UC Berkeley

UC Berkeley Electronic Theses and Dissertations

Title
Microbial Population Dynamics in Spatial Structure

Permalink
https://escholarship.org/uc/item/5w87506f

Author
Karita, Yuya

Publication Date
2022

Peer reviewed|Thesis/dissertation

Microbial Population Dynamics in Spatial Structure

by

Yuya Karita

A dissertation submitted in partial satisfaction of the

requirements for the degree of

Doctor of Philosophy

in

Biophysics

in the

Graduate Division

of the

University of California, Berkeley

Committee in charge:

Associate Professor Oskar Hallatschek, Chair
Associate Professor Aaron Streets
Associate Professor Britt Koskella
Associate Professor Noah K. Whiteman

Fall 2022

Microbial Population Dynamics in Spatial Structure

Abstract

Microbial Population Dynamics in Spatial Structure

by

Yuya Karita

Doctor of Philosophy in Biophysics

University of California, Berkeley

Associate Professor Oskar Hallatschek, Chair

Microbes proliferate and migrate to take over territories. The dynamics of population growth can be classified by the rate of proliferation and migration. When proliferation is predominant, the population density tends to saturate, and cells form expanding clusters. On the other hand, when migration is more active than the timescale of proliferation, the populations get almost well-mixed like a liquid culture in a shaken test tube. Both extreme cases have been extensively studied in previous research. However, the intermediate regime, where proliferation and migration consort with each other, has not been understood well. With this thesis, I attempt to provide an overarching insight into the interplay of proliferation and migration using microfluidic experiments and computer simulations.

In Chapter 2, we show that the balance of proliferation and diffusion results in the sharp transition between two density states, gaseous and jammed states, using a newly-developed microfluidic device named *microfluidic panflute*. The density dependence of the diffusivity is shown to be fundamental to producing bifurcating behaviors with hysteresis. We further discuss the ecological impact of the density transition on invasion resistance.

Chapter 3 characterizes the clone size distribution of jammed populations by fluctuation tests and lineage tracing with microfluidics. We show the characteristic power-law decay of the site frequency spectrum. We further discussed applying our results to cancer research: the site frequency spectrum can be reconstructed by sampling tumors spatially.

In chapters 4 and 5, characteristic behaviors of jammed and gaseous populations are discussed. Chapter 4 shows the impact of the shape of physical boundaries on the population dynamics in a jammed state. In chapter 5, gaseous populations in various types of flow are investigated.

This thesis contributes to the understanding of microbial population dynamics in spatial structure. Also, experimental techniques developed in this thesis, especially microfluidic systems, have the potential to be a platform for microbial experiments to investigate the ecological and evolutionary dynamics under spatial constraints.

To Haruka and Hiroto.

Contents

List of Figures

List of Tables

Acknowledgments

Chapter 1

Introduction

Proliferation is a central function of living matters at various scales. At the species level, life needs to produce offspring to inherit the genetic elements to future generations [1]. Also, increasing a population size to form a community is often beneficial to cope with external stresses such as harsh environments or competition against other species [2–4]. At the individual level, proliferation is key to development [5]: life emerges through a series of mitosis from a fertilized egg, which consists of a few cells, to a largely multi-cellular body, which consists of about 30 trillion cells in the case of a human [6]. Moreover, somatic replication is indispensable for turnovers and homeostasis [7].

Importantly, proliferation is never perfect: a random error can occur during the process, and it induces an inheritable change on a newly produced cell, referred to as a mutation. A mutation can change the function of a newborn and may cause defects. However, it also can drive evolution by neutral drifts or the emergence of a rare beneficial mutation [8, 9].

Once spatial dimensions are taken into account, dispersal and migration become a core factor in population dynamics because of the spatial proximity of two cells, a parent and a child, right after a proliferation event [10]. The two cells initially share the same spatial position as they are a single cell before the proliferation. Migration, which re-configures the spatial positions of cells, alters local interactions and thus impacts the community function and population dynamics (fig. 1.1) [11–13].

Migration can be driven by various mechanisms. In the case of embryonic development, collective movements, such as gastrulation [14], are well-programmed by a genetic blueprint. In the case of marine plankton, migration is largely driven by ocean currents [15, 16]. While dynamics are externally defined in these instances, migration also can be autonomous or self-driven. Crowds of animals often seek a better environment such as rich foods or a warm climate. This is also the case for microbial populations. Microbes can migrate to a better environment by sensing local chemical gradients, known as *chemotaxis* [17, 18]. In an extreme case, migration may be totally stochastic or random. In this case, the time development of cell density can be well-described by Brownian diffusion [19].

The concert of proliferation and migration is fundamental, especially when the time scale of proliferation is shorter than or comparable with that of migration. When proliferation is frequent,
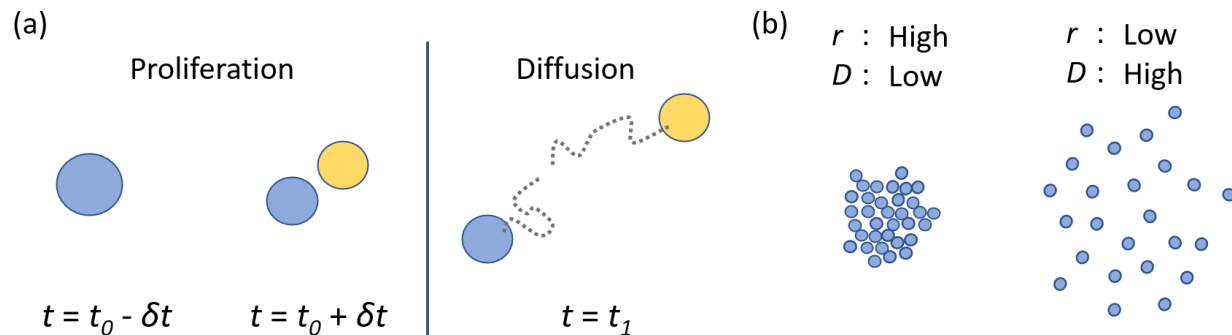
Figure 1.1: Illustrations of population dynamics with proliferation and diffusion. (a) At the onset of proliferation (right before the division $t = t_0 - \delta t$, and right after the division $t = t_0 + \delta t$), two cells (parent: blue and child: yellow) occupy the same spatial position. They are apart from each other at a later time point by diffusive movements ($t = t_1$). The dotted lines show the trajectories of the diffusion. (b) Population dynamics depend on the balance of proliferation and diffusion. When the proliferation is frequent (growth rate r is high), and the diffusion is suppressed (diffusivity D is low), the population gets localized and condensed (left). On the other hand, the population is sparse and well-mixed when r is low and D is high (right).

the cell density increases locally and saturates at its maximum density, called the *carrying capacity* [20]. Once the cell density locally saturates, it spatially expands to surrounding virgin spaces. This type of dynamics is called *range expansion* and relevant to the growth of solid tumors and bacterial biofilms [21, 22]. When proliferation is as frequent as migration, the interplay of two processes results in complex spatio-temporal patterns such as patch formation of marine plankton [23–25]. The dynamics depend on the details of a system and are involved even in a simple setup.

To investigate population dynamics in space, microbes have been useful experimental model systems. Because there is no stable artificial replicator, microbes are one of the simplest and most controllable systems available to study population dynamics. Importantly, their short doubling time (order of 1 hour) allows researchers to conduct experiments in a reasonable time scale. The migration of microbes can be driven by Brownian motions, swimming, and hydrodynamic flow. The impact of chemotaxis and interactions between species can also be investigated. In light of applications, some species are directly relevant to pathogens, and revealing their spatial dynamics can provide insights into therapeutic strategies [26].

In this thesis, the interplay of proliferation and spatial structure is the major overarching theme. Especially, I focus on yeast and bacterial populations as model systems and investigate collective dynamics in confinement by computational and experimental approaches. As an introduction, natural examples of microbial populations in a spatial structure are overviewed first, and the theoretical background of reaction-diffusion models and computer simulations are discussed. Typical

experimental methods are also introduced. In the end, the organization of this thesis is described.

1.1 Microbial populations in spatially structured habitats

Microbes are ubiquitously found in nature. Notably, most of their populations are spatially structured by the habitats. For example, microbial distributions in the human body are highly localized and specific to body parts. *C. acnes* colonizes skin follicles [27, 28], and *Lactobacilli* dominates the vaginal microbiome [29]. One of the main habitats for microbes is digestive tracts, such as the gut microbiome [30–32] and the oral microbiome [33]. Importantly, their populations are highly spatially structured. For instance, bacteria aggregate and form layers of biofilms on the tongue [34, 35]. They can also invade small spatial niches, such as folding structures or crypts in a gut [30–32]. Outside of the animal body, typical microbial habitats are soil and water. The soil microbiome is sensitive to the size of pores in soil [36, 37]. Also, the soil microbiome around plant roots, called rhizosphere, is highly specific to the type and spatial configuration of plants [38]. Microbes in bodies of water, such as lakes, rivers, and the ocean, are usually less spatially-structured: they typically float along with water currents. Still, some microbes can attach to and reside on the surfaces [39].

Spatial structure can highly impact ecological and evolutionary dynamics. In expanding populations, it has been experimentally revealed that spatial constraints weaken selective pressures [40, 41] and mutual interactions [42]. In confined populations, microfluidic experiments have shown that dense-packing induces drug resistance in *Pseudomonas aeruginosa* populations [43]. In natural cases, strong priority effects, such as colonization resistance, have been reported in the gut microbiome of mice [44, 45]and flies [46]. Also, significant clonality has been revealed in bacterial populations in human skin follicles [28]. Thus, investigating the impact of spatial structure is fundamental to ecology and evolution.

1.2 Spatial growth model

To model microbial population dynamics in space, a straightforward approach is to explicitly simulate the movement and the growth of every single cell. This "*agent-based model*" has been effective in studying the dynamics of relatively small populations; however, it is computationally expensive and not very useful for studying large populations. To capture macroscopic dynamics, it is tempting to coarse-grain populations with continuous models.

A reaction-diffusion model is a widely used mathematical model in population dynamics [47]. A general form which includes diffusion and growth is

$$\frac{\partial}{\partial t}c(x,t) = \nabla \cdot (D(c)\nabla c(x,t)) + r(c)c(x,t), \tag{1.1}$$

where x and t are space and time, and c, D, and r mean the cell density, diffusion coefficient, and growth rate, respectively.

As for the diffusion coefficient, its density dependence is often ignored:

$$\nabla \cdot (D(c)\nabla c(x,t)) = D_0 \nabla^2 c,$$

where D_0 is constant. However, the density dependence is a natural consequence of excluded volume effects and should be taken into account when c is close to the maximum packing density. Actually, chapter 2 shows that the density dependence can result in phase separation of two density phases, gaseous and jammed phases.

Various forms of the growth term have been extensively studied. When the growth is logistic,

$$\frac{\partial}{\partial t}c(x,t) = D_0\nabla^2 c + r_0\left(1 - \frac{c}{K}\right)c \tag{1.2}$$

is called the Fisher-Kolmogorov-Petrovsky-Piskunov equation (FKPP equation), and its traveling wave solutions have been widely investigated in the context of range expansion [48–50]. Once the density reaches the maximum value (carrying capacity) K, the growth term vanishes. Also, the growth term can include the Allee effect, which represents cooperative effects and the minimum critical population size for a population to survive [51]:

$$r(c) = r_0\left(1 - \frac{c}{K}\right)\left(\frac{c}{A} - 1\right),$$

where A is the critical population size. One can consider additional variables such as a spatially-varying nutrient concentration $S(x,t)$. With S, the growth term can represent the effect of nutrient depletion. One typical model is Monod growth [52]:

$$r(c) = r_0\frac{S}{S_h + S},$$

where S_h is a constant value with which $S = S_h$ gives $r_0/2$ growth rate. Typically, the spatial distribution of the nutrient can also be described by a reaction-diffusion equation:

$$\frac{\partial}{\partial t}S(x,t) = D_S\nabla^2 S - kr(c)c, \tag{1.3}$$

where D_S is the diffusivity of nutrient molecules, and k is a constant coefficient.

Importantly, to analyze the equations, boundary conditions largely impact the solutions. As a simple example, steady-state solutions of a simple 1D reaction-diffusion model

$$\frac{\partial}{\partial t}c(x,t) = D_0\frac{\partial^2}{\partial x^2}c + r_0 c \tag{1.4}$$

can be expressed by combinations of wave functions. Reflecting boundary conditions or absorbing boundary conditions

$$\left.\frac{dc_s(x)}{dx}\right|_{x=x_1} = 0, \quad c_s(x_2) = 0 \tag{1.5}$$

constrain the possible solutions significantly, where c_s is the steady-state cell density. The lowest-order wave solution defines the typical length scale of the population

$$L_c = a\sqrt{\frac{D_0}{r_0}},$$

where a is a constant whose order is 1. This length scale has been used to infer the typical patch size of marine plankton [24]. A similar argument appears in chapter 2 to characterize the critical chamber size for phase transition.

1.3 Dynamics in jammed states

Once cellular populations get jammed, a reaction-diffusion model is no longer valid because migration becomes non-diffusive. Cells physically contact each other, and diffusion is strongly suppressed by jamming. The proliferation of cells results in mechanical forces pushing neighbors due to excluded volume effects. These local pushing dynamics require other models. One typical model for crowded populations is a contact process or voter model [53]. This is a spatially-discrete model which stochastically replaces the cell type at a certain position with a neighbor cell type. The replacement can either push all the other cells representing the propagation of pushing forces, or just locally change the cell type representing the death or turnover of the previous cell type at the position. These models have been used in microbial growth, colon cancer, and stem cell renewal of mouse spermatogenesis or intestinal crypts [54–57].

If a population is expanding, Eden model is another major model [58]. In the model, there is no replacement of existing cells, but they proliferate to invade surrounding virgin spaces. Also, the Domany-Kinzel model is a model for range expansion, which is usually defined on triangular or hexagonal lattices [59, 60]. The front dynamics of the Domany-Kinzel model can be regarded as a contact process.

Continuous models are also useful in some situations. The velocity of cells can be expressed by the integration of growth rate over space:

$$\dot{x} = \int_{x_0}^{x} r(x) dx,$$

where x_0 is the position where cells always do not move, such as the wall or the center of an expanding colony. This mass conservation relation can be re-written in a differential form:

$$\nabla \cdot \dot{x} = r(x).$$

Here, one can introduce "internal pressure" $p(x)$ to express

$$\dot{x} = -\mu \nabla p$$

with a motility coefficient μ. This equation is called Darcy's law, which was first introduced to express hydrodynamics in porous materials in the 1850s [61]. This equation also has been used to model the dynamics of tumor growth [62, 63]. With this equation, now we get

$$\nabla^2 p = -\frac{1}{\mu} r.$$

This is similar to the equations of electrostatics:

$$E = -\nabla \phi$$

$$\nabla \cdot E = -\nabla^2 \phi = \frac{\rho}{\varepsilon}$$

In chapter 3 and 4, the application of continuous models is discussed.

1.4 Well-mixed states

In well-mixed situations such as a liquid culture in a shaken flask or a dilute population of swimming bacteria, the reaction-diffusion model is also not useful because the cellular movements are much faster than the time scale of proliferation. As the time scale of growth and migration is separated, spatial configurations do not matter to the population growth. And thus, one can safely ignore the spatial variables.

Well-mixed dynamics have been widely studied in classic population genetics for a long time [8] and have provided a useful null model to infer the impact of spatial dimensions. Deviations from a null model may imply that the spatial structure is not negligible. However, importantly, some observables, such as a site frequency spectrum, can be similar between well-mixed and spatially-structured populations by chance, even though the underlying mechanisms are different. One example of the coincidences is the main topic of chapter 3.

1.5 Experimental approaches

To study microbial population dynamics, various experimental systems have been proposed and developed. The most common system is a liquid culture. One can culture cells in a liquid medium in a test tube or flask with appropriate incubation and shaking. A well-shaken culture is supposed to be well-mixed, and the spatial dimension becomes less relevant as long as there is no aggregation or sedimentation. Recent studies have successfully increased the throughput of liquid-culture experiments using 96-well plates with automated liquid handling or microfluidic or millifluidic droplets with programmed droplet manipulation [64–66].

To investigate spatially-structured populations, agar plates or agar pads have been major platforms, but other model systems, such as bacterial mats or biofilm on beads, also have been useful [67, 68]. Recently, a new effective method, microfluidics, has quickly developed and become an indispensable tool.

With microfluidics, one can design an arbitrary geometry and regulate a medium environment precisely and rapidly. Also, microfluidics enables imaging in real time at a single-cell resolution. A remarkable application of the method is the so-called *mother machine*, where a bacterial lineage is trapped in a thin channel [69]. The experimental designs in chapters 2 and 3 are inspired by this prior work. Other various types of microfluidics are introduced in chapter 5.

1.6 Overview of this thesis

In chapter 2, we find a characteristic transition of density phases using microfluidics. The bacterial populations in microfluidic cavities exhibit two density phases, gaseous and jammed phases. The phase separation is driven by the balance of the population growth and diffusive outflow, and it is sensitively dependent on the length scale of the system. We show that the observed density phases can be understood by a reaction-diffusion model with a density-dependent diffusivity. We further

discuss the ecological impact of the phase transition using invasion experiments with an antibiotic attack.

We focus on the dynamics of a jammed phase in chapter 3. Using a switcher budding yeast strain, the clone size of lineages is measured in a jammed population in a microfluidic chamber. The clone size distribution follows a power-law decay, which can be reproduced by a 1D continuum model and agent-based simulations. The connection to the site frequency spectrum in expanding populations in nature, such as bacterial biofilms and tumors, is also discussed.

Chapters 4 and 5 investigate characteristic behaviors of jammed and gaseous populations. In chapter 4, the impact of physical boundary conditions in a jammed phase is discussed. The shape of walls defines the spatial advantage to persist in a confined population. The dynamics are modeled by a hydrodynamic approximation and simulated by agent-based simulations. In chapter 5, the influence of medium flow on a dilute population is studied. Hydrodynamic flow can mix cells, but also trap cells in a certain condition. Various types of flow are produced with microfluidic devices, and the impact on microbial population dynamics is experimentally tested.

Chapter 2

Scale-dependent tipping points of bacterial colonization resistance

Proliferation of cells increases the density of a population, while diffusive movements of cells decrease the local density. The balance of the two factors is critical, especially in a confined habitat, a space surrounded by walls with an outlet. In this chapter, we discuss the phase transition of cell densities by tuning the rate of proliferation and the length scale of habitats. We develop a novel microfluidic device named *microfluidic panflute*, where the chamber size is systematically varied. The ecological significance of the density phase transition is highlighted in invasion dynamics. We show that a jam-packed population is resistant to the invasion by a fitter strain, while a gaseous population is not.

The rest of this chapter was published as

Yuya Karita, David T. Limmer, Oskar Hallatschek, Scale-dependent tipping points of bacterial colonization resistance. Proceedings of the National Academy of Sciences, 115, e2115496119 (2022). https://doi.org/10.1073/pnas.2115496119

The supplementary movies mentioned in the main text are available from the journal website.

2.1 Abstract

Bacteria are efficient colonizers of a wide range of secluded micro-habitats, such as soil pores, skin follicles, or intestinal crypts. How the structural diversity of these habitats modulates microbial self-organization remains poorly understood, in part because of the challenge to specifically manipulate the physical structure of microbial environments. Using a microfluidic device to grow bacteria in crypt-like incubation chambers of systematically varied lengths, we show that small variations in the physical structure of the micro-habitat can drastically alter bacterial colonization success and resistance against invaders. Small crypts are un-colonizable, intermediately sized crypts can stably support dilute populations, while beyond a second critical lengthscale, populations phase-separate into a dilute and a jammed region. The jammed state is characterized by

extreme colonization resistance, even if the resident strain is suppressed by an antibiotic. Combined with a flexible biophysical model, we demonstrate that colonization resistance and associated priority effects can be explained by a crowding-induced phase transition, which results from a competition between proliferation and density-dependent cell leakage. The emerging sensitivity to scale underscores the need to control for scale in microbial ecology experiments. Systematic flow-adjustable lengthscale variations may serve as a promising strategy to elucidate further scale-sensitive tipping points and to rationally modulate the stability and resilience of microbial colonizers.

2.2   Introduction

Natural microbial communities are often found to be remarkably stable, capable of either quickly recovering from disturbances or remaining essentially unaffected by them [70–73]. Stability is particularly puzzling in small populations, which are prone to number fluctuations and lack the size and extent to buffer against local environmental changes. Nevertheless, small but stable populations have been found in association with spatially defined micro-habitats [32, 44, 45, 73–76].

Strains that colonize cavities are sometimes found to be so stable that they hold their ground against even much fitter invaders [77]. For example, *Bacteroides fragilis* is a particularly resilient colonizer of crypts in mouse guts [44]. Conspecifics are unable to invade, unless the resident strain is strongly suppressed by an antibiotic. A similar colonization resistance has been demonstrated for groups of ceca microbiota in mice guts [45] and for *Lactobacillus plantarum* in fly guts [46, 76].

The ubiquity of micro-habitat associated stability and colonization resistance raises the question of whether these features generically emerge in confined spaces, for example soil pores [36, 37, 78], skin follicles [28, 73], or crypts and folds in gut-like environments [30, 32, 79]. Previous studies have identified biological features, such as suppressed biofilm growth or the expression of specific adhesion molecules, that promote stability in specific systems [44, 70, 80–82]. However, we currently lack systematic scale-dependent measurements to identify a generic mechanism of stability and resilience in micro-habitats, as well as a theory that could predict colonization success and tipping points. To fill this gap, we developed an approach to measure the scale-dependence of microbial colonization patterns combined with a predictive theory of how microbes invade, occupy and protect confined micro-habitats.

2.3   Experimental Setup

Our experiments employ a microfluidic incubation device that allows to continuously monitor bacterial population dynamics in crypt-shaped chambers across many lengthscales (Fig. 2.1a). A supply channel is used to continuously perfuse the device with media enabling the experiments to run under constant conditions for several days. As bacteria are inoculated and pass through the supply channel, they get exposed to rectangular cavities of systematically varied depths (10-350

μm). Even though the fluid inside these cavities is largely stagnant, it is nutrient rich and hence supports growth, due to the rapid diffusion of small nutrient molecules from the supply channel [69, 83].

In this device, lengthscale-dependent ecological processes can be identified by comparing the colonization dynamics across the sequence of chambers. To capture the differential population dynamics in single microscopy frames, we ordered the cavities according to size (see Fig. S1 for a randomized control). The device thus resembles a panflute in appearance, so we refer to our device as a "Microfluidic Panflute". We employed it to explore the colonization dynamics of several bacterial genera, focusing mainly on *Acetobacter*, which is prevalent in the fly gut [76, 84] and grows aerobically.

2.4   Results

We found that the emerging population dynamics sensitively depend on the length of the incubation chamber (Fig. 2.1b and Supplementary Movie 1). The scale sensitivity is particularly strong near two recognizable phase transitions:

Establishment Transition

While all cavities are sporadically visited by cells, colonization attempts remain unsuccessful in small chambers. In chambers exceeding a certain threshold length (170 μm in Fig. 2.1b), cell densities stabilize after 2-3 days of incubation and are maintained for at least five days. Cell densities, as measured from the time-averaged signal intensity, increase with chamber length, are highest at the floor of the cavities and gradually decay towards a line of zero density (Fig. 2.1d). We call this regime "gaseous" because the cell packing fraction is small and cells diffuse almost freely (SI Fig. S2).

Jamming transition

When the chamber length exceeds a second threshold (220 μm in Fig. 2.1b), a densely populated region appears at the bottom of the cavities that is sharply separated from a gaseous region towards the opening of the cavities (see chambers 6 and 7 in Fig. 2.1b). Confocal imaging shows that neighboring cells are in direct contact in the dense phase, which is why we call the condensed phase "jammed" (Fig. 2.1c). Dynamically, the jammed phase grows like a wave from the floor towards the open boundary of a chamber, as can be seen in the kymograph Fig. 2.1e. The growth of this wave slows down near the jamming transition (Supplementary Movie S1). Interestingly, the transition from gaseous to jammed is abrupt in the size of the chambers. Between two neighboring cavities, differing by just 5% in length, the colonization state transitions from gaseous to nearly 75% jammed (quantified in Fig. 2.1d).
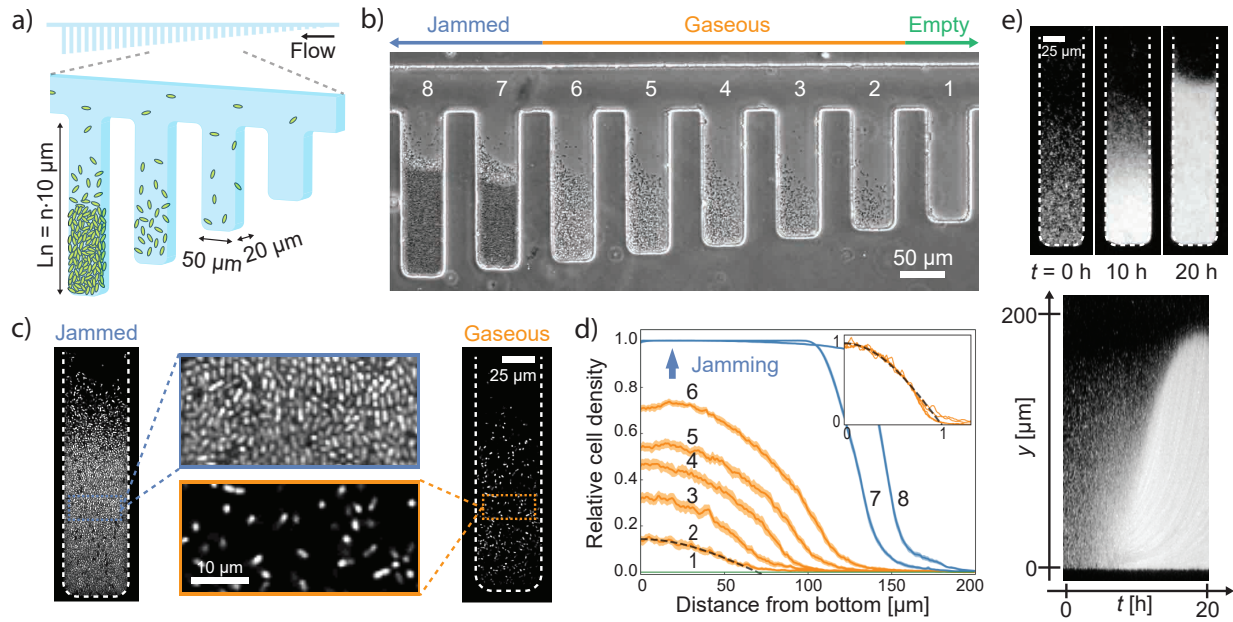
Figure 2.1: Microfluidic experiments reveal lengthscale-dependent colonization patterns. (a) A scheme of our Microfluidic Panflute incubation device: Rectangular cavities of systematically varied depths ($n = 1, 2, \ldots, 35$) are connected to a common supply channel through which media and bacteria flow. (b) The steady state after five days of incubation of a fly gut bacterium (*A. indonesiensis*). Depending on their length, cavities could not be invaded (1), hosted a gaseous population (2-6) or a phase-separated population with a jammed and gaseous state (7-8). (c) Confocal images of a partially jammed and gaseous population. The zoomed-in images are magnifications of the zoomed-out snapshots. (d) Steady-state cell density profiles obtained from time lapse movies. The shaded regions show the standard error of the mean. The profiles of gaseous phases (orange) collapsed to our linearized establishment model (black) upon rescaling both axes (inset). (e) A kymograph of the jamming front movement.

We observed qualitatively similar colonization patterns for species of other genera, including *V. cholerae* and *L. lactis* (Fig. S3). We therefore sought to explain the pronounced lengthscale-sensitivity by a general species-independent mechanism.

Linear Establishment Model

The colonization of a cavity can be viewed as a tug of war between cell proliferation and cell removal by outflow or death[1]. This competition can be considered in the absence of regulation or specific cell-cell interactions, in order to discern whether the rich scale-dependent phase behavior seen in our experiments is a consequence of general biophysical processes. To describe how the cell density $c(y,t)$ at a vertical position y and time t changes over time, we use the linear reaction-diffusion equation $\partial_t c(y,t) = D_0 \partial_y^2 c(y,t) + r c(y,t)$ where the first term represents cell diffusion with diffusivity D_0 and the second term represents cell proliferation with growth rate r. Since cells cannot penetrate the floor of the chamber, we use a reflecting boundary condition at $y = 0$, $\partial_y c(0,t) = 0$. We also introduce an absorbing boundary at $y = L$ where the cells are swept away by the media flow, $c(L,t) = 0$.

Our mathematical analysis (SI Sec. A.3) shows that the dynamics of the density profile can be decomposed into a sum of independently evolving normal modes. The empty state is stable if the amplitude of all normal modes shrink, which requires that the scale L of the population does not exceed the critical scale $L_{\text{est}} = \pi \sqrt{D_0/r}/2$. In turn, this implies that bacteria can establish in a chamber only if $L > L_{\text{est}}$. Thus, establishment is promoted by increasing the growth rate or decreasing the diffusivity, which drives the cell leakage. Using the measured growth rate, $r \approx 0.33 \pm 0.01$ h^{-1} (Fig. S4a and d), and diffusivity, $D_0 \approx (0.37 \pm 0.01) \times 10^3$ μm^2/h (Fig. S2), we estimate establishment in our experiments to occur at the scale $L_{\text{est}} \approx 53 \pm 1$ μm. This is consistent with the empirical value 53 ± 7 μm that we extrapolate from our measurements (Fig. S5b). We also confirmed that the establishment length changes predictably with variations in growth rate (Fig. S6). More importantly, the measured density profiles agree well with the cosine shape of the first normal mode, as observed in Fig. 2.1d, which is expected to dominate close to the onset of colonization (SI Sec. A.4). Our analysis is best suited to describe the bulk of the population where cell motion is dominated by diffusion. Deviations are expected, and indeed visible around the opening of cavities (near vanishing cell density) where the flow of the media is not negligible.

Nonlinear Population Control

Our linear model can tell us whether bacteria grow in empty chambers but it remains blind to how a population of successful colonizers reaches a steady state with a finite population size and how stable this state is. To predict the long-term dynamics, we needed to include a (non-linear) population control term that modulates the competition between cell proliferation and removal. For example, bacterial batch cultures are often limited by nutrient deprivation or waste product accumulation, implying that the growth rate is not constant but decays with density (logistic population

---

[1] In our experiments, removal is dominated by outflow. Cell death can also be included through an effective growth rate, representing the difference between growth and death rate
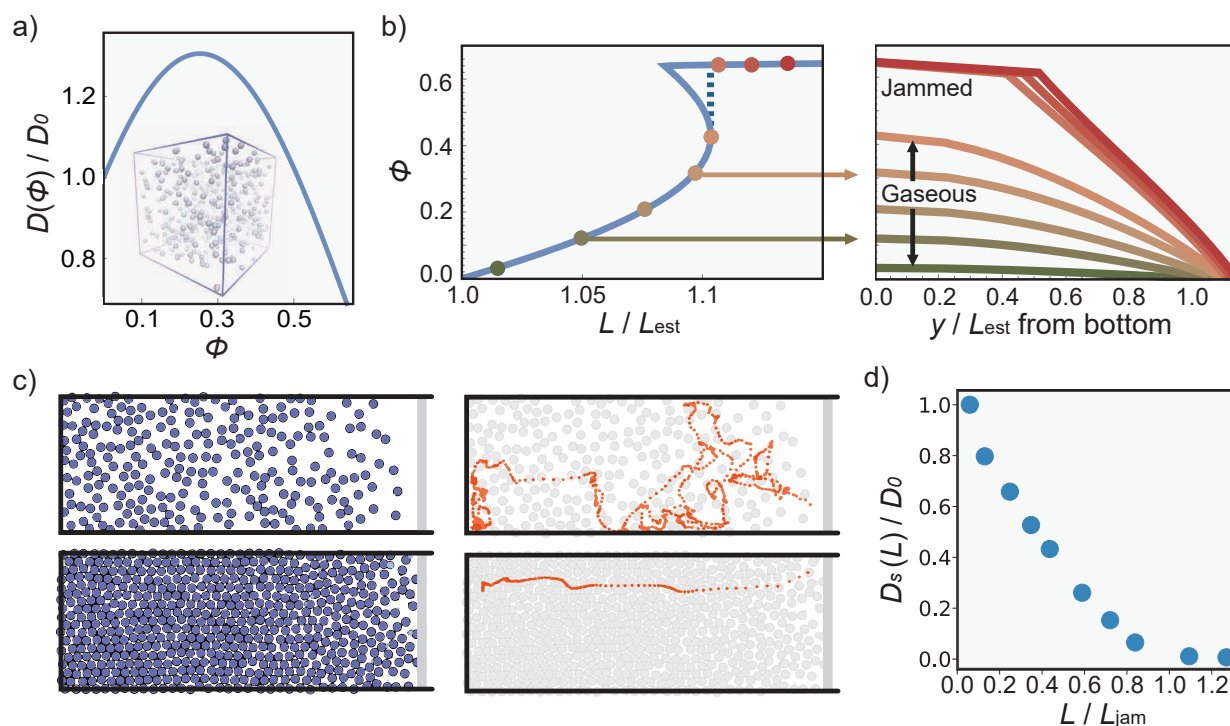
Figure 2.2: Theory: Collective motion can stabilize a growing population and drive phase separation. (a) Simulations show that the collective diffusivity of an idealized model of proliferating hard spheres in suspension is non-monotonic as a function of the packing fraction $\Phi = c\pi\sigma^3/6$ with σ the diameter of the particle. The negative gradients at high densities can drive a discontinuous transition towards jamming. (b) The packing fraction profile (right) was computed from the density-dependent diffusivity in (a) (see SI Sec. A.5). The maximum packing fraction (left) shows a fold bifurcation as a function of L/L_{est}, resulting in a sudden transition to a (partially) jammed state. (c) Minimal simulations of proliferating soft disks and example tagged particle trajectories for gaseous $L < L_{\mathrm{jam}}$ (top) vs. jammed states $L > L_{\mathrm{jam}}$ (bottom) pores. (d) Self-diffusion, D_s, in the gaseous state is larger by orders of magnitude than in the jammed state, suggesting a mechanism for an invasion barrier.
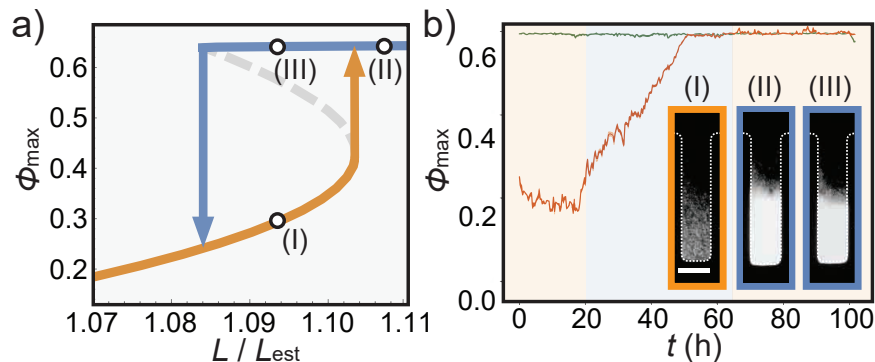
Figure 2.3: Bistability near the tipping point. (a) Phase diagram: The maximal packing fraction at steady state, Φ_{max}, as predicted from the density-dependent diffusivity in Fig. 2.2a. When the control parameter L/L_{est} is gradually increased, the state of the system suddenly jumps from a gaseous (I) to a partially jammed state (II, arrow pointing up). If one decreases the control parameter again, the system jumps back to a gaseous state (arrow pointing down), but at a different value of the control parameter, implying a hysteresis and a region of bistability. (b) Experiments to test bistability: A flow decrease triggered in the depicted chamber the transition from gaseous (I) to jammed (II), via an effective increase of the habitat size L. The orange curve depicts the density increase over time. After saturation, we increased the flow again but the chamber remained in the jammed state (III) at high density (green curve). The y-axis of the plot was normalized by $\Phi_{\mathrm{rcp}} \sim 0.64$, random close packing of monodisperse spheres (see Fig. S7). The scale bar indicates 50 μm.

control). However, growth rates in the jammed and dilute phase were statistically indistinguishable (Fig. S4), suggesting that nutrient deprivation did not limit population growth. Therefore, we hypothesized that, while the growth rate remains approximately constant, the population outflow adjusts itself via a density-dependent diffusivity $D(c)$. Steady state is reached when the cell leakage matches the influx of newborn cells in the bulk of the chamber.

Crowding-induced Phase Transition

Our mathematical analysis shows that a monotonically increasing $D(c)$ (more cells → more outflow) is capable of stabilizing a gaseous state inside the chambers (SI Sec. A.4). However, to reproduce a sudden jamming transition, $D(c)$ has to have a region of negative slope at high densities (more cells → less outflow). Intuitively, this generates a positive feedback cycle. As the density fluctuates up, diffusion-induced outflow goes down, which leads to even higher cell densities, suppressing outflow even more and so on. The cycle only breaks when the bacteria jam and come into contact, upon which the bulk modulus and, hence, $D(c)$ shoot up by several orders of magnitude [85].

The required negative slope of $D(c)$ could be induced at high density by constitutive or crowding-induced stickiness between cells, or active motility, which has been shown to drive phase-separation [86]. Our simulations (Fig. 2.2) and analytical arguments (SI Sec. A.7) show that even purely repulsive non-motile spheres exhibit a qualitatively similar phase behavior as seen in our experiments. Thus, a transition between gaseous and partially jammed states emerges without any special biotic factors other than proliferation.

In the SI, we show that, by exploiting a mathematical analogy to a solvable Newtonian problem, the phase diagram and the density profiles (c.f. Fig. 2.2b for hard spheres) can be obtained exactly by numerical integration (via SI Eqs. 34 and 35) from the underlying growth and dispersal parameters. This analysis shows that the position of the tipping points depends on the entire functions $D(c)$ and $r(c)$ up until the tipping point and, thus, can be modulated by any means that change these functions, such as attractive interactions or quorum sensing.

Our theory also predicts that the jamming transition arises through a fold bifurcation and, therefore, should have the characteristics of a tipping point [87–89]. In particular, once a chamber becomes jammed it is not easily unjammed and requires a substantial perturbation of the control parameters (growth rate or diffusivity). This also implies that there must be a region of bistability, where in the same chamber two states are stable - one gaseous and one phase-separated state (Fig. 2.3a). We confirmed that, in our experiments, chambers near the jamming transition indeed show bistability (Fig. 2.3b and S7) by flipping from one state to another using flow modulation (Fig. S8).

Tipping points also reveal themselves dynamically, through a dramatic slowing down near the transition point – a phenomenon called critical slowing down [87]. Indeed, our time lapse Supplementary Movie S1 shows that the relaxation dynamics near the transition point becomes very slow. The smallest jammed chamber takes about 30 hours or 14 doubling times to reach steady state, compared to 6 hours or less in the largest chambers.

Crowding-induced Drop in Diffusion

Simulations of a proliferating soft sphere model (see SI for details) further show that the cellular self-diffusion is dramatically reduced upon jamming, consistent with an onset of rigidity, except for movement of order one cell diameter per doubling induced by the division process (Fig. 2.2c). While in our experiments we could not track single cells in the jammed phase, we could track lineages using fluorescent tracers (Fig. S9), which also suggests self-diffusion to drop by two orders of magnitude from the gaseous to the jammed state.

A drop in self-diffusion has important consequences for species invasions. It lowers the chance for outside cells to diffusively penetrate the jammed fraction against the proliferation current coming from the floor of the chamber. Accounting for this crowding-induced diffusion barrier in a theory of strain invasion (SI Sec. C.1), we predict that the rate at which an external strain invades a jammed resident population is exponentially small in the ratio of the thickness of the jammed phase and the cell diameter. Thus, invasion of jammed populations should be an extremely rare event.

Colonization Resistance

To test this prediction, we performed specific invasion experiments. We inoculated our device with the wild type strain of *A. indonesiensis* and waited until a steady state was reached. We then flowed in a sister strain of the same species, which was fluorescently labeled green and resistant to the drug tetracycline. Titration of tetracycline then allowed us to tune the growth rate advantage of the invading strain.

In the absence of antibiotics, we did not observe any successful invasion over the experimental time scale of five days. When we added 10 µg/mL of the antibiotic (60% of MIC), scale-dependent invasion dynamics ensued: In the initial 24 hours, the drug-sensitive populations decreased the population density (Supplementary Movie S3), thus shifting the phase boundary between gaseous and jammed to larger cavities. Over the next 48 hours, drug resistant cells entered and seized a substantial number of the gaseous chambers (Fig. 2.4c and Supplementary Movie 4). Upon successful invasion, the population density generally increased again. Importantly, while most of the gaseous chambers were ultimately invaded, none of the jammed chambers did (out of 7 colonized panflutes monitored over 2-5 days in 3 independent experiments). The primary effect of the antibiotic is to push the state of some of the chambers from jammed to gaseous, upon which invasion becomes possible (Fig. 2.4a). Thus, while crowding strongly protects jammed populations from invasion, residents can be dislodged nevertheless if they are driven past a tipping point into a more fragile (gaseous) ecological state.

2.5 Discussion

We have shown that microbial colonization patterns can vary dramatically with the physical structure of their micro-environment. In particular, a crowded state with pronounced colonization resistance can arise spontaneously when the incubation scale exceeds a certain tipping point. Once pushed beyond the tipping point, it requires a substantial perturbation to break the ensuing colonization resistance, for instance by using antibiotics to trigger the reverse transition towards a gaseous phase with increased mixing (Fig. 2.4a).

The physical structure of the micro-environment, thus, acts as an ecological filter, permitting stable and resilient colonization by species with matching traits. By modulating the physical characteristics of this filter, hosts can actively or passively shape the pool of potential bacterial residents. Modulating endogenous micro-structures or introducing rationally-designed structures may also be considered as a strategy for precision-microbiome therapies to modulate microbial diversity.

The structure-induced stability supports the view that community assembly from potential colonizers are shaped by priority effects: whoever invades first enjoys colonization resistance against late invaders. The randomness induced by the order of strain arrival might contribute to the substantial host-to-host variability seen in some host-associated microbial communities [28, 45].

Colonization patterns, tipping points and colonization resistance could be captured by a minimal model that accounts for growth, diffusion and leakage. This model revealed a generic fold-
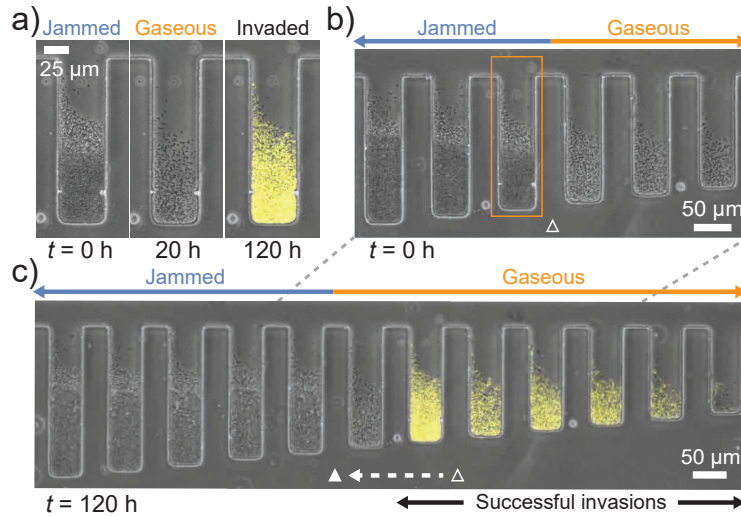
Figure 2.4: Crowding-induced colonization resistance. (a) After the chambers were pre-colonized by the wild type strain (dark), we introduced a fluorescently labeled "invader" strain (yellow). To make invasions more likely, we also increased the fitness of the invader by the simultaneous injection of an antibiotic (tetracycline) to which the invader was made resistant against. (b) A steady state of sensitive populations before the invaders were inoculated. The unfilled triangle shows the transition point between jammed and gaseous phases in the experiment. The transition was manually defined based on the bright-field darkness of the populations. (c) 120 hours after tetracycline was added to the culture medium. Drug-sensitive populations (dark) that remained jammed were not invaded. The unfilled and filled triangle show the transition points between jammed and gaseous phases at $t = 0$ h and $t = 120$ h respectively. The injection of the growth inhibitor (tetracycline) shifted the transition point.

bifurcation generating a discontinous transition between a gaseous phase, in which cells diffuse freely, and a glassy, jammed phase. This transition differs from what is known as Motility-Induced-Phase Separation (MIPS) [86] in the field of Active Matter [90, 91]. MIPS is associated with a spinodal instability that arises when an effective diffusivity becomes negative – an unintuitive consequence of the non-equilibrium nature of active motility [92]. In our case, the transition is triggered by the weaker condition of a (sufficiently) negative density-dependent diffusivity, which generically arises even for passively diffusing particles [93], for example hard spheres. It would be interesting to extend our model of proliferating active matter by active motility to see how bacteria that grow and swim self-organize in confined spaces.

While the tipping points in our experiments could be explained by our minimal model, we expect that, in general, additional biotic and abiotic factors influence colonization patterns quantitatively. For example, crowding will be promoted if cells stick to one another directly or indirectly through biofilm formation, or if nutrients are supplied from the floor of the chamber. On the other

hand, both establishment and jamming tend to be hindered by strong nutrient limitations or bacterial motility. While further research is needed to explore the relative importance of these factors, their impact may be anticipated theoretically using a reaction-diffusion model, which entails a flexible approach to analyze steady states (SI Sec. A.5).

More broadly, our results underscore that the lengthscale of experimentation can have a strong influence on micro-ecological processes, which could confound experiments that do not control for scale variation [94] – a well appreciated problem in the macro-ecological context [95–97]. Flow-tunable scale variations as implemented in our Microfluidic Panflute offer a systematic experimental approach to detect or exclude scale sensitivity in culturable microbial communities. Since the time scales of microbial evolution and ecology are inter-twined, we expect such scale sensitive experiments an exciting avenue for future eco-evolutionary research [98].

2.6 Acknowledgments

2.7 Methods

Bacterial strains and culture condition

The *Acetobacter indonesiensis* strains were derived from SB003 (kindly gifted by William Ludington, Carnegie Institution for Science), which was originally isolated from lab flies (*D. melanogaster*) [76, 84]. SB003 was transformed with mGFP5 via the backbone plasmid pCM62 [99] by Benjamin Obadia [46]. For culturing, all strains were grown in MRS medium (BD) at 30 °C. Strains are selected with 15 µg/mL tetracycline (Corning Cellgro) if needed.

Microfluidics fabrication

The microfluidic devices were fabricated by soft lithography [100, 101]. In order to make a master mold, a 20µm-thick layer of negative photoresist (SU8-2010, MicroChem) was spin-coated on a silicon wafer (WaferNet) and patterned by photolithography with a mask aligner (Hybralign 200, OAI) through a photomask (CAD/Art Services). On the master mold, Polydimethylsiloxane (PDMS, Sylgard 184, Dow Corning) was poured with crosslinker at 10:1 ratio and cured at 60 °C

in an oven overnight. The patterned PDMS was punched to make holes for inlets and outlets. The PDMS was bonded to a glass coverslip with O_2 plasma treatment by a reactive ion etcher (Plasma Equipment Technical Services).

Microfluidic cell culture

Prior to microfluidic culture, cells were streaked on a plate from frozen stock and grown in a test tube with 3 mL MRS for 1-2 days. The suspension of cells was injected into a microlfuidic device and cultured for 3-5 days with a continuous supply of the fresh medium until the system reached a steady state. The temperature was regulated at 30 °C by a microscope incubator (H201-T and UNO, Okolab), and the flow rate of the culture medium was controlled at 0.3 μL/h by syringe pumps (neMESYS, CETONI). Images were taken by inverted microscopes (IX81, Olympus. Also, Eclipse Ti, Nikon, was occasionally used for Figs. S6b and S7b.) and a confocal microscope (LSM 700, ZEISS).

Density profile measurement

To quantitatively measure the density profile of cellular populations in microfluidic crypts, GFP-tagged cells were cultured in a Microfluidic Panflute for about three days. After the system reached a steady state, fluorescent intensities were measured every 20 minutes for 14-48 hours. The intensities were first averaged over the horizontal direction, and then averaged over the time points at each *y*-position. They were scaled by the intensity of jammed populations to get relative cell densities. A standard error of the mean was calculated by dividing the standard deviation across time points by the square root of the approxomate number of uncorrelated time points. The latter was estimated by dividing the total duration of the time lapse movie by the typical relaxation time (6 hours) of the density profile measured in the gaseous phase (see Fig. S7d).

Neutral competition and invasion with fitness effect

To observe competitions of two strains with and without fitness effects, wild-type and GFP-tagged strains were co-cultured. As the GFP-tagged strain was resistant to tetracycline, with 10 μg/mL of tetracycline, the GFP-tagged cells grew normally while the wild-type strain grew slowly. We confirmed that there was no significant growth rate difference between the strains in the absence of antibiotics (Fig. S4b).

For neutral competition experiments, a 50:50 mixture of dark and GFP-tagged cells were inoculated into a Microfluidic Panflute device and cultured for two days. As each type of cells colonized chambers stochastically, we parallelized six rows of the panflutes and selected chambers with a desired initial population ratio. The population dynamics were observed with a fluorescent microscope every 20 minutes for a day.

To test the colonization resistance of jammed populations, we first cultured wild-type cells in a microfluidic device. After the populations reach a steady state, the culture medium was changed from MRS to MRS + 10 μg/mL tetracycline, and GFP-tagged cells were continuously flowed

into the device. The resulting population decay and invasion dynamics were observed with a microscope every 20 minutes for two days. In addition, the snapshots of the populations were taken every day for five days.

Flow and temperature change experiments

To investigate the effect of the system's parameters on the population density in microfluidic crypts, we dynamically changed the flow rate to tune the effective chamber depth. We initially cultured cells at 0.8 μL/h flow rate for three days until the system reached a steady state, and changed the flow rate to 0.3 μL/h. The decrease of the flow rate affected how deep the streamlines invaded chambers and changed the effective chamber depth by 5-10 μm (Fig. S8). After the system reached a second steady state, we recovered the flow rate to 0.8 μL/h to investigate hysteresis.

We also dynamically changed the temperature of the incubation chamber for controlling the growth rate of cells. We first cultured cells at 22 °C, where the growth rate is 0.28 h^{-1}, until a steady state, and ramped up the temperature to 30 °C, where the growth rate is 0.33 h^{-1} (for the growth rate measurement, see Fig. S4d). The transition dynamics were recorded every 20 minutes with a microscope.

Colonization experiments with other species

Colonization dynamics in a Microfluidic Panflute were tested with various microbial species (*Escherichia coil*, *Bacillus subtilis*, *Vibrio cholerae*, *Acetobacter pasteurianus*, *Acetobacter tropicalis*, and *Lactococcus lactis*. See Table S1 for the strain details and culture media.). Cells were streaked on a plate from frozen stock, and a small number of cells from a single colony were grown in a test tube with 3 mL of a culture medium for 1-2 days at 37 °C for *Escherichia coil* and 30 °C for the other species. The cell suspension was injected into a Microlfuidic Panflute and cultured for 5-6 days with a continuous supply of fresh media until the system reached a steady state. During the microfluidic culture, the temperature was regulated at 30 °C for all species.

Growth rate measurement

The growth rate of cells was measured in two ways: growth assay with a plate reader and particle image velocimetry (PIV) of a jammed population on microfluidics. Prior to the measurements, cells were cultured in test tubes from single colonies for 1-2 days in MRS at 30 °C up to saturation. For the plate reader experiments, cell suspensions were diluted to 0.02 OD, and 200 μL of the suspensions were transferred to transparent flat-bottom 96-well plates (Thermo Fisher Scientific). The plates were incubated in a plate reader (Spectramax) at 30 °C, and the optical density (OD) was measured at 600 nm wavelength every 5 minutes with 30-second mixing before each measurement. The maximum growth rate was calculated by fitting an exponential curve to the initial 2-hour growth. The growth rate of *Acetobacter indonesiensis* was measured as $0.325 \pm .003$ h^{-1} (Fig. S4a).

For the PIV measurement on microfluidics, cells were injected into a microfluidic device and incubated in a table-top incubator until cells colonized chambers and formed stable populations. Bright-field images were taken every 3 minutes for 3 hours and analyzed with PIVlab in Matlab [102]. PIV calculated the displacements of cells per timeframe. The displacement of a cell at position $y = y_0$ was caused by the growth of cells at $y \in [0, y_0]$, and therefore, the displacement at position $y = y_0$ could be formulated as $d(y_0) = y_0(e^{r\Delta t} - 1)$. Since our timeframe ($\Delta t = 3$ minutes) was much smaller than the doubling time of the cell (2.1 hours), it held $d(y_0)/\Delta t \approx ry_0$. Thus, the slope of the velocity field in the y-direction gave the growth rate. The growth rate of *Acetobacter indonesiensis* was measured as $0.332 \pm .007$ h^{-1} (Fig. S4d).

Diffusivity measurements

Self-diffusivity

To estimate the self-diffusivity of cells in gaseous and jammed phases, the displacement of cells was tracked over time, and the mean square displacements were calculated. A 50:50 mixture of dark and GFP-tagged cells was injected in a Microfluidic Panflute and cultured until the system reached a steady state. The motions of GFP-tagged cells were recorded with a fluorescent microscope every 30 seconds for 10 minutes for gaseous phases and every 20 minutes for 20 hours for jammed phases. The displacement of cells in gaseous phases was automatically tracked with TrackMate in Fiji [103], and that in jammed phases was manually tracked with the Manual Tracking plugin of ImageJ.

Collective diffusivity

To determine the collective diffusivity, we adapted the Boltzmann-Matano analysis [104] to the present case of a reaction-diffusion system. Under the assumption that our general reaction-diffusion model, $\partial_t c(y,t) = \partial_y[D(c(y,t))\partial_y c(y,t)] + rc(y,t)$, is valid, we can express the density-dependent diffusivity $D(c)$ in terms of the steady state density profile as follows:

$$D(c(y)) = \frac{r \int_0^y c(y')dy'}{-\partial_y c(y)} \tag{2.1}$$

This equation allows us to estimate $D(c)$ from the exponential growth rate and the steady state density profiles. The steady-state density profiles were determined from the temporal average of the fluorescent intensity of time lapse movies. For the data in Fig. S2c, we averaged the density profile over 20 frames (7 hours) and locally approximated it with a quadratic function by the Savitzky–Golay method [105] to extract $\partial_y c(y)$. We excluded the y-region 20% from the opening where the flow impacted the tail of the density profile, and excluded the y-region 20% from the bottom where $(\partial_y c(y))^{-1}$ was diverging.

Fluid dynamics simulations

The fluid dynamics of the culture medium flow through the cavity structures of our microfluidic devices were simulated using COMSOL. As a simple geometry, we defined a 500 μm × 50 μm × 20 μm supply channel with a 50 μm × 150 μm × 20 μm cavity in the middle. The fluid dynamics was modeled as incompressible Stokes flow subject to no-slip boundary conditions at the walls and a constant flow rate. To see how the flow field depends on external control parameters, we varied the depth of the cavity (30-150 μm) and the flow rate (100 μm/s and 250 μm/s mean flow rate).

2.8   Supplementary Information

Descriptions of Supplementary movies.

- S1: Jamming dynamics and gaseous phases. The movie shows the lengthscale-dependent colonization in a Microfluidic Panflute over 35 hours. While cell populations get jammed in long chambers, they remain gaseous in short chambers. The approach to the steady state takes markedly longer in chambers close to the transition, which is characteristic of critical slowing down near tipping points.

- S2: Formation of a jammed shockwave. The movie shows the movement of the jamming front over 20 hours. The culture medium flow came from the top to the bottom.

- S3: Population decay upon drug injection. The movie shows the decay of a drug-sensitive population over 14 hours upon injection of 10 μg/mL tetracycline. The sharp decrease of the growth rate of cells results in the phase transition from initially jammed to gaseous.

- S4: Invasion of an advantageous strain. The movie shows how a drug-sensitive resident population (dark) is invaded by drug-resistant cells (yellow). The fitness of the established drug-sensitive bacteria are suppressed by the addition of 10 μg/mL tetracycline. Successful invasions are observed 21 hours after the injection of the drug and the advantageous strain.

Theory of colonization

Here, we describe our modeling approach that helps us to interpret and predict the relaxation and steady-state properties of the bacterial populations in our variable length cavities. We begin by describing a general mathematical framework applicable to a wide range of situations. We then restrict the model to our specific experimental setup, which allows us to make a number of simplifying assumptions.

General reaction-diffusion model

In order to describe the combination of growth and cell movement, we employ a reaction-diffusion model for the packing fraction $\Phi(\mathbf{r},t)$ at position $\mathbf{r}$ and time t, which is the concentration multiplied

by the cell volume. In general, the rate of change of the packing fraction is given by

$$\partial_t \Phi(\mathbf{r},t) = -\nabla \cdot \mathbf{j}(\mathbf{r},t) + b[\Phi(\mathbf{r},t)]$$

in terms of the divergence $\nabla \cdot \mathbf{j}$ of a flux $\mathbf{j}$, a three dimensional vector, and the cell production rate $b[\Phi]$, which depends on the packing fraction itself, for exampled $b[\Phi] = r\phi$ in the case of exponential growth with rate r.

The flux $\mathbf{j}$ describes the magnitude and direction of the flow of cells and can be expressed as

$$\mathbf{j} = -D[\Phi(\mathbf{r},t)]\nabla\Phi + \mathbf{V}\Phi$$

in terms of the cell diffusivity D, the gradient $\nabla\Phi$ of the packing fraction and an advection velocity $\mathbf{V}$, a three dimensional vector.

Context-specific simplifications

A number of simplifications can be made due to the specific setup of our experiments. Here, we describe these simplifications, and note under which conditions they might break.

- *Diffusion is purely passive.* The bacteria in our experiments have no motility mechanism and, therefore, diffuse just like passive particles under the influence of thermal collisions with the solvent particles. However, many bacteria have flagella allowing them to swim and perform chemotaxis to chase the source of certain chemical cues. Although the behavior of swimming bacteria can be quite complex, they are often well described by an advection term to describe chemotaxis and an effective diffusivity, which has a non-trivial motility-induced density-dependence [86].

- *Advection is absent.* In other systems, advection may have to be incorporated to describe chemotaxis (pervious point) or the influence of gravity or fluid flow. Fluid flow is a particularly important aspect in the lumen of the gut [106] but also can also arise in microscopic pores, for instance, in skin pores when sebum is exuded [28].

- *The setup is effectively one-dimensional.* The concentration profile in the narrow crypts of our panflute device is approximately uniform along the directions perpendicular to the symmetry axis of the crypts. This allows us to restrict our discussion to the dynamics along the symmetry axis – the *y*–direction. For wide or high crypts, a three-dimensional description is necessary, especially when hydrodynamic instabilities drive motion in the direction perpendicular to *y*. We expect such higher-dimensional dynamics to be a fruitful topic for future work, in particular because it cannot be mapped to an effective Newtonian dynamics (described below).

Under these simplifying assumptions, which match our experimental conditions, we obtain an effectively one-dimensional reaction-diffusion model that reads

$$\partial_t \Phi(y,t) = \partial_y \left[D(\Phi)\, \partial_y \Phi(y,t) \right] + b(\Phi). \tag{2.2}$$

The boundary conditions are fixed by demanding that cells shall not exit through the floor of the chamber, $\partial_y\Phi = 0$, and that the density vanishes at position L, $\Phi(L,t) = 0$.

Linear Stability Analysis

In order to determine the onset of population growth in our microfluidic crypts, we have to determine the conditions for which an empty crypt is stable against an inoculation with cells. To this end, we perform a linear stability analysis of our model in the low density limit.

The linearized reaction-diffusion equation Eq. 2.2 reads

$$\partial_t \Phi(y,t) = D_0 \partial_y^2 \Phi(y,t) + r\Phi. \tag{2.3}$$

in terms of the low-density diffusivity D_0 and the constant growth rate r.

We first expand the cell density as

$$\Phi(y,t) = \sum_{n=0}^{\infty} a_n(t)\varphi_n(y) \tag{2.4}$$

in terms of cosine modes

$$\varphi_n(y) = \cos(k_n y) \qquad k_n = \left(n + \frac{1}{2}\right)\frac{\pi}{L} \tag{2.5}$$

which are orthonormal

$$\langle \varphi_n | \varphi_m \rangle = \delta_{nm} \tag{2.6}$$

with respect to the scalar product

$$\langle f | g \rangle \equiv \frac{2}{L} \int_0^L dy f(y) g(y) . \tag{2.7}$$

Inserting the expansion Eq. 2.4 into the linearized reaction-diffusion equation Eq. 2.3 and then projecting onto the normal modes yields simple amplitude equations,

$$\partial_t a_n = \omega_n a_n , \tag{2.8}$$

where the frequency ω_n of the nth mode is given by

$$\omega_n = -D_0 k_n^2 + r . \tag{2.9}$$

The mode amplitudes a_n therefore obey $a_n = a_n(0)\exp(\omega_n t)$ with the prefactors fixed by the initial conditions.

For the empty state to be linearly stable, we require all ω_n to be negative, meaning that all mode amplitudes exponentially decay to zero. As the slowest growing mode is $n = 0$, this implies $D_0 k_0^2 > r$, or

$$L < L_{\text{est}} = \frac{\pi}{2}\sqrt{\frac{D_0}{r}} , \tag{2.10}$$

revealing the establishment transition discussed in the main text.

Note that the density decay of non-growing particles ($r = 0$), which merely diffuse out of the chamber, is on long times controlled by the slowest decaying mode, $\Phi \propto \exp(-D_0 k_0^2 t)$. Since, at the establishment transition, we have $D_0 k_0^2 = r$, we see that the diffusive "half-life" of the bacteria just equals their doubling time. This confirms the intuition that the establishment transition occurs when the diffusive outflow is balanced by growth.

Steady state at low packing fraction

To explore the nature of the gaseous phase, it is useful to study the limit of low packing fractions, where the diffusivity takes the form [93]

$$D(\Phi) = D_0(1 + \alpha\Phi) + O(\Phi^2) . \tag{2.11}$$

The numerical coefficient α measures the leading order change in diffusivity with increasing packing fraction and depends on the shape of the particles as well as their interactions. For repulsive particles, such as our main model system *Acetobacter indonesiensis*, α is positive. Detailed analytical results are available for hard spheres, yielding $\alpha = 1.45$ [107]. Strong attraction can lead to negative α [93].

When we include the non-linear packing fraction dependence to leading order, we obtain the following equation of motion

$$\partial_t \Phi(y,t) = D_0 \partial_y^2 \left(\Phi + \frac{\alpha}{2}\Phi^2 \right) + r\Phi . \tag{2.12}$$

If we expand $\Phi(y,t)$ in terms of the normal modes as in Eq. 2.5, we find

$$\partial_t a_n(t) = \omega_n a_n - \frac{\alpha}{2} D_0 k_n^2 \langle \varphi_n | \Phi^2 \rangle , \tag{2.13}$$

where $\langle \varphi_n | \Phi^2 \rangle$ is the projection of $\Phi^2(y,t)$ on to the nth mode.

We expect the small density approximation, Eq. 2.13, to be appropriate when L just slightly exceeds L_{est}. Thus, we can introduce the small parameter

$$\varepsilon \equiv \frac{L}{L_{\text{est}}} - 1 \ll 1 . \tag{2.14}$$

Our discussion of the establishment transition has shown that the frequency of the lowest mode vanishes right at the transition, $\omega_0 = 0$, and that the frequencies of all other modes is finite, i.e. $\omega_n = O(1)$.

For ε small but finite, we still have that the higher modes have linear relaxation frequencies of order one, $\omega_n = O(1)$ for $n > 1$, but the frequency of the lowest mode now assumes small positive frequency of order ε,

$$\frac{\omega_0}{r} = -\frac{D_0 k_0^2}{r} + 1 = -\left(\frac{L_{\text{est}}}{L} \right)^2 + 1 \tag{2.15}$$

$$= -\frac{1}{1 + 2\varepsilon + \varepsilon^2} + 1 \approx 2\varepsilon \ll 1 \tag{2.16}$$

Combining $\omega_0 = O(\varepsilon)$, $\omega_{n>1} = O(1)$ with Eq. 2.13 shows that, at steady state, $a_{n>1}$ with $n > 1$ is of higher order in ε than a_0. Thus, to leading order in ε, we have $\Phi(y,t) = a_0 \varphi_0(y,t) + O(\varepsilon^2)$, which simplifies the amplitude equation Eq. 2.13 to

$$\partial_t a_n(t) = \omega_n a_n - \frac{\alpha}{2} D_0 k_n^2 a_0^2 \langle \varphi_n | \varphi_0^2 \rangle . \tag{2.17}$$

The scalar product on the right hand side evaluates in general to

$$\langle \varphi_n | \varphi_0^2 \rangle = \frac{2}{L} \int_0^L dy \cos\left[\left(n + \frac{1}{2}\right) \pi y\right] \cos^2\left(\frac{\pi y}{2}\right) \tag{2.18}$$

$$= \frac{8(-1)^n}{\pi\left(3 + 2n - 12n^2 - 8n^3\right)} . \tag{2.19}$$

As before, we confine our attention to the slowest growing mode, $n = 0$, for which $\langle \varphi_0 | \varphi_0^2 \rangle = 8/3\pi$ leading to the closed amplitude equation,

$$\partial_t a_0 = \omega_0 a_0 - \frac{4\alpha}{3\pi} D_0 k_0^2 a_0^2 . \tag{2.20}$$

the steady state density will be small allowing us to expand

$$\frac{\omega_0}{r} \approx 2\varepsilon \ll 1 \tag{2.21}$$

in terms of

$$\varepsilon \equiv \frac{L}{L_{\text{est}}} - 1 . \tag{2.22}$$

Rescaling time $\tau = rt$ and using the leading order approximations $D_0 k_0^2 \approx r + O(\varepsilon)$ and $\omega/r \approx 2\varepsilon$ (Eq. 2.16), we obtain

$$\partial_\tau a_0 = 2\varepsilon a_0 - \frac{4\alpha}{3\pi} a_0^2 . \tag{2.23}$$

For the inoculation of an initially empty chamber, this logistic differential equation yields the simple prediction

$$a_0(\tau) = \frac{6\pi\varepsilon}{4\alpha} \frac{1}{1 + \exp(-2\varepsilon\tau)} \tag{2.24}$$

up to a shift in time.

To illustrate these results, we consider the example of hard spheres for which $\alpha = 1.45$ is known exactly (from Eq. (6.12) in Ref. [107]). Our lowest order expansion Eq. 2.24 then predicts a packing fraction at the floor of the chamber of $c(y = 0) = a_0 \cos(0) = a_0 = \varepsilon 6\pi/(4\alpha) \approx 3.25\varepsilon$ at steady state ($t \to \infty$). Extrapolating from this lowest order expansion, we may estimate that a chamber length of no more than $\varepsilon_j = 24\%$ above the establishment length is needed for jamming to occur, because then the maximal density at the floor, $3.25\varepsilon_j = 0.64$, approaches random close packing ($\Phi_{\text{rcp}} \approx 64\%$ for monodisperse spheres). This simple estimate of course ignores non-linear feedbacks, which typically leads to an earlier onset of jamming, as seen in Figs. 2b and 3a.

Of particular significance is also the predicted relaxation time to the steady state, the inverse of which is often taken as a measure for the resilience of an ecological system [108]. From the exponent in Eq. 2.24, we see that this relaxation time is given by $1/(2\varepsilon r)$, which is independent of α and, notably, diverges near the establishment transition. Thus, relaxation can take long — much longer than the diffusive exploration of the chamber, which takes about one cell doubling near the establishment transition (the diffusive half-life of particles in a crypt at establishment

length just equals the doubling time, see Sec. 2.8). Therefore, we generically expect a time scale separation between relaxation of the density profile towards the cosine shape (fast) and relaxation of the amplitude of the cosine (slow).

Although the cells in our experiments are neither spherical nor monodisperse, we expect the above results to apply up to pre-factors. For example, since ε remains small up to the jamming transition also in our experiments, one would expect long relaxation times throughout the gaseous phase. Indeed, relaxation in our flow shift experiments took up to 10 h or five doublings (see green curve in Fig. 2.11).

Mechanical analogy predicts steady-state colonization patterns

Let us consider the one-dimensional reaction-diffusion equation for the cell packing fraction $\Phi(y,t)$ at position y and time t

$$\partial_t \Phi(y,t) = -\partial_y J + b(\Phi) \tag{2.25}$$

$$J(y,t) \equiv -D(\Phi)\partial_y \Phi \tag{2.26}$$

where we allow for an arbitrary density-dependence in both the collective diffusivity $D(\Phi)$ as well as the growth rate $b(\Phi)$. As pointed out in the main text, the linear growth rate in our experimental system is to a good approximation constant, which corresponds to $b(\Phi) = r\Phi$. The mathematical treatment in this section is independent from this simplifying condition.

We define the quantity

$$\Pi(\Phi) \equiv \int_0^\Phi d\Phi' D(\Phi') \tag{2.27}$$

such that the diffusive current is given by

$$J = -\partial_\Phi \Pi(\Phi)\partial_y \Phi = -\partial_y \Pi(y) \tag{2.28}$$

where we identified $\Pi(y) \equiv \Pi[\Phi(y)]$ to simplify the notation. Eq. 2.28 formally implies that a gradient of $\Pi(y)$ drives a current just like a conventional pressure gradient would. We therefore call Π effective pressure. Since for passive diffusion[2], we must have $\partial_\Phi \Pi(\Phi) = D(\Phi) > 0$, we can invert the equation of state to obtain a the packing fraction $\Phi(\Pi)$ as function of effective pressure Π.

Next, combining Eqs. 2.25, 2.27 and 2.28 yields at steady state

$$\partial_y^2 \Pi = -b(\Phi) = -\partial_\Pi U(\Pi) \tag{2.29}$$

where we defined an effective potential

$$U(\Pi) \equiv \int_0^\Pi d\Pi' b[\Phi(\Pi')] \tag{2.30}$$

$$U[\Phi(\Pi)] = \int_0^{\Phi(\Pi)} d\Phi' D(\Phi')b(\Phi') \ . \tag{2.31}$$

---

[2]The mechanism of Motility-Induced Phase Separation is based on an active movement (motility), which can generate a negative effective diffusivity [86].

The boundary conditions imply $\Pi(L) = 0$, manifestly ensured through Eq. 2.27, and $\partial_y\Pi(y = 0) = 0$, which we will account for below.

Notice that Eq. 2.29 is formally identical to Newton's equation for a particle at position $\Pi(y)$ at time y freely falling in a potential $U(\Pi)$. Hence, we can use the principle of mechanical energy conservation to immediately predict the velocity $\partial_y\Pi$ of the moving particle in our mechanical analogy, which in our reaction-diffusion problem corresponds to the negative particle current

$$J(y) = -\partial_y\Pi = \sqrt{2\left(U_0 - U(\Pi)\right)}, \tag{2.32}$$

manifestly satisfying the no-flux boundary condition $\partial_y\Pi(y = 0) = 0$. Note that we use the notation $U_0 \equiv U(\Pi_0)$ and $\Pi_0 \equiv \Pi(y = 0)$.

Integrating Eq. 2.32 over the y yields

$$\int_\Pi^{\Pi_0} \frac{d\Pi'}{\sqrt{2\left(U_0 - U(\Pi')\right)}} = \int_0^{y(\Pi)} dy = y(\Pi) \tag{2.33}$$

or

$$y(\Phi) = \int_\Phi^{\Phi_0} \frac{d\Phi'\partial_\Phi\Pi}{\sqrt{2\left(U_0 - U(\Phi')\right)}} \tag{2.34}$$

$$= \int_\Phi^{\Phi_0} \frac{d\Phi'D(\Phi')}{\sqrt{2\left(U_0 - U(\Phi')\right)}} \tag{2.35}$$

where $U(\Phi) = U[\Phi(\Pi)]$, as defined in Eq. 2.31. Calculating $y(0) = L$ gives us the effective chamber length given a maximal packing fraction Φ_0 at the floor ($y = 0$) of the chamber, which is how we determined Figs. 2b and 3a. Since the function $y(\Phi)$ is monotonous, it can also be inverted to determine the position-dependent packing fraction $\Phi(y)$, shown in Fig. 2b for hard sphere,again given the maximal packing fraction Φ_0 at the floor of the chamber.

The integrals in Eqs. 2.35 and 2.31 can be solved numerically without problems for any $D(\Phi) > 0$ and $b(\Phi)$, provided $U(\Phi) < U_0$ along the trajectory.

General approach to compute the phase diagram

Generically, the shape of the potential $U(\Phi)$ will start at $U(\Phi = 0) = 0$ and increase monotonically because $U' = -D(\Phi)b(\Phi) \leq 0$, unless we allow for a region of negative net growth $b < 0$. The behavior near $\Phi = 0$ is quadratic since $U'(\Phi = 0) = 0$ from the no-flux boundary condition and we assume analyticity of D and b. For small Φ, we expect $D' > 0$ suggesting that the potential at first rises faster than a parabola. At larger Φ we expect, instead, a negative slope of $D(\Phi)$ resulting in a flattening of the potential until jamming leads to rapid rise of the potential.

To determine the density at the floor of the chamber, we have to solve the following problem: Let a point mass move down this energy landscape from $\Phi = \Phi_0$ back down to $\Phi = 0$. The time it takes the moving mass to reach $\Phi = 0$ has to equal the length L of the chamber. If the sojourn

time is too small (large) we have to increase (decrease) Φ_0. Mathematically, we can formulate this condition using Eq. 2.35,

$$L = F(\Phi_0) \equiv \int_0^{\Phi_0} \frac{d\tilde{\Phi} D(\tilde{\Phi})}{\sqrt{2\left(U(\Phi_0) - U(\tilde{\Phi})\right)}} \ . \tag{2.36}$$

We have thus obtained an equation that can be used to determine a phase diagram as in Fig. 3a from any $D(\Phi)$ and $b(\Phi)$. Multiple steady states exist if there are multiple Φ_0 values with *identical* sojourn times. The trivial case for which this happens is a simple parabola, which corresponds to the case without density-dependence, $D = \text{const.}$ and $b(\Phi) = r\Phi$. Then, we have a critical length where any density Φ_0 will lead to a marginally stable steady state.

More realistically, multiple steady states occur if the potential fluctuates around a parabola. The density interval supporting multiple steady states is bounded by Φ_0-values for which

$$\partial_{\Phi_0} F(\Phi_0) = 0. \tag{2.37}$$

This condition can be computed explicitly as follows,

$$0 = \partial_{\Phi_0} F(\Phi_0) = \partial_{\Phi_0} \int_0^{\Phi_0} \frac{d\xi D(\Phi_0 - \xi)}{\sqrt{2\left(U(\Phi_0) - U(\Phi_0 - \xi)\right)}} \tag{2.38}$$

$$= \frac{D_0}{2U(\Phi_0)} + \int_0^{\Phi_0} \frac{d\xi D'(\Phi_0 - \xi)}{\sqrt{2\left(U(\Phi_0) - U(\Phi_0 - \xi)\right)}}$$

$$+ \left(D(\Phi_0)b(\Phi_0) - D(\Phi_0)b(\Phi_0)\right) \int_0^{\Phi_0} \frac{d\xi D(\Phi_0 - \xi)}{\left[2\left(U(\Phi_0) - U(\Phi_0 - \xi)\right)\right]^{3/2}} \ , \tag{2.39}$$

where we substituted $\xi \equiv \Phi_0 - \tilde{\Phi}$ in the first line and using Eq. 2.31 to express the derivative of U in the last line. If Eq. 2.39 has any solution there must exist multiple steady states.

Collective diffusion for hard spheres

In general, $D(\Phi)$ is a collective diffusion coefficient as opposed to a tracer diffusivity or self-diffusion coefficient. With purely passive diffusion, $D(\Phi)$ can be decomposed into the product $D(\Phi) = \mu(\Phi)k_B T \partial_\Phi P(\Phi)$ of two terms with an intuitive interpretation:

- $\mu(\Phi)$ is the collective mobility, a transport coefficient that describes the sedimentation velocity and is typically a decreasing function of packing fraction Φ. As a transport coefficient it depends on the equations of motion, and the treatment of hydrodynamics.

- $P(\Phi)$ is the osmotic pressure of the cell suspension, and its derivative is proportional to the (osmotic) bulk modulus, which has to be positive. Because $P(\Phi)$ is a pure equilibrium quantity, it can be readily obtained from Monte Carlo simulations without modeling the surrounding fluid at all.

For a system of hard spheres, a multipole expansion of the effective hydrodynamic interaction [109] can be used to extract the collective mobility for particles immersed in an incompressible fluid. With collective mobility computed using this method, we confirmed the empirical Richardson-Zaki scaling form [110], $\mu(\Phi) = \mu_0(1-\Phi)^\eta$ where μ_0 is the particle mobility in the dilute limit. We extracted $\eta = 5.8$ from a linear regression of $\mu(\Phi)$. The fit and accompanying data are shown in Fig. 2.15, which over the range of packing fractions considered are in good agreement. Similarly, the equation of state of hard spheres is known to be well described by a Carnahan-Starling equation [111]. In terms of the packing fraction, the pressure $P(\Phi)$ is given by, $P(\Phi)/k_BT = (6\Phi/\pi)(1+\Phi+\Phi^2-\Phi^3)/(1-\Phi)^3$. Taken together, we obtain the collective diffusion coefficient via $D(\Phi) = k_BT\mu(\Phi)\partial_\Phi P(\Phi)$, which was used together with $b(\Phi) = r\Phi$ to determine the hard sphere phase diagram Fig. 3a in the main text using Eq. 2.36.

It is worth noting that that the resulting collective diffusion coefficient for hard spheres is merely an approximation designed to capture the non-linear behavior for modest to high packing fractions. Exact results are often available for the linear expansion coefficient α of the diffusivity $D/D_0 \approx 1+\alpha\Phi+$h.o.t. (see e.g. Ref. [93]), valid at low density, which can be useful for estimating the behavior of the gaseous phase at low densities. For instance, in Sec. 2.8, we used the exact result $\alpha = 1.45$ [107] for hard spheres to estimate the steady state density, rather than $\alpha_{approx} = 8 - \eta$ from the above approximation Richardson-Zaki/ Carnahan-Starling approximation.

Proliferating soft disk simulations

To see which phase transitions emerge in a minimal model that only includes proliferation, cell diffusion and cell repulsion, we explicitly simulate a mechanical system of soft disks that undergo Brownian motion and that divide with a constant rate.

Model details

Each particle, i, obeys a stochastic equation of motion for its position in two dimensions, $\mathbf{r}_i = \{x_i, y_i\}$,

$$\frac{d\mathbf{r}_i}{dt} = -\mu_0 \nabla_i U\left(\mathbf{r}^N\right) + \eta_i$$

where μ_0 is the time single particle mobility resulting from the surrounding fluid, η_i is a Gaussian random variable with mean $\langle \eta_i \rangle = 0$ and variance $\langle \eta_i(t) \otimes \eta_j(t') \rangle = 2k_BT\mu_0 \mathbf{1}\delta_{ij}\delta(t-t')$ where k_BT is Boltzmann's constant times the temperature of the fluid and is diagonal for each particle and cartesian component. We solve this equation using a standard first order Euler discretization. In addition to Brownian motion, the particles move in response to a potential $U(\mathbf{r}^N)$ that depends on the full configuration of the system, denoted $\mathbf{r}^N$. At any time, there are N total particles, with N_m maturated mother particles and N_d growing daughter particles. The interaction potential is decomposable into $U\left(\mathbf{r}^N\right) = U_b\left(\mathbf{r}^N\right) + U_r\left(\mathbf{r}^N\right) + U_w\left(\mathbf{r}^N\right)$ where U_b is the bonding potential between mother and daughter particles, U_r is a purely repulsive interparticle interaction and U_w is a confining potential.

The bonding potential is taken to taken to be a simple Hookian spring,

$$U_{\mathrm{b}}\left(\mathbf{r}^N\right) = \sum_{\substack{i \in N_{\mathrm{m}} \\ j \in N_{\mathrm{d}}}}^{N} \frac{\kappa}{2}\left(r_{ij} - b_{ij}\right)^2 \chi_{ij}$$

with stiffness κ, rest length b_{ij}, and $\chi_{ij} = 1$ if particles i and j are a mother daughter pair and $\chi_{ij} = 0$ otherwise. The specific form of the repulsive interparticle potential is taken to be pairwise decomposable

$$U_{\mathrm{r}}\left(\mathbf{r}^N\right) = \frac{1}{2} \sum_{i \neq j = 1}^{N} u_2(r_{ij})(1 - \chi_{ij})$$

where the pair potential $u_2(r_{ij})$, is a WCA potential [112]

$$u_2(r_{ij}) = \begin{cases} 4\varepsilon\left[\left(\frac{\sigma_{ij}}{r_{ij}}\right)^{12} - \left(\frac{\sigma_{ij}}{r_{ij}}\right)^6\right] + \varepsilon & \text{if } r < 2^{1/6}\sigma_{ij} \\ 0 & \text{else} \end{cases}$$

where ε is a characteristic energy scale and

$$\sigma_{ij} = \frac{1}{2}\left(\sigma_i + \sigma_j\right)$$

where σ_i is the characteristic size of particle i. All pairs of particles, excluding bonded mother and daughter pairs, interact with these are excluded volume interactions. Finally, the confining potential restricts the the particles motion to approximately an area $A = L_x L_y$ by imposing a steep potential at $x = 0$, $x = L_x$, and $y = 0$. Specifically, the external wall potential has the form,

$$U_{\mathrm{w}}\left(\mathbf{r}^N\right) = \sum_{i=1}^{N} a\left[e^{-y_i/\xi} + e^{-x_i/\xi} + e^{-(L_x - x_i)/\xi}\right]$$

with a the amplitude of the confining potential and ξ its characteristic length scale.

The mechanical system outlined above is conservative and describes the motion of a collection of overdamped particles with a simplified, local description of hydrodynamics [113]. At long times, absent added external forces, its evolution would be consistent with thermal distribution and would conserve particle number. In order to model the growth of the bacterial population and division of an individual mother daughter pair, we endow the daughter particles with a time dependent effective size through the deterministic equation of motion

$$\frac{d\sigma_i(t)}{dt} = \begin{cases} k & \text{for } t < 1/k \\ 0 & \text{else} \end{cases}$$

with boundary condition $\sigma_i(0) = 0$ and growth rate k. Similarly, to model the budding of the daughter from the mother, the rest distance b_{ij} changes in time with the deterministic equation of motion

$$\frac{db_{ij}(t)}{dt} = \begin{cases} k & \text{for } r_{ij} < \sigma_i \\ 0 & \text{else} \end{cases}$$

with boundary condition $b_{ij}(0) = 0$ and the same growth rate k. When then impose that when the distance between the mother-daughter pair $r_{ij}(t)$ has grown past the effective size of the mother particle, σ_i, we sever the bond potential by $\chi_{ij} \to 0$ between mother-daughter pair ij, provided $t > 1/k$. An illustration of this criteria is shown in Fig. 2.16. This growth rule results in an increasing excluded area of the mother-daughter pair that grows approximately linearly in time. All of the results in the main text and below employ this rule with a fixed k. Growth rules that affect in an exponential increase in the excluded area with time yield qualitatively similar results. Further the results presented are for a fixed growth rate k, but generalizations for populations evolving with a distribution of growth rates are also qualitatively similar, provided the distribution is narrow. Synchronized with the bond breaking event, we add new daughter sites to each of the newly divided particles and reinitialize the size and rest length to 0 for each of them. This last step breaks particle number conservation. An illustration of the subsequent increase in N_{m} is also shown in Fig. 2.16, which absent mitigating factors will grow exponentially in time.

Finally, consistent with the experiments, we apply an absorbing boundary condition at $y = L_y$. The absorbing boundary condition and particle number growth balance at steady-state, resulting in a mean particle number that depends on the geometry and model parameters. We adopt a unit system where $\mu = \varepsilon = k_{\mathrm{B}}T = 1$, and mature particles sizes $\sigma = 1$. This implies that lengths are defined in multiples of the mature particles size, $x \to x/\sigma$ and times in units of the diffusion time for an isolated particle to move its diameter, with $D_0 = k_{\mathrm{B}}T\mu_0$ and accompanying units of time, $t \to t/(D_0\sigma^2)$. The stiffness κ in principle allows for mechanocoupling between the division and local packing environment, with deterministic division occurring when κ is much larger then the local stress on the mother-daughter pair. In this work, we consider this limit and take $\kappa = 100$. The confining potential parameters are taken as $a = 10$ and $\xi = 1$.

Nonequilibrium phase diagram

We have studied the particle based model described above and have found qualitative agreement with both the experimental results and simplified theory presented in the main text. Specifically, we have studied a system with confinement defined by fixed spatial scale $L_x = 15$ and $L_y = 40$, seeded with an $N_{\mathrm{m}} = 10$ initial mother particles. We have found that 10 division cycles is sufficient to relax to a steady state density in the chamber, and evaluated expectation values by averaging over a minimum of 30 additional division cycles. Further, 3-5 independent simulations are used for each expectation value reported. Studies of the effective reaction diffusion model suggests that the function dependence of the system on the length of the chamber enters relative to the establishment length $L_{\mathrm{est}} = \pi\sqrt{D_0/4k}$, so rather then studying different L_y's, we fixed $L_y = L$ and study the dependence on the division rate k, and thus L_{est}.

First, we studied the stead-state density distribution in the chamber. For $L/L_{\mathrm{est}} < 1$, as expected the density in the chamber is 0 at steady-state on average. For $L/L_{\mathrm{est}} > 1$, the particles are able to colonize the chamber, and evolve a stationary density distribution. The distribution can be characterized analogously through local packing fraction $\Phi(y) = \rho(y)\pi/4$ where $\hat{\rho}(y) = \langle\delta(y - y_i)\rangle$. Generally, the discrete size of the particles relative to a flat wall will result in an oscillatory density profile when the overall density is larger, $\rho > 0.1$, which is a result of density correlations

induced by their excluded area. Such an oscillatory density profile is not predicted by the simple reaction diffusion model employed in the main text. In order to make contact with that perspective, we report in Fig. 2.17 density profiles coarse-grained over a the length-scale of the particle[114]. We achieve this using by convoluting the number density with a Gaussian,

$$\rho(y) = \int dy' \hat{\rho}(y') \frac{e^{-(y-y')^2/2\sigma^2}}{\sqrt{2\pi\sigma^2}}$$

which smooths the profile out. Further, we consider the contribution of the density only from the mother particles, and evaluate expectation values for times that are integer multiples of $1/k$.

Fig. 2.17 specifically reports conditions for $L/L_{est} = \{1.2, 2, 4\}$. We also compare those calculations to the predictions of the reaction diffusion model. For $L_y/L_{est} = 1.2$, the density is small enough that we find good agreement with the predicted cosine profile, $\Phi(y) = \Phi(0)\cos(\pi y/2L_y)$. At elevated L/L_{est}, deviations of the cosine profile are found and specifically at $L_y/L_{est} = 4$, the distribution is flat in the interior of the chamber with an exponential boundary layer that brings the packing fraction to 0 at $y = L$. Using a parameterization of the collective diffusion constant $D(\Phi)$, evaluated by computing the packing fraction dependent mobility $\mu(\phi)$ that is well described by $\mu(\phi) \approx \mu_0 \exp(-1.70\Phi - 0.18\Phi/(1-1.33\Phi))$, and the equation of state well described by $P(\Phi)/k_B T \approx 1.27\Phi + 2.55\Phi^2 - 9.35\Phi^3 + 42.72\Phi^4$ of the WCA disks, consistent with previous estimations,[115, 116] we can numerically solve the reaction diffusion equation and determine the packing fraction profile for $L/L_{est} = 4$. This predicted profile is in good agreement with the coarse-grained profile from the simulations.

To estimate the boundaries between the extinct, established, and jammed phases, we have computed the coarse-grained value of the packing fraction at the wall as a function of L/L_{est}. This is shown in Fig. 2.18. As anticipated by the reaction diffusion analysis, the establishment transition occurs for $L/L_{est} \approx 1$, which is consistent with our findings that $L < L_{est}$ the chamber is empty at steady-state. For $L > L_{est}$ the maximum packing fraction gradually increases until $L = L_{jam} \approx 3.3$ where for this two-dimensional system we find an abrupt change in the maximum packing fraction. The amplitude of this change is small, reflecting the small change in the density upon freezing of the WCA disks, which is around 2% [117]. Indeed, the pressure measured at the wall at $y = 0$, computed from the average force per unit length of wall, $p_w = -\sum_i^N \langle dU_w/dy_i \rangle/L_x$, surpasses the coexistence pressure for the freezing of WCA spheres at this value of L. As illustrated in Fig. 2 in the main text, for $L > L_{jam}$ the system exhibits noticeable crystallinity.

Self diffusion calculations

In order to estimate the self-diffusion coefficient in the chamber as a function of L/L_{est}, we consider only the diffusivity in the x direction, the direction orthogonal to the open end. This is because there exists a net mass current in the y direction, so motion is convective in that direction rather than diffusive. For diffusion in the x, we use the standard definition

$$D_s(\Phi) = \lim_{t \to \infty} \frac{1}{2t} \langle [x_i(t) - x_i(0)]^2 \rangle$$

as the long time limit of the mean squared displacement. However two difficulties arise in applying this relation to extract the self diffusion. First, particles leave the chamber at a finite rate, due to the absorbing boundary condition at $y = L$. This requires that we average particles' displacements only up to their lifetime in the chamber. In order to gather sufficient statistics and increase the lifetime of individual particles, we use a larger chamber $L_y = L = 80$. Second, the finite size of the chamber in the x direction, L_x means that particles will only exhibit diffusive dynamics for mean squared displacements $\sqrt{\langle [x_i(t) - x_i(0)]^2 \rangle} < L_x/2$, and thus the long time limit strictly goes to 0. We find using $L_x = 30$ to be large enough that there exists a sufficient separation of timescales between the onset of diffusive motion and its reduction due to confinement that we easily extract a pseudo-time independent self-diffusion constant. This data is reported in Fig. 2.

Theory of Invasion

For a foreign strain to invade a pre-occupied chamber, an invader has to overcome two hurdles: #1) *Infiltration*: the invader diffuses from the outside against the gradient to reach a favorable position near the floor of the chamber. #2) *Take over*: the invader's descendants displace the resident population through a combination of chance (genetic drift) and competitive advantage.

Our experimental observations in combination with our simulations indicate that the main reason for the colonization resistance is the difficulty for outside cells to diffusively penetrate chambers that are already filled. Infiltration is rare even in gaseous chambers, but nearly impossible in jammed populations where a narrow strip of founder cells at the floor of the chamber is insulated from the outside by diffusion barrier of descendant cells. Accordingly, the biggest impact of the antibiotic occurs in cavities that, due to the growth rate detriment of the resident, become unjammed and hence invadable (Fig. 4). The larger the growth rate detriment, the larger the range of chamber length that are driven across the tipping point.

In the limit of weak selection, and large chamber population size, infiltration happens on a much faster time scale than take over. This allows to analyze the dynamics in two separate steps. The second, takeover, step is familiar from well-mixed populations. The rate of successful take over depends on the competition between selective advantage of the faster growing invader and genetic drift. The first challenge, however, uniquely depends on the spatial structure of the colonized cavities, which is why we mainly focus on the infiltration step.

The infiltration step is best analyzed backward in time. As we follow the lineage of a randomly chosen cell backward in time, it is advected towards the floor of the chamber, reflecting the intuitive location advantage discussed above. A balance between self-diffusion and advection leads to a steady state lineage distribution, whose extent scales as the ratio of self-diffusivity and advection velocity. While the advection velocity is very similar between gaseous and jammed populations, self-diffusion differs dramatically, by four orders of magnitude, compressing the ancestor distribution in the jammed population to just few cell layers at floor of the chamber.

Our mathematical analysis in the next section shows that the neutral invasion success of an injected invader is proportional to $1/N$ times the ratio of the invader density in the supply channel and the mean density of the population. This shows that gaseous population do enjoy some col-

onization resistance, compared to well-mixed populations for which the neutral invasion success would just be $1/N$.

Yet, the colonization resistance of gaseous populations still is weak compared to partially-jammed populations. Their infiltration is nearly impossible, as it is exponential in the ratio of the thickness of the jammed fraction and the thickness of the founder population, which is at most several cell diameter. The founder population at the floor of the chamber is essentially isolated from the supply channel, through the constant shedding of jammed cells acting as diffusion barrier for any invader. Invasion can only be achieved if this diffusion barrier is broken down, say by an antibiotic treatment or chamber deformation or increase in chamber flow.

Finally, we discuss the case where the growth rate of the resident is reduced by the action of an antibiotic, as done in our experiments. Invadable, gaseous, populations become invaded at rate that is increased by factor of $N_e s$, where $s \ll 1$ is the growth rate defect and $N_e \gg 1$ is the effective population size of the chamber. The situation is similar to well-mixed populations. The only difference is that, due to the spatial structure of the population, $N_e/N < 1$ is mildly and strongly reduced in the gaseous and jammed states, respectively.

Tracking lineages backward in time

To model infiltration and neutral take over, we generalize an analysis of "gene surfing" [118] to include a distinction between collective diffusion and self-diffusion. Suppose we sample a cell at position ξ at present time τ and seek to determine the probability density $G(y,t|\xi,\tau)$ that the ancestor of the cell was at position y at earlier time t. G then describes backward in time the position of the cell's lineage, which is subject to self-diffusion and advection (no proliferation). G therefore satisfies a generalized diffusion or Fokker-Planck equation, which takes the form

$$\partial_t G(y,t|\xi,\tau) = -\partial_y j_l(y,t) \tag{2.40}$$

$$j_l(y,t) = -D_s\partial_y G - (v_g + v_s)G \tag{2.41}$$

$$v_g \equiv j_p/c \tag{2.42}$$

$$v_s \equiv -D_s\partial_y \ln(c) , \tag{2.43}$$

where D_s is the self-diffusivity and the particle current j_p is given by

$$j_p = -D_g\partial_y c + v_p c , \tag{2.44}$$

where $v_p(y,t)$ is the particle velocity at (y,t) due to any external force.

The key part here is the contribution of the lineage current due to self-diffusion. The mathematical form $v_s = -D_s\partial_y \ln(c)$ is fixed by the requirement that, for $v_g = 0$, $G \propto c$ must be a steady sate solution with vanishing current.

Suppose, the chamber population has reached a steady state and is large enough so that we can ignore density fluctuations. Assuming there is no external force, $v_p = 0$, the steady state of the ancestor distribution is then given by

$$G(y) = c(y)^{1+\frac{D_g}{D_s}}/\mathcal{N} , \tag{2.45}$$

where $\mathcal{N}$ is a normalizing factor,

$$\mathcal{N} = \int_{y=0}^{L} dy\, c(y)^{1+\frac{D_g}{D_s}} \tag{2.46}$$

From this, we can conclude that one particle injected at y, will after relaxation in the cavity take up
a fraction

$$u(y) = c(y)^{\frac{D_g}{D_s}} / \mathcal{N} . \tag{2.47}$$

This expression is particularly useful for the gaseous phase where gradient- and self-diffusivity are
nearly identical. In this case, we have an approximately cosine density profile and, with $D_g = D_s$,
we obtain

$$u(y) \approx \frac{8}{\pi^2} \frac{c(y)}{\bar{c}} \frac{1}{N} , \tag{2.48}$$

where $\bar{c} = N/L$ is the mean population density in the chamber. This expression shows that the
neutral invasion success is much less than the well-mixed expectation $1/N$ because the invading
cell has to enter from the supply where the cell density is very low.

In the case of a jammed population, the above expressions are not so useful because they require
us to know the minute spatial density variations in the jammed phase. Instead, we can exploit the
fact that the density hardly varies apart from a boundary layer near the exit of the chamber. A
vanishing particle current at steady state requires

$$-D_g \partial_y c(y,t) = r \int_0^y dy'\, c(y',t) \approx rc_0 y , \tag{2.49}$$

where we used $c(y,t) \approx c_0$ in the last step. Hence, the steady state ancestor distribution is a decay-
ing Gaussian,

$$G(y) = \exp\left[-\frac{r}{2D_s}\left(1 + \frac{D_s}{D_g}\right)y^2 \right] / \mathcal{N} . \tag{2.50}$$

Since $D_s/D_g \ll 1$ in the jammed phase, we conclude that fixation becomes small very rapidly when
$y > \lambda_s \equiv \sqrt{2D_s/r}$.

In our experimental system, we found that λ_s is about one cell diameter and the thickness of
the jammed fraction was about 50 cell diameters, even just after the tipping point. It is, therefore,
appropriate to think of the jammed populations as diffusively isolated from the outside environ-
ment.

Supplementary Table

Supplementary Figures

Species	Strain	Note	Medium	Scale-dependent colonization	Reference
E. coil	MG1655		LB + 0.2% BSA	Not observed	
E. coil	UG2441	Less adhesive Non-motile	LB + 0.2% BSA	Not observed	[119]
B. subtilis	HV1235	Matrix mutant Non-motile	LB	Not observed	[120]
V. cholerae	JY287	Matrix mutant Non-motile	LB + 0.2% BSA	Observed	[121]
A. pasteurianus	LFM13	Fly-gut derived Non-motile	MRS	Observed	[76]
A. tropicalis	LFM14	Fly-gut derived Non-motile	MRS	Observed	[76]
L. lactis	NZ9000	Non-motile	GM17	Observed	[122]

Table 2.1: Strains cultured in panflute devices. Scale-depedent colonization was observed across
multiple species (see Fig. 2.7), but was not observed for strains which were highly adhesive to
walls or had a strong capability of bioflim formation or filamentation.
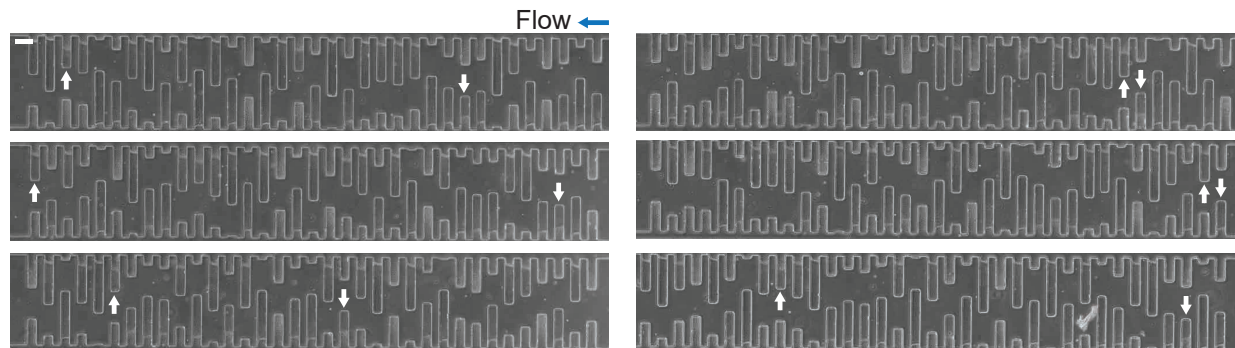
Figure 2.5: Colonization patterns in randomized panflutes. The effect of anterior populations in the
same row was tested by randomizing the order of chambers. The transition to a phase-separated
state was observed independent of the order of the chambers. White arrows show the onset of
jamming. The scale bar indicates 100 μm.
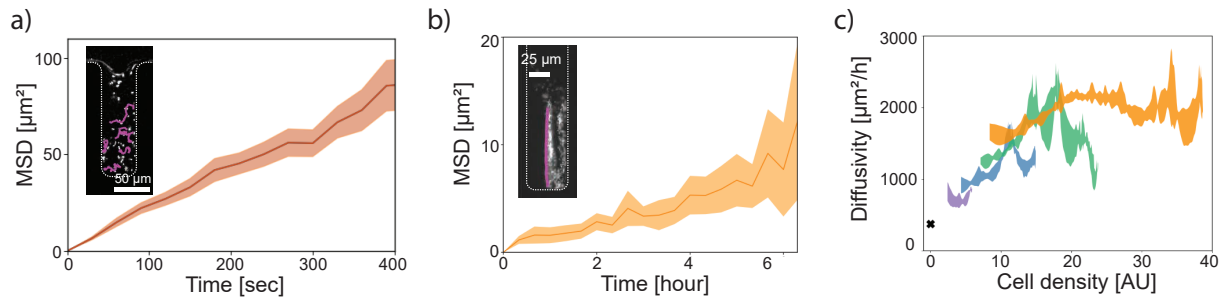
Figure 2.6: Measuring self-diffusivity and collective diffusivity. (a) Self-diffusivity was measured by tracking single cells in gaseous phases (inset: a snapshot of single-cell tracks). The self-diffusivity was calculated as 376 ± 6 µm^2/h from the mean square displacements in the horizontal direction. The error was estimated from fitting. (b) Diffusivity in jammed phases was estimated by manually tracking lineages (inset: a snapshot of a lineage). The diffusivity was calculated as 0.62 ± 0.02 µm^2/h from the mean square displacements in the horizontal direction. (c) Collective diffusivity was calculated from steady-state density profiles (see Method) of gaseous phases in 4 chambers with various depths (the colors show different chambers in the same panflute). The measured collective diffusivity showed a trend of unimodality. The black cross shows the self diffusivity measured in (a). The errors were estimated from the smoothing parameters.
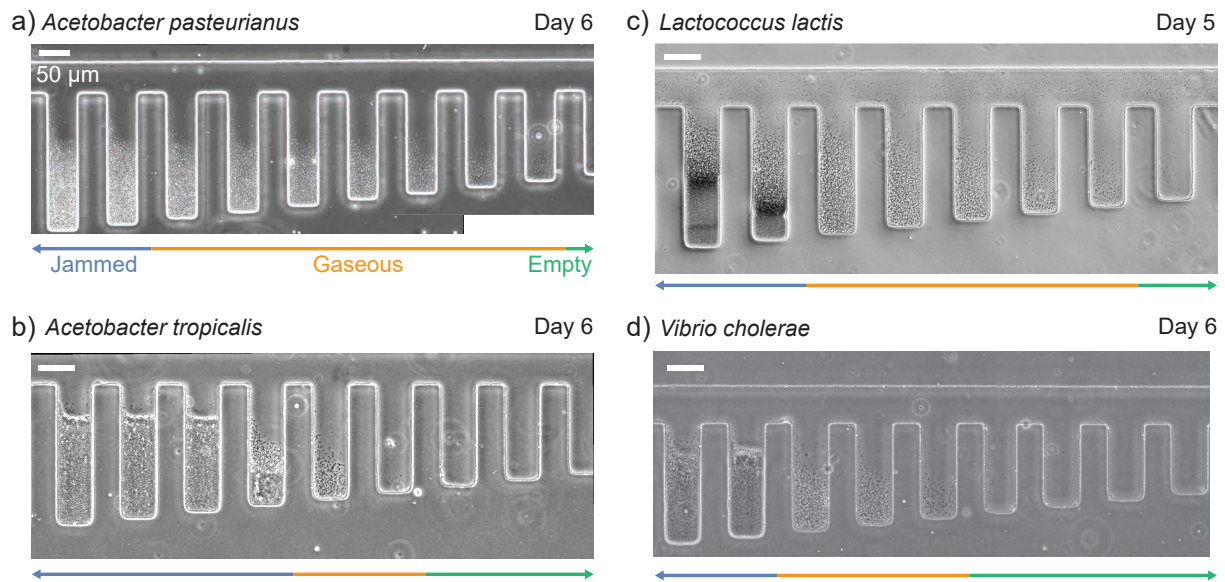
Figure 2.7: Three colonization phases are observed in different bacterial species. Pictures were taken after 5-6 days of incubation in microfluidic devices. Despite biofilm formation (b) and nutrient depletion (c), we observed qualitatively similar colonization patterns. Scale bars indicate 50 µm.
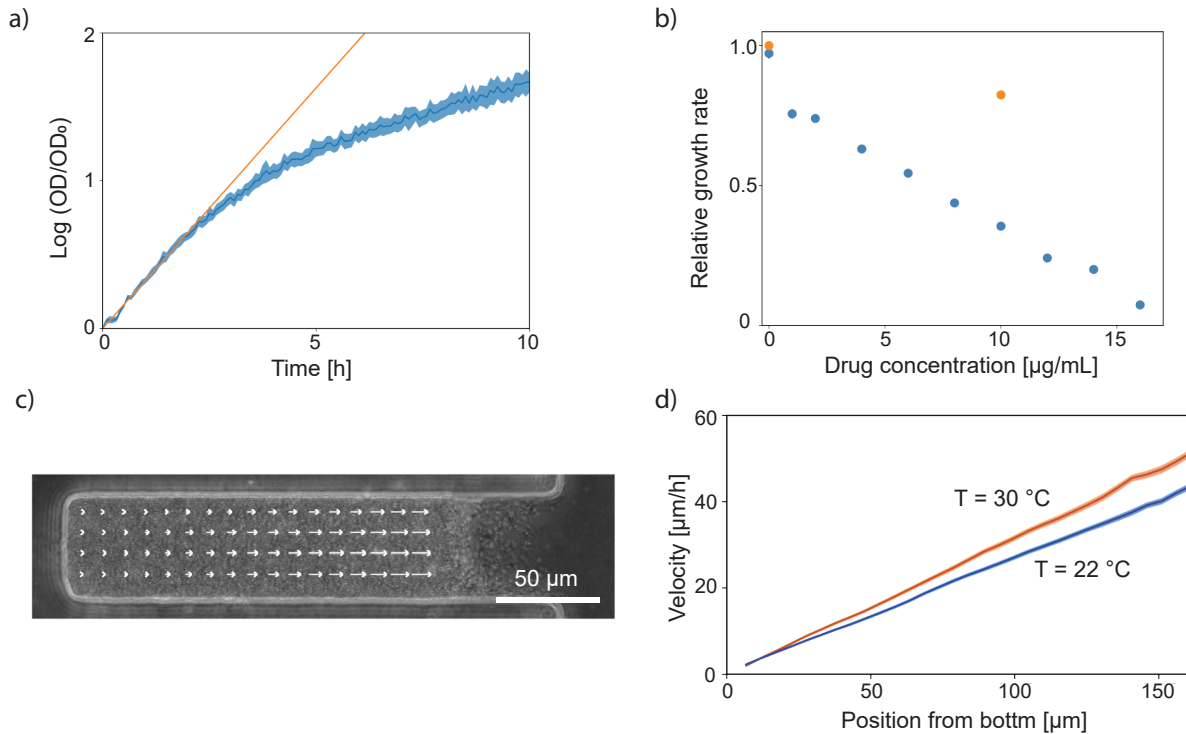
Figure 2.8: Growth rate measurements with a plate reader and particle image velocimetry (PIV). (a) The growth rate of *Acetobacter indonesiensis* was measured with a plate reader. The maximum growth rate at 30 °C was estimated as 0.325 ± 0.003 h^{-1} from the initial growth of 4 independent populations. (b) The growth rate of tetracycline-sensitive (blue) and resistant (orange) cells was measured with various drug concentrations and normalized by the the growth rate of drug-resistant cells in the absence of the drug. The minimum inhibitory concentration was estimated about 17 µg/mL by extrapolating the plot. The averaged growth rate for each condition was calculated from 4 replicas. (c) A schematic of PIV analysis. Arrows show the local velocity of the positions. The length of arrows is proportional to the local velocity. (d) The local velocities of cells at high temperature (red, 30 °C) and low temperature (blue, 22 °C) were linear functions of the position from the bottom of a microfluidic chamber. The solid lines were the local velocities averaged over 3 hours, and the shaded regions show the standard error of mean. The growth rate of cells was derived from the slope of the linear function as 0.332 ± 0.007 and 0.280 ± 0.001 h^{-1} at high and low temperature respectively.
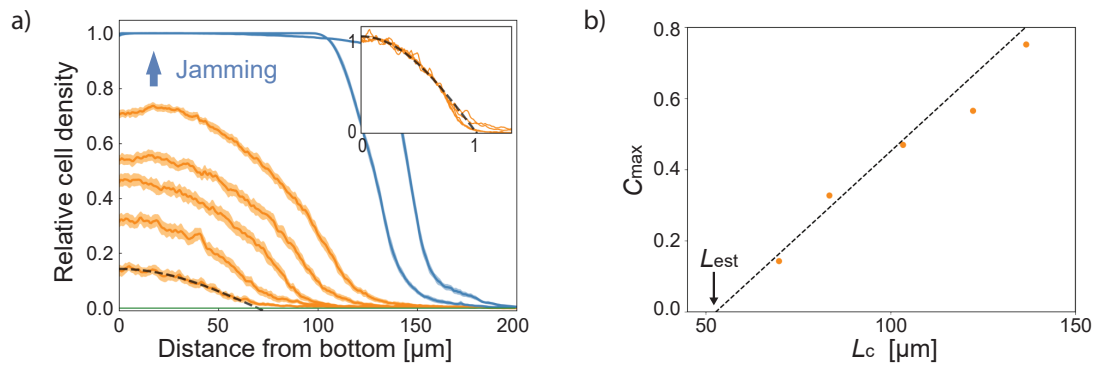
Figure 2.9: Density profiles of gaseous phases can be scaled to approximately collapse onto a master curve. (a) The steady-state density profiles in a Microfluidic Panflute device. The plot is taken from Fig. 1d. The density profiles in the gaseous state can be well approximated by the function $c_{max} \cos(\pi x/2L_c)$, which can be seen in the rescaled plot showing c/c_{max} vs. x/L_c (inset). (b) Plotting L_c vs. c_{max} yielded a near linear relationship in the gaseous state. Extrapolating the linear fitting of the lowest three points to vanishing density yielded an estimate of the establishment length $L_{est} \approx 53 \pm 7$ µm. The error was estimated from fitting. By comparison, our linear stability analysis predicted $L_{est} \approx 53 \pm 1$ µm (see main text).
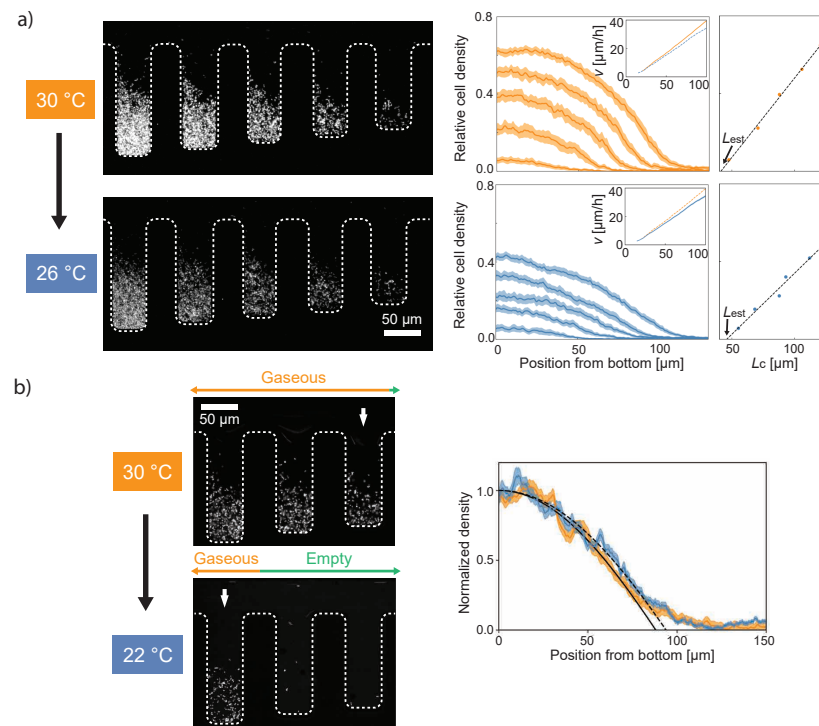
Figure 2.10: The establishment length L_{est} shifts upon a temperature change. We performed two temperature shift experiments, where we inoculate a panflute at one temperature and, after sufficient relaxation, shift to another temperature, after which we let the system relax again. (Relaxation often took more than 5 hrs.) (a) 30 °C to 26 °C. Right: The density profiles changed within the different crypts changed substantially the temperature change. Densities are consistently higher at 30 °C (orange) than at 26 °C (blue). The profiles were measured at steady states with fluorescent microscopy. The insets of the plots show PIV measurements whose slopes indicated the growth rates (see Fig. 2.8c and d). The growth rate decreased to 87.2 ± 0.8 %. The shift of L_{est} was analyzed by determined by extrapolating the relation between cavity length and maximal population density at the floor of the crypts to vanishing cell density, similarly to Fig. 2.9. We found that the establishment length L_{est} increased by 112 ± 11 %. This change was consistent with our theory $L_{est} \propto 1/\sqrt{r}$ ($1/\sqrt{0.87} \sim 1.07$). (b) The establishment length shifted upon the temperature change (from 30 °C to 22 °C). The steady-state density profiles at 30 °C (orange) and 22 °C (blue) were fitted by a cosine function (black solid and dashed lines, respectively) and normalized. The establishment length was defined by the x-intercept. The relative change of this critical length (6.6 %) was consistent with our theory predicting it to be given by the square root of the relative growth rate change (8.6 %, Fig. 2.8d). Note that, while these temperature shift experiments are consistent with a pure growth rate change, they come with the caveat that, besides growth rate, additional cell traits might be affected that influence the phase behavior, for instance, the shape of the cells or their intercellular mechanical interactions.
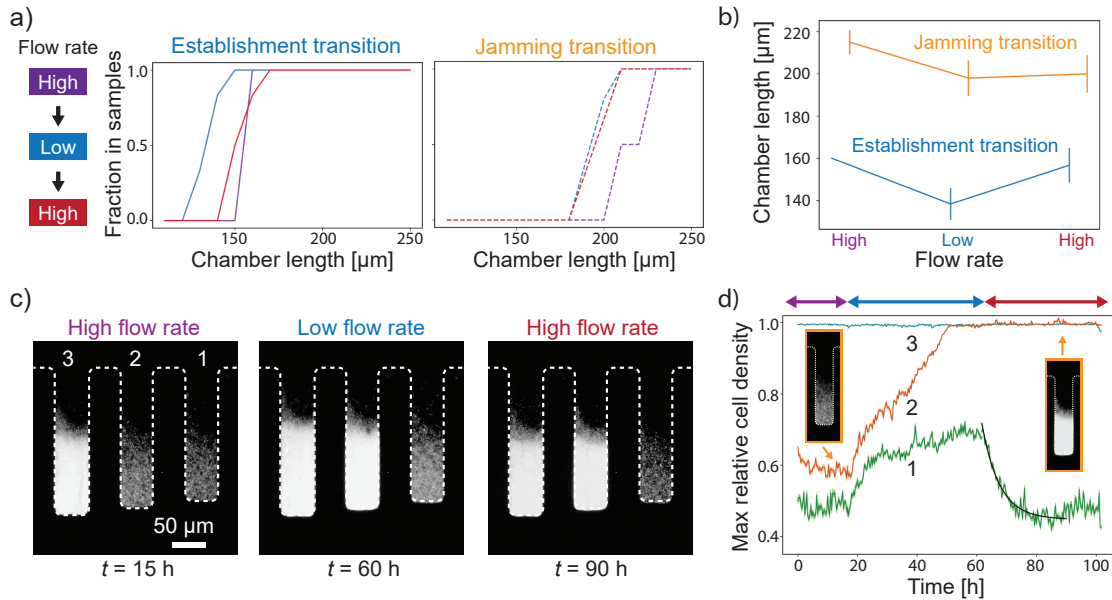
Figure 2.11: Phase shift and bistability upon flow rate change. This figure documents how colonization patterns in the Microfluidic Panflute changed as we changed flow rates from "High" (purple, 0.8 µL/h) to "Low" (blue, 0.3 µL/h) and back to "High" (red), while allowing the populations to reach steady state after each flow rate change. Note that a flow rate increase (decrease) corresponds to a decrease (increase) in the effective chamber depths (see Fig. 2.12). (a) The fraction of occupied chambers (left) and the fraction of jammed chambers (right) are shown as a function of chamber size (incremented by 10 µm). The lines are colored according to the state diagram (left). $n = 3\text{-}6$ for each chamber length. Note that, while the critical length for establishment (left) shifted reversibly as the flow rates was changed, we found hysteresis in the jamming transition (right). (b) The average transitional lengths extracted from (a) are displayed. The error bars show the standard error of the mean. The point without the error bar means that all samples had their establishment transition at the same (discrete) chamber length. (c,d) Time tracking of populations growing in the same Microfluidic Panflute. (c) Steady state snapshots of chambers that are near the jamming transition. Note that, while the occupancy pattern of chambers 1 and 3 changed reversibly, chamber 2 showed hysteric behavior, indicating bistability. (d) Dynamics of the maximal cell density at the floor of the chambers as the flow rate was cycled. Colored lines show the temporal dynamics of the maximum relative cell density in each chamber. The density profiles in the chambers were calculated by averaging the fluorescence across the horizontal direction at each time point. The shaded region shows the standard error of the mean. Two representative snapshots for two stable states of chamber 2 are shown in the insets. The black line shows an exponential fit to the population decay. The decay time was 5.9 ± 0.4 hour (the error was estimated from fitting).
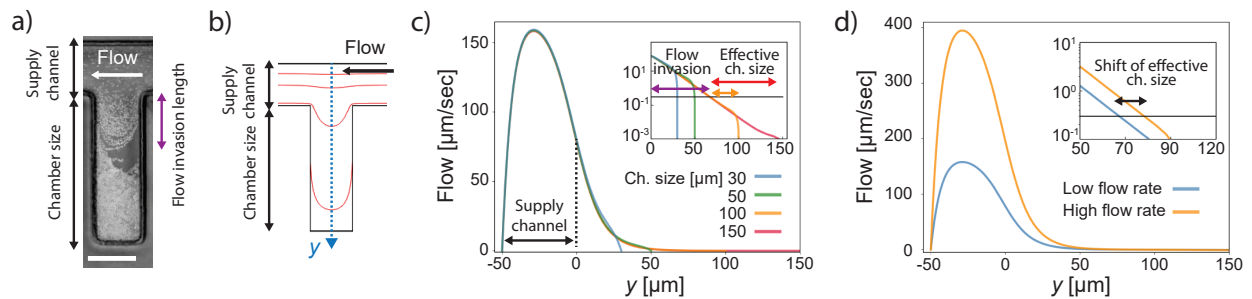
Figure 2.12: Simulations of the hydrodynamic flow fields in the Microfluidic Panflutes. (a) Stream-
lines of the flow were visualized by overlaying 90 frames taken every 2 seconds. The trajectory
of cells showed that the typical scale of the flow invasion length was about 60 μm. The scale bar
shows 50 μm. (b) The hydrodynamics in our microfluidic devices were simulated using COMSOL.
Red lines show streamlines. (c) The horizontal flow velocity along the blue dotted line in (b) is
shown as function of vertical position y. Note that the flow rapidly decays from the opening ($y = 0$)
towards the floor of the cavity. The inset shows the flow profiles in a semi-log scale. We define
an arbitrary threshold flow velocity (0.3 μm/s, the black line in the inset) to define the flow inva-
sion length and the effective chamber length, shown as the purple arrow and the orange (100-μm
chamber) and red (150-μm chamber) arrows, respectively. The flow invasion length is constant for
chamber sizes beyond 100 μm. (d) The effective chamber size gets shorter by 10 μm when the flow
rate changes from low (blue, 100 μm/s average flow rate) to high (orange, 250 μm/s average flow
rate), shown as the black arrow in the inset. Note that the shift of the effective chamber size is not
sensitive to the choice of the threshold flow velocity.
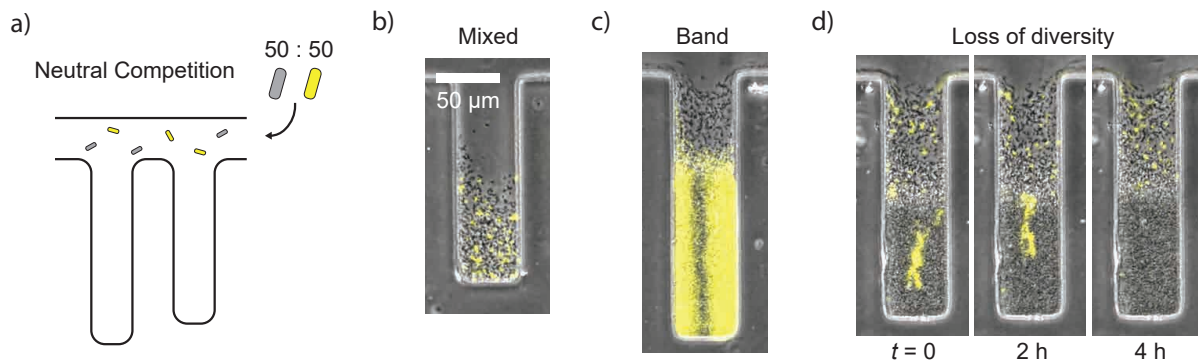
Figure 2.13: Neutral dynamics of mixed cultures reveal suppressed lineage diffusion in jammed
population. (a) A schematic of neutral competition experiments. A 50:50 mixture of wild-type
and labeled invader strains was inoculated into unoccupied chambers without antibiotics. (b) La-
beled cells were sparsely distributed in a gaseous phase. (c) Steric interactions and proliferation
produced band-like patterns in a jammed phase. The population dynamics were dominated by a
small number of cells at the bottom of a cavity. (d) Diversity was rapidly lost in a jammed phase.
A cluster of GFP-tagged cells was pushed out of the chamber by the population growth in a few
generations.
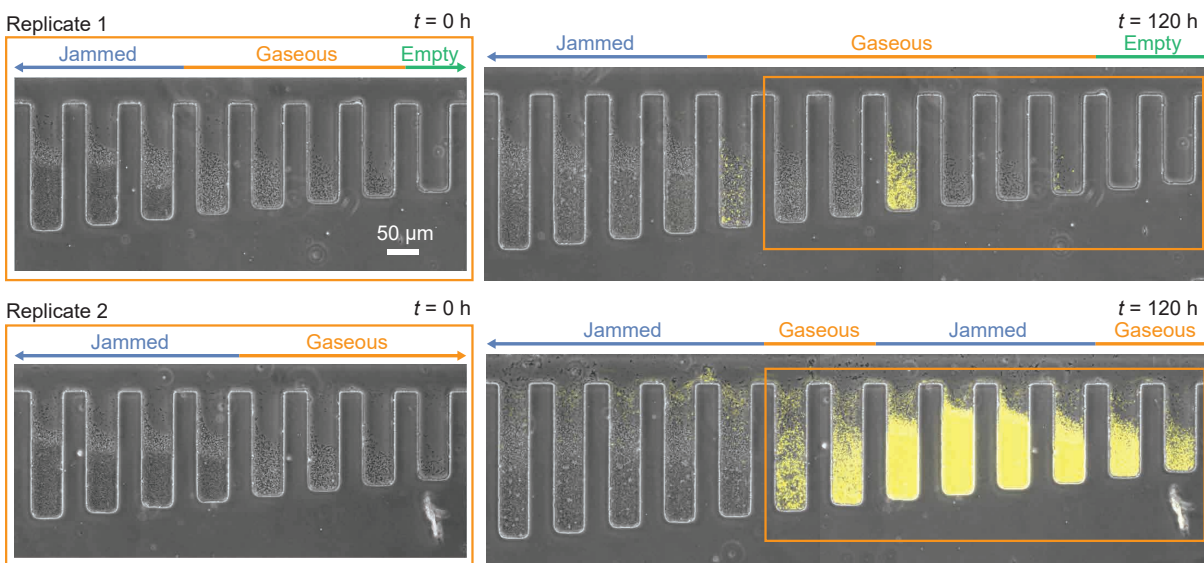
Figure 2.14: Replicas of invasion experiments with 10 µg/mL tetracycline. Replicas from other rows on the same microfluidic chip. Orange frames show the same positions. Colonization resistance of the jammed phases was consistently observed, while the rate of invasion varied across replicas (less successful in the replica 1, and more successful in the replica 2).
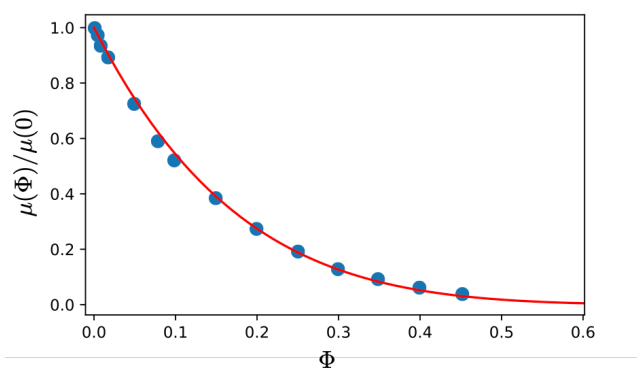
Figure 2.15: Collective mobility with complete many-body hydrodynamic interactions (blue circles) and a fit to the Richardson-Zaki scaling form (red line).
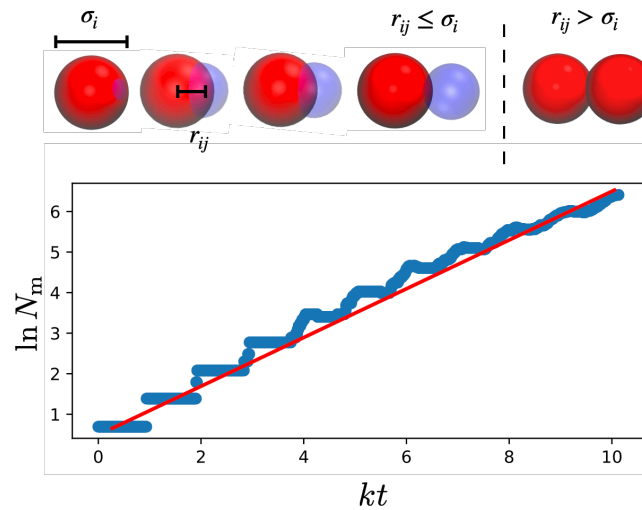
Figure 2.16: Illustration of the growth and division. (top) Illustration of the mechanical model of division of a mother (red) daughter (blue) particle pair, where the characteristic size of the mother is σ_i and its displacement from a daughter is r_{ij} (bottom) Illustration of the subsequent exponential proliferation of particles in time over 10 division times. The red line is a guide to the eye.
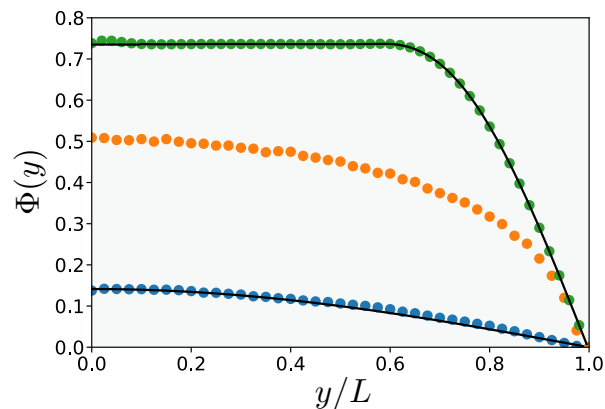
Figure 2.17: Coarse-grained packing fraction profiles computed from simulations at $L/L_{\text{est}} = \{1.2, 2, 4\}$ (blue, orange and green) compared to the analytical predictions of the reaction diffusion model (solid lines).
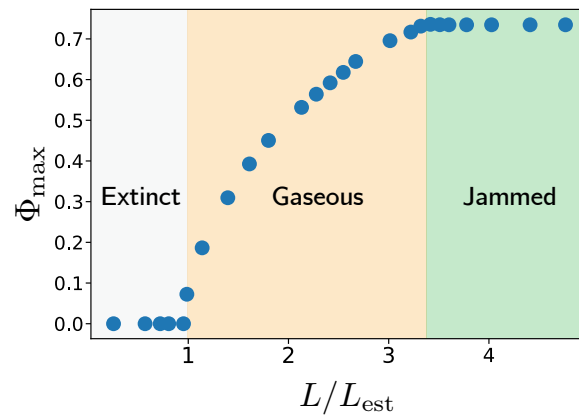
Figure 2.18: Phase diagram for the proliferating soft disks determined by the maximum coarse-grained packing fraction in the chamber.

Chapter 3

Impact of crowding on the diversity of expanding populations

A jammed cellular population exhibits characteristic pushing dynamics upon the population growth. The spatially-structured growth makes the ecological and evolutionary dynamics distinct from a well-mixed population. For example, the excess of mutational jackpots has been reported in range expansion of microbial colonies [123]. However, we find that the low end of the site frequency spectrum follows the same power-law decay in a well-mixed case, even though the underlying mechanism is totally different. Combining analytical models, agent-based simulations, and plate and microfluidic experiments, we characterize the clone size distribution in a jammed population. We also discuss a practical sampling strategy to capture the whole range of the site frequency spectrum.

The remainder of this chapter was submitted to the bioRxiv preprint server as

3.1   Abstract

Crowding effects are key to the self-organization of densely packed cellular assemblies, such as biofilms, solid tumors, and developing tissues. When cells grow and divide they push each other apart, remodeling the structure and extent of the population's range. It has recently been shown that crowding has a strong impact on the strength of natural selection. However, the impact of crowding on neutral processes remains unclear, which controls the fate of new variants as long as they are rare. Here, we quantify the genetic diversity of expanding microbial colonies and uncover signatures of crowding in the site frequency spectrum. By combining Luria-Delbrück fluctuation tests, lineage tracing in a novel microfluidic incubator, cell-based simulations, and theoretical modeling, we find that the majority of mutations arise behind the expanding frontier, giving rise to

clones that are mechanically "pushed out" of the growing region by the proliferating cells in front.
These excluded-volume interactions result in a clone size distribution that solely depends on *where*
the mutation first arose relative to the front and is characterized by a simple power-law for low-
frequency clones. Our model predicts that the distribution only depends on a single parameter, the
characteristic growth layer thickness, and hence allows estimation of the mutation rate in a variety
of crowded cellular populations. Combined with previous studies on high-frequency mutations,
our finding provides a unified picture of the genetic diversity in expanding populations over the
whole frequency range and suggests a practical method to assess growth dynamics by sequencing
populations across spatial scales.

Significance Statement

Growing cell populations become densely packed as cells proliferate and fill space. Crowding
prevents spatial mixing of individuals, significantly altering the evolutionary outcome from estab-
lished results for well-mixed populations. Despite the fundamental differences between spatial and
well-mixed populations, little is known about the impact of crowding on genetic diversity. Looking
at microbial colonies growing on plates, we show that the allele frequency spectrum is character-
ized by a simple power law for low frequencies. Using cell-based simulations and microfluidic
experiments, we identify the origin of this distribution in the volume-exclusion interactions within
the crowded cellular environment, enabling us to extend this findings to a broad range of densely
packed populations. This study highlights the importance of cellular crowding for the emergence
of rare genetic variants.

3.2 Introduction

Environmental factors often structure the spatial organization of growing cellular populations, such
as microbial biofilms [124], developing embryos and differentiating tissues [125], as well as solid
tumors [126–129]. Advances in lineage tracing techniques are progressively revealing that in many
of these cases growth is non-uniform across the population, as it strongly depends on the mechan-
ical and biochemical cues experienced by each cell [127, 128, 130–137]. Non-uniform growth can
favor individuals based on their spatial locations rather than their fitness [55, 129, 138–140] and as
such can dramatically impact the evolutionary fate of the population.

   The interplay between evolution and growth has been extensively investigated in the context of
range expansions, in which populations grow by invading surrounding virgin territory [141–147].
In cellular range expansions, growth is often limited to a thin layer of cells at the expanding front
of the population (the *growth layer*) due to processes like nutrient depletion, waste accumulation,
mechanical pressure, or quorum sensing in the bulk [40, 41, 148–152]. Recent studies have re-
vealed that this growth constraint generates an excess of high-frequency mutations in microbial
colonies [123] and colorectal cancer xenografts [129]. Remarkably, the size distribution of these
large clones is exclusively determined by the surface growth properties of the population through
a phenomenon called allele surfing [141, 153].

The distribution of low-frequency mutations, however, remains an open question. Assuming a mutation rate of 10^{-3} mutation/genome/generation (typical of microbes) and a population size of 10^8-10^9 cells, a total of 10^5-10^6 mutations are generated during population growth. Yet, experimentally only approximately 0.001 % of these mutations have been captured by population sequencing in the case of bacterial colonies and tumors [123, 154–156]. This suggests that low-frequency mutations constitute the majority of genetic diversity in the population, but since their frequency is often below the detection limit of population sequencing, they go unaccounted for. As a single mutant can be sufficient to drive drug resistance [138], its quantification is imperative to better understand the emergence of resistant cells after drug treatment. While several groups have recently revealed the dynamics of small clones by multicolor lineage tracing in solid tumors [128, 129, 135], a quantitative understanding of the dynamics of low-frequency mutations is still lacking. Here, we address this gap by investigating the dynamics of low-frequency mutations utilizing an expanding microbial colony as a model system.

To probe the low-frequency end of the mutational spectrum, we adapt the classic Luria-Delbrück fluctuation test, normally used to infer mutation rates in well-mixed populations [157], to microbial colonies. We find that the vast majority of mutations occurring during growth are present at very low frequencies and characterized by a clone size distribution that decays faster than that observed at high frequency [123]. To investigate the origin and statistics of low frequency clones at single-cell resolution in a well-controlled environment, we designed a microfluidic chemostat (the "population machine") that mimics the growth at the expanding front of a colony. In combination with a newly engineered color-switching *S. cerevisiae* strain, we track clonal lineages for ten generations. Visualization of the clones shows that small clones stem from mutations that occur behind the population's front. The mutant cells are then pushed towards the bulk of the population by the proliferating cells in front and eventually fall out of the growth layer and stop dividing, limiting the maximum size a clone can reach.

Cell-based simulations show that mechanical cell-cell forces are sufficient to explain the observed low frequency spectrum, and that the spectrum's behavior is robust to cell-level details such as cell shape and mode of division.

We further develop a theoretical model that captures the essential population genetic process that shapes the low frequency spectrum, extends our results to a broad range of cellular populations,and provides predictions beyond evolutionary neutral populations.

Finally, we discuss a useful sampling strategy to sequence spatially structured populations such as tumors. We show that the spatial position where one takes samples defines which regime of the site frequency spectrum one can capture. Our results suggest that the whole site frequency spectrum can be reconstructed by combining various sampling methods and rescaling.

3.3 Results

Fluctuation test in bacterial colonies

To assess the clone size distribution of small clones ($< 10^4$ cells) in *E. coli* colonies grown from single cells to $\approx 10^9$ cells, we adapted the Luria-Delbrück fluctuation test [157], routinely used to determine spontaneous rates of resistant mutations in well-mixed populations [158–162], to structured populations like colonies (Fig. 3.1). Colonies were grown on rich non-selective media, scooped up completely after two days of growth, resuspended, and then plated on selective plates containing nalidixic acid (see Methods). After overnight growth, the selective plates were imaged and the number of resistant colony forming units (CFUs) were counted (Methods).
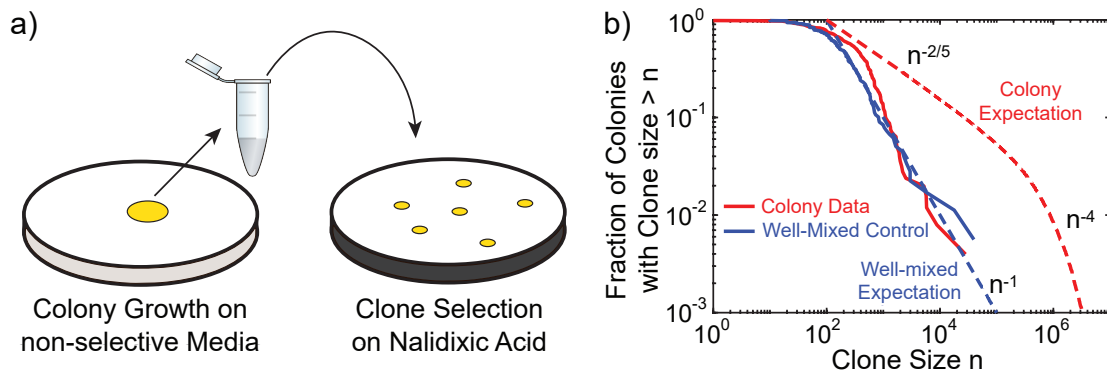
Figure 3.1: Fluctuation test in bacterial colonies reveals a distinct clone size distribution at low frequencies. (a) Fluctuation test on 234 *E. coli* colonies that were grown for two days, completely harvested and then plated on nalidixic acid. The size of clones corresponding to resistant mutations was determined by counting the number of CFUs on selective plates. (b) Fraction of the sampled colonies carrying at least *n* resistant mutants (red solid line) in comparison with the well-mixed control (blue solid lines). The blue dashed line corresponds to the classic Luria-Delbrück distribution for well-mixed populations (n^{-1}) [163], while the red dashed line corresponds to large clones found in colonies ($n^{-2/5}$ and n^{-4} regimes, corresponding to so-called "bubble" and "sector" patterns that were previously characterized [123].)

The resulting distribution exhibits a decay that resembles the classic Luria-Delbrück distribution typical of well-mixed populations (dashed blue line in Fig. 3.1), in contrast to the distribution of large mutant clones ($> 10^5$ cells) previously observed in similar colonies of the same strain via population sequencing (dashed red line) [123]. Indeed, comparison of the clone size distribution pre-factors between colonies and well-mixed populations from sequencing data had previously hinted to the necessary presence of a different distribution regime at very low frequencies [123]. In the following, we investigate the physical origin of these low-frequency clones and characterize their statistics.

Clone tracking experiments on microfluidics
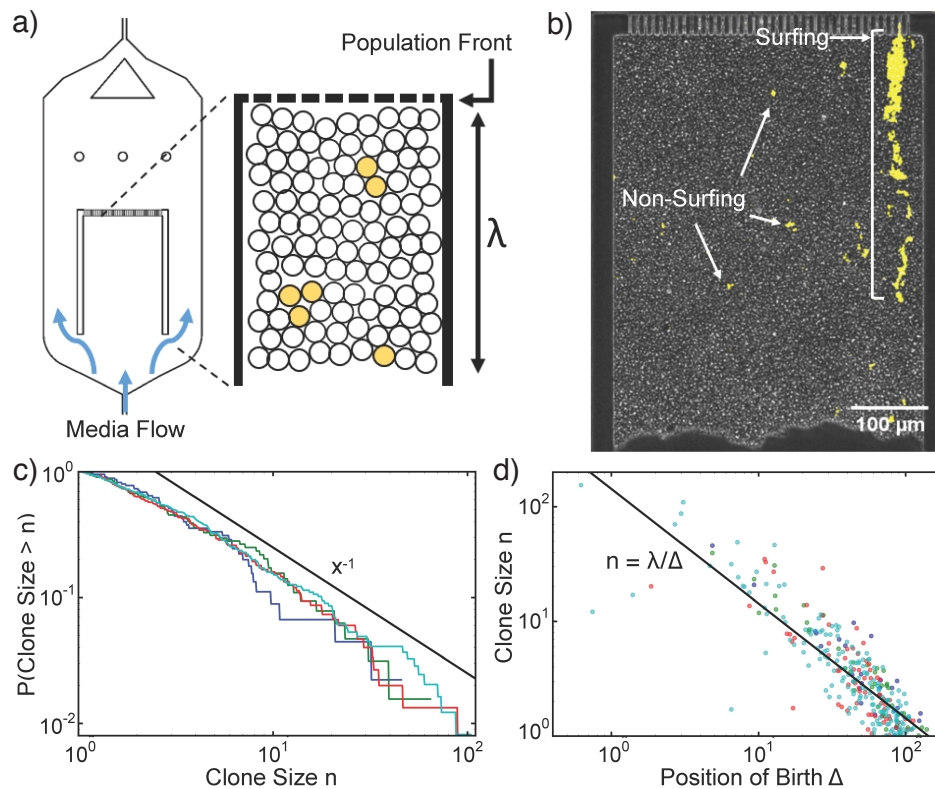
Figure 3.2: (a-d) Our microfluidic incubator enables the tracking of front dynamics over several generations. (a,b) Schematic and snapshot of microfluidic experiments. Cellular growth within the chamber models the co-moving frame of the growth layer in an expanding colony. Nutrients are supplied from both the top and bottom of the chamber by diffusion so that all cells grow at the uniform rate (Fig. 3.8). Cells out of the growth layer are flushed away by continuous media flow. (c) Proportion of color-switched cells whose final clone size is greater than n, where area is used as a proxy for clone size. The different lines indicate experimental replicas with respectively 45 (blue), 64 (green), 150 (red), 245 (cyan) mutant clones. (d) Relationship between final clone size and distance from the front at which such clone arose. Colors are as in panel (c). The black line corresponds to λ/Δ, where λ is the size of the chamber and Δ is the distance from the front.

Because in colonies cell replication is primarily limited to the region near the expanding front, called the "growth layer" [141, 164], most genetic mutations likely occur in this region. In order to visualize the emergence and dynamics of clones over several generations in a well-controlled environment, we designed an *in vitro* growth layer using a microfluidic chamber inoculated with a newly engineered color-switching budding yeast strain (Fig. 3.2a, b and Methods). In the chamber, whose design is inspired by previous studies [69, 83, 165–167], all cells grow at the same rate

(Fig. 3.8) and are continuously pushed out as the cells in front proliferate, mimicking the mechanical interactions between cells at the growing edge of a colony in its co-moving frame. By pinning the position of the population front, the device enables tracking the growth layer at single-cell resolution for up to 4 days (Fig. 3.2a, b and Methods).

To quantify the dynamics of clones stemming from a single mutational event, we conducted lineage tracking experiments (Methods and Fig. 3.7). Since the switch can occur only at cell division, is inheritable and does not measurably change the growth rate (Fig. 3.9), it effectively behaves like a neutral mutation, whose position and growth can be visually tracked with fluorescent microscopy.

During the course of the experiment, we observed both surfing clones, which are born at the very front, as well as non-surfing clones, which are born behind the front (Fig. 3.2b). Surfing events, which have been previously investigated [123], occur rarely and generate very large clones (10^2-10^3 cells each) by letting clones stay at the front for some time. By contrast, non-surfing clones cannot reach sizes larger than 100 cells and exhibit completely distinct dynamics. Using clone area as a proxy for size, we obtained the clone size distribution by tracking non-surfing clones for 19-50 hours. The resulting distribution (Fig. 3.2d) exhibits a power-law decay in agreement with the fluctuation test experiments (Fig. 3.1b).

The time resolution of this experiment enables us to go beyond the clones' ensemble behavior, and to track the dynamics the individual clones. Remarkably, we find that clone size is anti-proportional to the birth position of the first mutant (Fig. 3.2c). This straightforward relationship, despite the complexities of real cellular populations such as cell death, aging of mothers, and feedback of mechanical pressures on growth rate, suggests that a simple physical process may underlie low-frequency clones.

Mechanical simulations

To gain an intuition into whether the physical growth process alone is sufficient to generate the clone size behavior observed in Fig. 3.2, we employed 2D mechanical simulations where individually-modeled cells proliferate and repel each other upon contact (see Methods)[41, 168]. We introduced an explicit growth layer of finite depth λ within which cells of width σ grow exponentially at a uniform rate (Fig. 3.3a). Beyond the growth layer, cells are considered to be in the *bulk* and stop growing. We represented proliferation via budding to mimic our microfluidic budding yeast experiments (Fig. 3.2).

The clone size distribution obtained from simulations exhibits two regimes (Fig. 3.3b): very small clones ($n \lesssim \lambda/\sigma$, Fig. 3.5) follow n^{-1} while larger clones follow a shallower power-law in quantitative agreement with the allele surfing prediction [123]. Small clones correspond to mutations originating behind the front whereas large clones correspond to mutations originating at the front. When looking at clones arising behind the front, we find that clone size decreases monotonically with the birth position of the first mutant (Fig. 3.3c).

These results (Fig. 3.2b,c) agree quantitatively with microfluidic experiments (Fig. 3.2c,d), showing that the physical process of population expansion is indeed sufficient to generate the n^{-1} low-frequency clone distribution. To further investigate whether clone sizes are dependant on

cell-level details, we altered the rules of bud site selection in budding cells and also performed simulations of elongated cells (Fig. 3.11). In both cases, low frequency clones decay as n^{-1}, suggesting that this underlying phenomena may be described by a simple continuum mathematical model.

Crowding model of non-surfing clones

o uncover the physical mechanisms underlying non-surfing clones, we developed a mathematical model that describes what we observe in the microfluidic experiments and simulations. As in the simulations, we assumed that the growth rate is uniform within a distance λ of the expanding front and zero otherwise. We describe clones in a reference frame that is co-moving with the expanding front, so that rather than accumulating at the edge of the colony, cells are washed out towards the colony bulk (Fig. 3.3c inset). A mutant of infinitesimal size δn_0 born at a distance Δ from the front will grow until it is pushed out of the growth layer by excluded volume effects from the cells proliferating in front. This happens when the cells in front of the clone have grown to size λ to fill the growth layer. Because growth is constant within the growth layer, the mutant will grow by the same relative amount as the layers of cells in front, reaching a final size $\delta n = \frac{\lambda}{\Delta} \delta n_0$. By extending this infinitesimal relation to mutant clones with $n_0 = 1$ cell at the onset of mutation, we have the prediction (see SI section 3.7 for finite-size analysis)

$$n \approx \frac{\lambda}{\Delta}, \tag{3.1}$$

in agreement with cell-based mechanical simulations (Fig. 3.3b).

Equation 3.1 translates into a prediction for the clone size distribution when combined with the probability of observing a mutation at distance Δ. If we assume that the mutation rate is proportional to the growth rate, the probability that a mutation will occur at $\Delta < \lambda$ is $P(\Delta) = \lambda^{-1}$. Then, the probability of observing a clone of size n is

$$P(n) = P(\Delta) \times |d\Delta/dn| = \lambda^{-1} \times \lambda/n^2 = n^{-2}, \tag{3.2}$$

corresponding to a cumulative clone size distribution of $P(\text{Clone size} > n) = 1/n$.

This prediction rests on the assumptions that clone size (n) is infinitesimal compared to the growth layer depth (λ/σ) and that cellular growth rate is uniform within the growth layer. We show in SI section 3.7 that Eq. 1 is robust for finite clones up to $n = \lambda/\sigma$, corresponding to mutants born one cell behind the front, which is verified by both microfluidic experiments (Fig. 3.10) and cell-based simulations (Fig. 3.5). Additionally, in SI section 3.7 we show that our prediction also holds in the case of non-uniform growth inside the growth layer, which we verify via simulations in Fig. 3.13.

Reconstruction of clone size distribution from subsamples

By characterizing the behavior of low-frequency mutations, a complete picture of the clone size distribution in crowded expanding populations can now be assessed over the entire frequency

range. The full distribution (black line in Fig. 3.4) exhibits three distinct regimes (grey shades in
Fig. 3.4): two regimes for surfing clones that were previously characterized [123] and one regime
for non-surfing clones at low frequencies characterized in this paper. Using random population
sequencing, one can capture the complete distribution only by sequencing unrealistically deeply
(over 10^5X coverage). With a typical coverage (10-100X), population sequencing is likely able
to assess only the high frequency regimes [123] (red line in Fig. 3.4a), and miss the non-surfing
bubble behavior that accounts for most of the genetic diversity. However, other sampling strategies
can be chosen to take advantage of the spatial proximity of cells that are closely related, a practice
that is becoming increasingly frequent in cancer research [155, 156, 169–173]. We find that sam-
pling all cells in a small contiguous region of the colony is capable of detecting non-surfing clones
(magenta line in Fig. 3.4a) or the transition between non-surfing and surfing clones (cyan line in
Fig. 3.4a). The data from these contiguous regions can be appropriately rescaled (Fig. 3.4b, see
Methods for rescaling details) in order to recover the complete behavior of the clone size distribu-
tion. The local spatial distribution of mutations can therefore be used to identify non-homogeneous
growth in the population by sequencing well-chosen sub-samples.

3.4 Discussion

A single resistant cell can seed an entirely new resistant population following an antimicrobial
attack. To predict the chances of success of a drug therapy, it is therefore crucial to assess not just
the high frequency mutations, but also the rare ones present in small clones after the incubation
period. In well-mixed populations, the probability that a mutation carried by at least a frequency
n is $1/n$ across the entire frequency range. Allele surfing, a hallmark of spatial growth, has been
shown to give rise to a different probability distribution characterized by an excess of mutational
jackpot events [123]. Here, we have shown that, while allele surfing can explain the behavior of
large clones, it fails to describe the majority of mutations which reach much lower frequencies.

Crowded growth in dense populations leads to clones whose final size is determined not by
when, but *where* a mutation first arose relative to the expanding front. Large surfing clones, which
are well described by the surface growth properties of the population, arise at the very front of
the expanding edge [164]. However, most mutations occur behind the front, are pushed into the
population bulk by proliferating cells near the front, and reach only small final clone sizes. This
process leads to a reproducible relationship between final clone size and initial position of the first
mutant cell, generating a clone size distribution different from that of surfing clones.

Because clone size is only determined by the relative position to the front, our argument to de-
rive the full distribution is not limited to two-dimensional colonies expanding at the outer edge, but
can be applied to a wider class of populations. Theoretical analysis predicts that these results hold
in any system where (i) growth rate varies only along the direction of expansion, (ii) a reference
frame exists where the growth profile is constant over time, and (iii) the mutation rate per genera-
tion is proportional to the growth rate (see SI). Under these conditions, the clone size distribution
describing small clones decays like n^{-1} up to a critical size that depends only on the growth layer
depth but is independent of the number of dimensions (circular colonies vs. solid tumors, see SI),

origin of growth (outer vs. inner growth, see SI) or mode of proliferation (budding vs. symmetric division, see SI), demonstrating the robustness of the distribution.

Our model allows to extend the theoretical predictions to more complex evolutionary scenarios. For instance, we predict deviations from the n^{-1} power law in the cases where mutations confer selective effects (see SI section 4, simulation confirmation in Fig. 3.12) and where mutation rate and net growth rate are not proportional as may be the case during necrosis (see SI section 4).

As the population expands, the majority of mutations are left behind in the bulk, forming a reservoir of genetic diversity in the population. In a typical microbial colony with a growth layer of approximately 100 cells, these mutations would account for more than 99% of the genetic diversity. Analogously, in a solid tumor, they would be responsible for the vast majority of the intra-tumor heterogeneity, while being largely undetectable by population sequencing. As this class of mutations is the most abundant, it is likely to harbor those rare mutations that can confer resistance. Upon environmental changes that kill the surrounding wild-type, these mutants can be spatially released and thus rescue the population from extinction [123, 174]. It is therefore crucial to develop methodologies that enable their detection.

In well-mixed populations, the detection power is limited by the sequencing coverage one can afford. Still, because the clone size distribution is characterized by a single process across the full range of frequencies, it is possible to estimate mutation rates and selection effects using a reasonable depth of sequencing. Here we have shown that this procedure cannot be applied to crowded populations growing in space, since the shape of the clone size distribution is controlled by very different processes at low and high frequencies. A way around this problem consists in exploiting the spatial arrangement of the population. Neighboring cells are likely to be more closely related than cells farther apart, therefore concentrating sampling power to one or few locations in the population would allow to reach deeper into the low-frequency regime and measure important population genetic parameters like the mutation rate.

In the context of cancer, where there are active debates on how to distinguish selection from neutral evolution [175, 176], our findings highlight the additional challenge of distinguishing selection effects from non-uniform growth that is exclusively driven by spatial constraints. Recent work has recognized similar effects in experiments and simulations, proposing phenomenological models of the tumorogenic evolutionary process [128, 135, 156, 177]. Here we offer a microscopic, physical model of evolutionary dynamics that is consistent with the patterns of genetic diversity in solid tumors (n^{-1} distribution in [128, 156]) and which is flexible enough to provide insight into the effects that different evolutionary and demographic processes have on the statistics of rare mutants. By taking advantage of the spatial proximity of closely-related cells, this model offers rational sampling strategies for probing clone size distributions that can be useful for characterizing intra-tumor heterogeneity in cancer research [169–173]. These results can better characterize the growth dynamics of the tumor, which can be used to more precisely identify signatures of selection.

3.5 Methods

Fluctuation test in *E. coli*

The mutator strain *mutT* of the bacterium *E. coli* was used for the fluctuation test experiment on nalidixic acid. The spontaneous mutation rate in this strain was estimated to be approximately $2 \cdot 10^{-7}$ per generation from the fluctuation test in the well-mixed control, which is consistent with previously reported values [178]. Colonies starting from single cells were grown on plates with LB and 2 % agar at 37 °C for 30 hours up to a population size between 10^8 and $5 \cdot 10^8$ cells. Each of the 234 colonies was completely scooped from the plate with a pipette tip and resuspended in PBS. A 100X dilution of the resuspension was stored in the fridge for further analysis, while the rest was plated on selective plates containing LB, 2 % agar and 30 µg/mL of nalidixic acid for CFU count. The selective plates were incubated overnight at 37 °C and imaged the following day. CFU count was determined semi-manually with a built-in ImageJ function (see below). If selective plates exhibited more than 400 CFUs, the set-aside 100X dilution was itself plated on nalidixic acid, incubated overnight, and imaged the following day to better estimate the size of large mutations. In the control experiment under well-mixed condition, populations were started from about 50 cells in 200 µL of LB and incubated on a table-top shaker overnight up to saturation. The final population size was estimated to be between 10^8 and 10^9. Each of the 178 well-mixed populations was treated similarly as described above.

Colony counting on plates

Images of colonies on plates were thresholded and binarized using ImageJ. Thresholding was done manually for each image to minimize the effect of noise, such as dust particles, smudges, or glares. Colonies near the rim of the plates were excluded to avoid an edge effect. Colony counting was done automatically with the Analyze particles function of ImageJ. The final clone size of the well-mixed populations control was rescaled by 10 to take into account the different final population size and to better visualize the comparison with the data from colonies.

Mechanical simulations

Cells are modeled as 2D rigidly-attached disks of width σ that proliferate via budding. Upon division, cells divide in polarly, with newly-formed buds retaining the orientation of their mothers. Cells interact with each other upon contact via purely repulsive elastic forces and move via over-damped Stokesian dynamics [41]. To mimic diffusion of nutrients into the population from the exterior, we allow only cells within a distance λ from the front to actively grow while the rest of the population remains in stationary phase. In order to simulate a flat geometry, we impose periodic boundary conditions in the horizontal direction so that the populations expands outward only in the vertical direction. To calculate the frequency of neutral mutations, we periodically label $40,000$ newly-born cells and track their descendants.

Fabrication of microfluidics

The microfluidics was fabricated by soft lithography [100, 101]. The master mold was made by spin-coating (CEE 100 spin coater, Brewer Science) a 10 μm - thick layer of negative photoresist (SU8-2010, MicroChem) on a silicon wafer (WaferNet). The photoresist was patterned by photolithography on a mask aligner (Hybralign 200, OAI) through a chrome photomask (Compugraphics). The thickness of the pattern was measured by a stylus meter (Dektak3030, Bruker). Polydimethylsiloxane (PDMS, Sylgard 184, Dow Corning) was mixed with the crosslinker in 10-to-1 ratio and poured on the mold. After being cured at 60 °C overnight, the PDMS was peeled off from the mold and punched holes in for inlets and outlets. The chip was bonded to a glass coverslip after O_2 plasma treatment by a reactive ion etcher (Plasma Equipment Technical Services). Prior to cell culture, 0.1 % bovine serum albumin (Sigma-Aldrich) was loaded into the device to reduce the interaction between cells and the substrate.

Yeast Strain

The microfluidics experiments were conducted with the *S. cerevisiae* strain yJK10, derived from strain yDM117 (courtesy of Jasper Rine, University of California, Berkeley). yJK10 employs a Cre-loxP recombination system to switch stochastically from a red (yEmRFP) to a green (yEGFP) fluorescent state, as previously published [123, 179]. Using an estradiol-inducible Cre construct allowed us to optimize the average switching rate for our experiments[180]. For all experiments, we used a concentration of 1.6 nM β-estradiol corresponding to a switching rate of $7.1 \pm 4.8 \times 10^{-4}$ per cell per generation (estimated from the number of observed switching during the microfluidics experiments). In principle, the relative fitness between switched and unswitched cells can be set via the differing cycloheximide susceptibility of both states. However, while we did not perform any variation of relative fitness in this study, we chose to use yJK10 to maximize comparability of our results to ongoing and future investigations involving this strain. Under our experimental condition, the relative fitness between the two states ($s = 0.022 \pm 0.040$) is sufficiently small to be neglected (Fig. 3.9). See the SI section 4 for the effect of non-zero s on the power-law exponent of the distribution of clone size.

Clone tracking in microfluidics

The microfluidic growth chamber was designed as a population version of the mother machine [69]. A suspension of yJK10 cells in an exponential phase was injected into the device with YPD culture medium. After overnight culture, cells grew and filled up the growth chamber. At this point, 1.6 nM β-estradiol was added to the culture medium to induce color switching (the switching rate was about 10^{-3} per cell division). Subsequent growth was imaged using time-lapse microscopy on an inverted microscope (IX81, Olympus) with a 10X objective every 10 minutes for 2-4 days. The taken GFP images (color of switched cells) were binarized by Otsu's method [181], and the dynamics of the clones were manually tracked on Matlab (Mathworks) and ImageJ (NIH). Throughout the experiment, the temperature was controlled at 30 °C by a microscope incubator (H201-T, Oko-

lab), and the flow rate of the medium was regulated by syringe pumps (neMESYS, CETONI) at 15 μL/h. The growth rate of cells was uniform across the chamber under our experimental condition (Fig. 3.8) [182].

3.6 Acknowledgements

3.7 Supplementary information

Finite size effects in minimal model of clone size distribution

Here, using a 1D mathematical model of growth layer expansion, we derive a relationship between birth position (Δ) and clone size (n) without relying on an assumption that clone sizes are infinitesimal.

We first consider an infinitesimally small mutant of width $d\sigma_0$ born at a distance Δ from the front. This mutant will grow until it is pushed out of the growth layer by the cells proliferating in front of it, which occurs when the thickness Δ of cells in front has reached width λ filling the growth layer. Because growth is constant within the growth layer, the infinitesimal mutant will grow by the same relative amount as the thickness of cells in front, reaching a final width $d\sigma_f = \frac{\lambda}{\Delta} d\sigma_0$.

Next, we consider a mutant with an initial finite width σ_0 centered at a distance Δ from the front by subdividing it into many infinitesimal mutant segments over the range $[\Delta - \sigma_0/2, \Delta + \sigma_0/2]$. Since each infinitesimal segment $d\Delta'$ satisfies the relationship above, the final size of the mutant clone will be

$$\sigma_f = \int_{\Delta-\sigma_0/2}^{\Delta+\sigma_0/2} \frac{\lambda}{\Delta'} d\Delta' = \lambda \log\left(\frac{\Delta + \sigma_0/2}{\Delta - \sigma_0/2}\right). \tag{3.3}$$

Assuming that the initial width σ_0 corresponds to one cell width, we refer to $n = \sigma_f/\sigma_0$ as the final clonal size and express λ

$$n = \lambda \log\left(\frac{\Delta + \sigma_0/2}{\Delta - \sigma_0/2}\right). \tag{3.4}$$

In the limit where $\Delta \gg 1/2$ (or equivalently $n \ll \lambda$)

$$n \approx \frac{\lambda}{\Delta/\sigma_0}, \tag{3.5}$$

This relationship between position at birth and final clone size is consistent with what we predict in the main text for infinitesimal clones (Eq. 3.1) and find in cell-based simulations (Fig. 3.3b).

This approximation underestimates the final clone size, with the largest errors corresponding to mutations that occur closest to the front ($\Delta \ll \lambda$). However, the approximation works very well even for the largest possibly non-surfing clones that originate at $\Delta = \sigma_0$, corresponding to a relative error of $|(n_{\text{exact}} - n_{\text{approx}})/n_{\text{exact}}| = 0.1$. Clones born closer to the front ($\Delta < \sigma_0$) tend to surf (Fig. 3.3c), leading to a qualitative change in the clone size distribution that is highly dependent on the granular nature of the cell colony.

The relationship between position at birth and final clone size, which holds for each clone individually, translates into a prediction for the global clone size distribution when combined with the probability of observing a mutation at distance Δ. We assume that the mutation rate is proportional to the growth rate (no death), meaning that mutations occur with a certain probability only when a new cell is born. Since growth is constant within the growth layer, the probability that a mutation will occur at Δ (for $0 < \Delta < \lambda$) is $P(\Delta) = \lambda^{-1}$. By inverting Eq. 3.4 in order to calculate $d\Delta/dn$

$$\Delta = \frac{1}{2}\frac{e^{n/\lambda} + 1}{e^{n/\lambda} - 1}, \tag{3.6}$$

we can obtain the probability of observing a clone of size n

$$P(n) = P(\Delta)\left|\frac{d\Delta}{dn}\right| = \frac{e^{n/\lambda}}{\lambda^2(e^{n/\lambda} - 1)^2}, \tag{3.7}$$

If $n \ll \lambda/\sigma_0$, we find the approximate relation we had before $P(n) \approx n^{-2}$ (and cumulative distribution $P(n > \text{Clone size}) \approx n^{-1}$).

Extension to non-uniform growth layer

We built an ODE model able to explain the form of the clone size distribution we observe for an arbitrary one-dimensional growth profile $k(z)$. At time $t = 0$, a mutant cell is born a distance Δ behind the front. We assume that the growth rate $k(z)$ depends only on the z position of the cell measured as distance from the front in units of cell widths and that $k(z)$ is constant over the length of one cell. The clone size n will evolve in a position

$$\dot{n} = \int_{z(t)}^{z(t)+n} k(z')dz' \approx k(z(t))n$$

where $z(t)$ is mutant clone's position at time t. We have taken the limit that the characteristic clone size is smaller than the lengthscale on which k decays. Formally, the final size of the clone will be:

$$n_\infty = n_0 \exp\left[\int_0^\infty k(z(t))dt\right]$$

where n_0 is the initial size of the clone (in most cases 1) The element's position, z, will move away from the front with velocity:

$$\dot{z} = \int_0^z k(z')dz'$$

if we choose a frame of reference in which the front is 'pinned' at $z = 0$ while the bubble is pushed back along the nutrient profile. A key assumption here is that the growth profile is stable in relation to the front. Now, we can write the asymptotic clone size as:

$$n_\infty = n_0 \exp \left[\int_\Delta^\infty \frac{k(z)}{\dot{z}} dz \right] = n_0 \exp \left[\int_\Delta^\infty \frac{k(z)}{\int_0^z k(z') dz'} dz \right]$$

Note that in order for the asymptotic area to be well-defined, the integral over z must be finite. We make the change of variables:

$$\kappa_z \equiv \int_0^z k(z') dz'$$
$$d\kappa_z = k(z) dz$$

Therefore:

$$n = n_0 \frac{\kappa_\infty}{\kappa_\Delta}$$

where we have dropped the subscript on n. We see that κ_∞ must be a finite constant to have a finite asymptotic area, so this further constrains our choice of $k(z)$.

The clone size distribution $P(n)$ can be written as

$$P(n) = \left| \frac{da}{d\Delta} \right|^{-1} P(\Delta),$$

and from the relationship above we have that

$$\left| \frac{dn}{d\Delta} \right| = n_0 \frac{\kappa_\infty}{\kappa_\Delta^2} k(\Delta)$$

If we assume that the probability of mutating is proportional to the growth rate, then $P(\Delta) \sim k(\Delta)$. It thus follows that

$$P(n) \sim \frac{\kappa_\Delta^2}{n_0 \kappa_\infty} \sim \frac{1}{n^2}.$$

The result holds for exponential growth profiles, power law profile with small and large z cutoffs, and Monod type profiles of the form $\frac{e^{-z}}{1+e^{-z}}$. We explicitly test this prediction for mechanical cell-based simulations with exponential profiles in Fig. 3.13.

Another interesting aspect of this analysis is that the final bubble area depends on its position at birth through the term κ_Δ. We see that κ_Δ is a measure of the total amount of available biomass between the bubble's birth position and the front. In other words, the bubble size is dictated by global properties of the nutrient profile.

Selection: single effect size

If the mutations are not neutral, the mutant population will grow at a different rate compared to the WT. We assume that this difference is given by a multiplicative constant, so that if the WT grows according to $k(z)$, the mutant grows according to $(1+s)k(z)$ where $s > -1$ is the "fitness difference" between the two strains.

Using the same analytical derivation as in the previous section, we find that

$$n = n_0 \left(\frac{\kappa_\infty}{\kappa_\Delta} \right)^{1+s}.$$

Note that for neutral mutations ($s = 0$) we recover the old result. We now get for the probability distribution (conditioned on s):

$$P(n|s) \sim n^{-\frac{2+s}{1+s}}$$

corresponding to cumulative distribution $P(\text{Clone size} > n) \sim n^{-1/(1+s)}$. See Fig. 3.12 for verification of this prediction in mechanical cell-based simulations.

This prediction follows our intuition: if $s < 0$ (deleterious mutations) the bubble distribution falls off more steeply, whereas it becomes more broad as we get to larger positive fitness effects.

Selection: distribution of fitness effects

A distribution of fitness effects will also create noticeable distortions in the clone size distribution. For small s, we have:

$$P(a|s) \sim n^{-2+s}$$

For a distribution of fitness effects $P(s)$, we have the clone size distribution:

$$P(n) = \int P(n|s)P(s)ds \sim n^{-2}\langle n^s \rangle_s$$

where $\langle n^s \rangle_s$ is related to the generating function of the distribution of fitness effects, $\langle e^{zs} \rangle_s$, evaluated at $z = \log n$.

Let's assume $s \sim \mathcal{N}(0, \sigma)$, so we have:

$$P(n) \sim n^{-2} \int n^s e^{s^2/\sigma^2} ds$$

where we have dropped any constant factors. We can complete the square and perform the integral to get:

$$P(n) \sim n^{-2} \exp\left(-\frac{\sigma^2 \log^2 n}{4} \right) \approx n^{-2} \left(1 - \frac{\sigma^2 \log^2 n}{4} \right)$$

since σ is assumed to be small.

Clone size in microfluidic lineage tracking

In microfluidic experiments, we measure the size of clones within a culture chamber at each time point and use the maximum value as a proxy of final clone size. We show here that this approximation does not affect the predicted power-law of the site frequency spectrum.

If a cell is born at distance Δ from the front with initial length σ_0, then the initial position of the leading edge of the clone is $z = \Delta + \sigma_0/2$. When the leading edge makes contact with the back of the growth layer ($z = \lambda$), the entire clone is stretched to size $\sigma_f = \sigma_0 \lambda/(\Delta + \sigma_0/2)$. Inverting this relationship gives $\Delta = \lambda/n - 1/2$, where the length scale is rescaled by σ_0. The result slightly deviates from Eq. 3.1, but $P(n) \propto d\Delta/dn \propto n^{-2}$ holds in this case as well.

Clone size distribution with non-homogeneous death rate

The clone size distribution for non-surfing clones behaves like n^{-2} when assuming that the probability $P(\Delta)$ for a mutation to appear at position Δ is proportional to the net growth rate $k(\Delta)$ in such position. However, this assumption might break under certain conditions, for instance if a non-homogeneous death rate is present. In the general case, it still holds that the probability of observing a mutant of size n is

$$P(n) = P(\Delta) \left| \frac{dn}{d\Delta} \right|^{-1}$$

and the relationship between final size n and position at birth Δ remains

$$n \propto \left[\int_0^\Delta k(z)dz \right]^{-1}$$

where $k(z)$ is the net growth rate at position z. However, further simplifications cannot be made, leading to the general expression

$$P(n) \propto \frac{P[\Delta(n)]}{n^2 k[\Delta(n)]},$$

where the notation $\Delta(n)$ highlights that Δ is a function of n. The functional form of the clone size distribution $P(n)$ will then in general depend on the specific form of $P(\Delta)$ and $k(\Delta)$.

For illustration, we report here an example in which we define the net growth rate $k(z) = \exp(-z/\lambda) = \alpha(z) - \beta(z)$, where $\alpha(z)$ represents the birth rate and is proportional to the mutation rate $P(z)$, while $\beta(z)$ is the death rate. In this case, $n = [1 - e^{-\Delta/\lambda}]^{-1}$ and

$$P(n) \propto \frac{\alpha(\Delta)}{n^2(1 - 1/n)} = \frac{\alpha(\Delta)}{n(n-1)}.$$

If $\alpha(z)$ is uniform along z and $\beta(z) = 1 - e^{-z/\lambda}$, then the clone size distribution $P(n) \propto \frac{1}{n(n-1)}$, which tends to n^{-2} for large n, but deviates from it at small n. This would correspond to the case in which replication rate is not affected by position, but death rate increases as we move deeper inside the colony, for instance because of the accumulation of toxic waste.

Inferring mutation rate from non-surfing clones distribution and localized deep sequencing

We have shown that for non-surfing clones, the probability that a mutation is larger than size n is $P(\text{Clone size} > n) = 1/n$. Indeed, by definition, a mutation has to be carried by at least $n = 1$ cells and $P(\text{Clone size} > 1) = 1$ as intuition suggests. A related quantity to $P(\text{Clone size} > n)$ that can be observed experimentally is the number of mutations $M(\text{Clone size} > x)$ that are carried by at least a frequency x of the population (Fig. 4). Because the total number of mutations in a population of final size N is approximately μN, where μ is the mutation rate per replication, it follows that $M(\text{Clone size} > x) = \mu N P(\text{Clone size} > n) = \mu N/n = \mu/x$. It is therefore possible to estimate the mutation rate μ from the prefactor of the non-surfing clone regime of $M(\text{Clone size} > x)$ (low-frequency range of the black line in Fig. 4).

If the population is too large or sequencing coverage is too low to observe the non-surfing clone regime, we find that localized bulk deep sequencing can be used (cyan line in fig. 4). In this case, the observed frequency $\hat{x}$ of a mutation represents the frequency in the sequenced sub-population $\hat{N} < N$. However, also the total number of mutations in the sub-population scales like $\mu \hat{N}$. As a result, the observed number of mutations above an observed frequency, $\hat{M}(\text{Clone size} > \hat{x}) = \frac{\mu \hat{N}}{\hat{x} \hat{N}} = \mu/\hat{x}$. Therefore, the prefactor of the power-law can again be used to estimate the mutation rate of the population, even if only part of the population is sequenced.

Rescaling of entire colony frequency spectra

In order to rescale the clone frequency distributions from sub-sampled regions, we calculate a characteristic frequency f_c and corresponding value of the cumulative distribution N_c. The frequency f_c can be thought of as the frequency that a mutation carried by a single cell in the sub-sample would have in the entire colony.

For the side sampling technique, f_c is determined the the solid angle $\theta =$(sampled width)/(colony radius) that is inscribed by the sampled region: $f_c = \theta$. For the middle sampled regions, n_c further takes into account the ratio $r =$(number of cells in fictitious inner colony with radius equal to outer extent of sampled region)/(number of cells in entire colony): $n_c = r\theta$.

N_c is then determined by aligning the smallest of value of N is the subsampled region with with predicted trend $N/N_c = n_c/f$.

Supplementary Figures
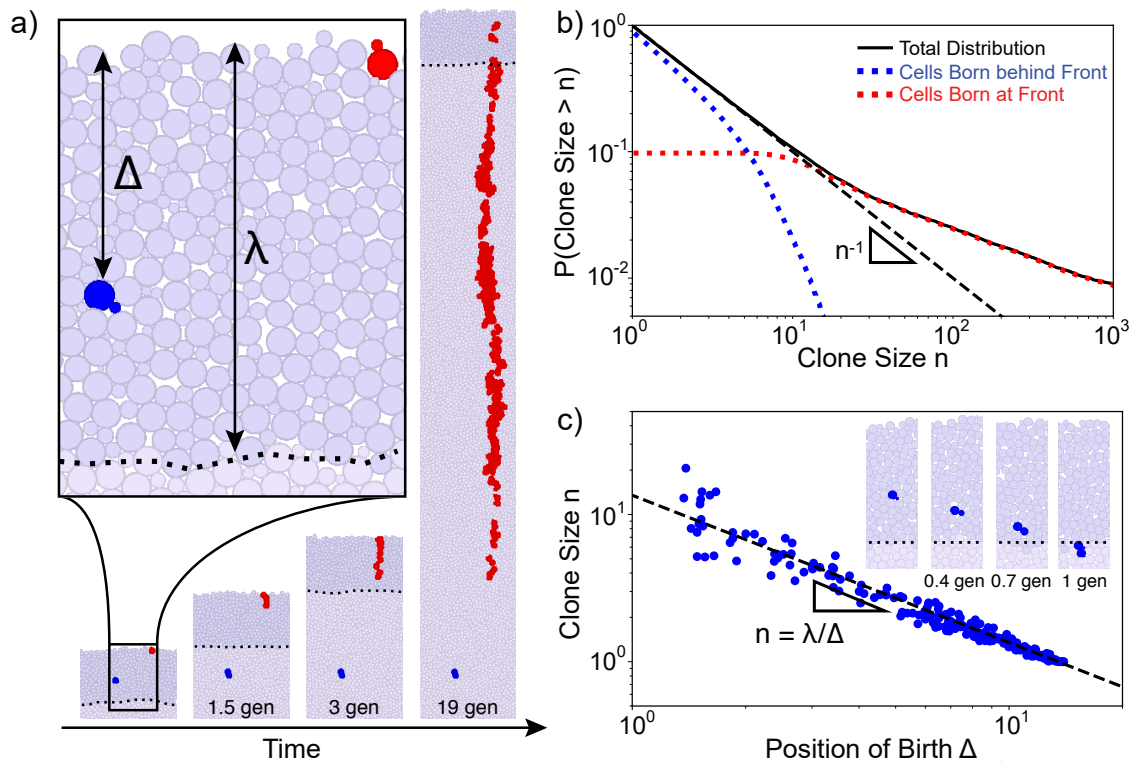
Figure 3.3: Cell-based simulations show different behaviors between surfing and non-surfing clones. (a) Illustration of the mechanical simulations. Cells lying in the growth layer, defined as the region within a distance $\Delta < \lambda$ from the front (dark purple region with dashed line showing back of growth layer), replicate exponentially. In this image, $\lambda = 14$ cell widths (about 50 μm). As growth proceeds, the front moves at a constant speed and cells behind the front are continuously pushed out of the growth layer by replicating cells in front due to excluded-volume interactions. Mutations can either occur at the very front (red cells) generating a surfing clone, or behind the front (blue cells) generating non-surfing clones that are quickly washed out of the growth layer. Clonal dynamics are shown for the first 20 generations of cellular growth. (b) The full clone distribution (solid black line) can be subdivided in the size distribution of surfing clones (red dotted line), which dominate the high-frequency tail of the distribution, and non-surfing clones (blue dotted line), that dominates the low-frequency behavior. The dashed black line shows the n^{-1} prediction. (c) Scatter-plot identifying for each clone (blue dot) the distance from the front at which the mutation first arose and the final clone size upon exiting the growth layer. Surfing clones are by definition clones that arose within 1 cell distance from the front. Non-surfing clones are found to satisfy the relationship $n = \lambda/\Delta$, rationalized in Eq. 3.1 (dashed black line). The inset shows the dynamics of the blue clone a short time (< 1 generation) after birth in the reference frame of the front. This clone is born at distance $\Delta = 7$ cells from the front and grows to a size of $n = 2$.
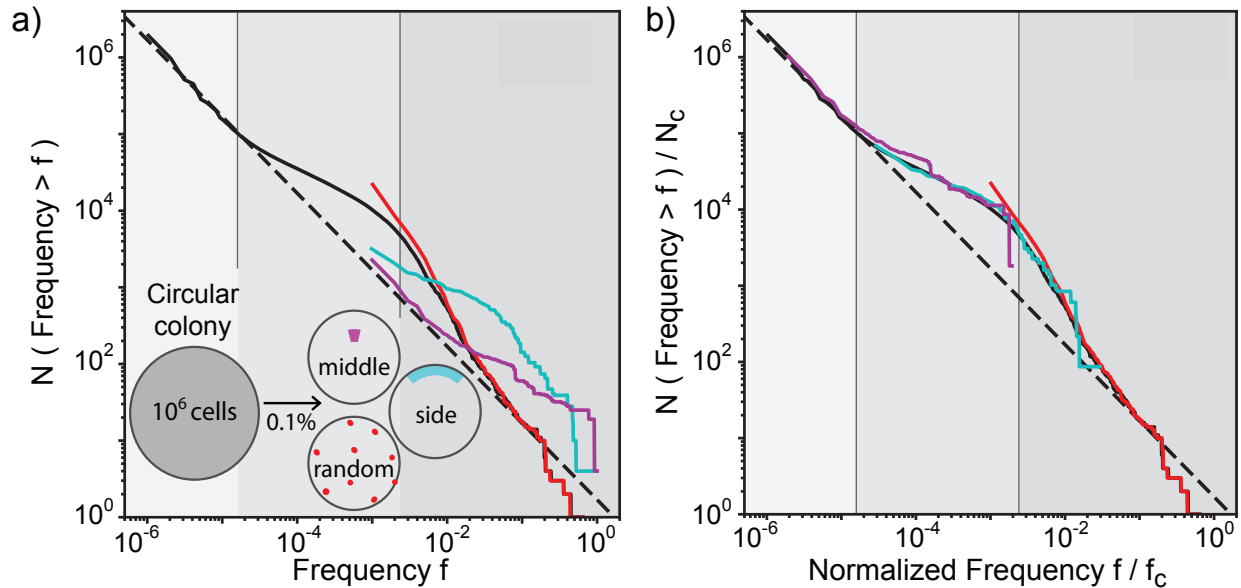
Figure 3.4: Results from multiple sampling strategies can be combined to infer mutation rate
and growth dynamic of the population. (a) Different sampling methods generate distinct clone
frequency distributions that highlight distinct properties of the growth dynamics. This in stark
contrast with well-mixed populations where the sampling scheme merely affects how well the
clone frequency distribution can be resolved. The solid black line shows the clone frequency
distribution (clone size divided by population size) of the whole simulated colony (growth layer
$\lambda/\sigma = 14$ cells) grown up to 10^6 cells. We identify three frequency f ranges in the site fre-
quency spectrum: (i) for $f < (\lambda/\sigma)/N$, the distribution is dominated by non-surfing clones; (ii)
for $(\lambda/\sigma)/N < f < 0.003$, allele surfing dominates generating bubbles and sectors as previously
described; (iii) for $f > 0.003$, we see a third behavior, generated by mutations that arise in the
first few generations, when the whole microcolony is growing exponentially ($N < \pi(\lambda\sigma)^2$). The
grayscale regions correspond to non-surfing bubbles (light gray), surfing bubbles (intermediate
gray), and sectors (darkest gray). Sampling 0.1 % of the population (equivalent to a 1000X cov-
erage in sequencing) can target non-surfing small clones and generate their corresponding dis-
tribution (middle, magenta), or high-frequency surfing clones (random, red). Sampling an outer
segment generates a shifted distribution where distinct trends can be observed. (b) These sampling
techniques can be combined to reproduce the entire clone size distribution. The rescaling used
here requires only knowledge of the total number of cells in the colony and the size/shape of the
sampled region, as are described in SI section 3.7.
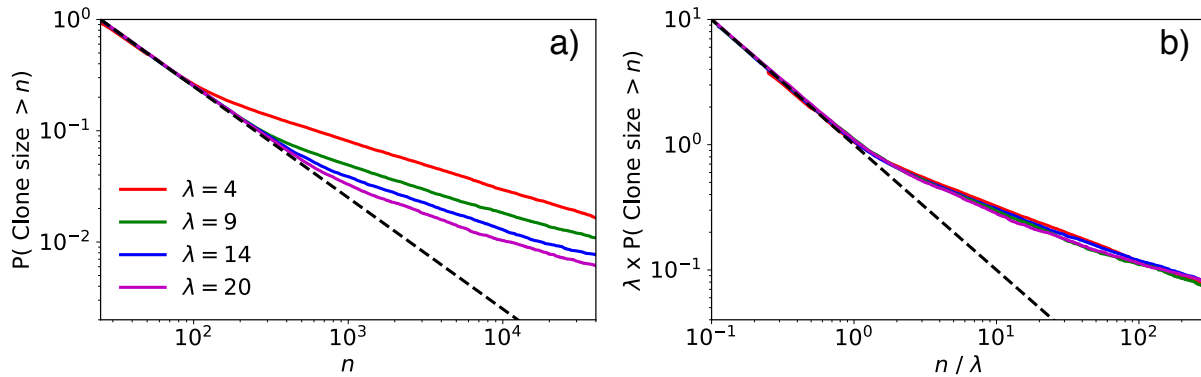
Figure 3.5: (a) Clone size distribution for a range of growth layers depths: $\lambda = 4$, $\lambda = 9$, $\lambda = 14$, and $\lambda = 20$ (units of cell widths). The dashed line shows the n^{-1} prediction. (b) Clone size distribution rescaled by λ shows that the n^{-1} regime extends over the range $n = 1$ to $n = \lambda$. For $n > \lambda$, the clone size distribution is dominated by surfing bubbles (Fig. 3.3a).
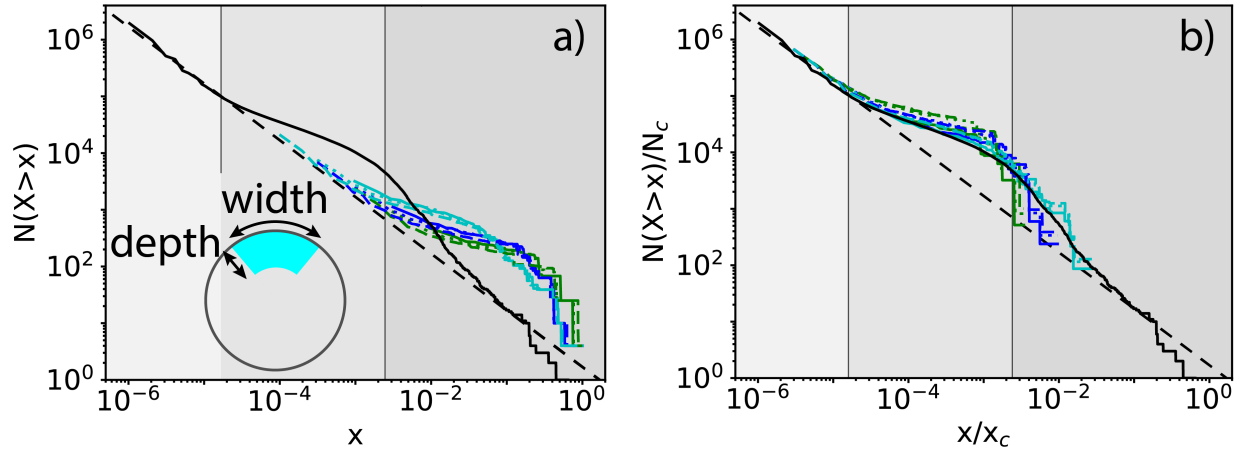
Figure 3.6: (a) Clone size distribution (black) for colony with $\lambda = 14$ cells and radius $R = 602$ cells (total number of cells in colony $= 10^6$). Colored lines show distributions obtained via sub-sampling using side technique with widths 11 cells (green), 36 cells (blue), 112 cells (cyan) and depths of 11 cells (solid line), 36 cells (dashed line), 120 cells (dotted line). Shaded regions correspond to non-surfing bubbles, surfing bubbles, and established sectors. The grayscale regions correspond to non-surfing bubbles (light gray), surfing bubbles (intermediate gray), and sectors (darkest gray). (b) Rescaled distributions, x_c and N_c are described in Section 3.7.
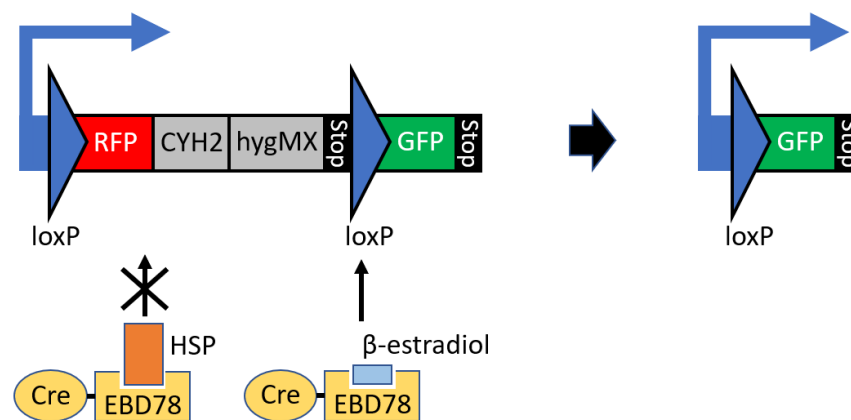
Figure 3.7: A schematic of the engineered *S. cerevisiae* strain yJK10 that stochastically switches
the color from RFP (yEmRFP) to GFP (yEGFP). The switching rate is tunable with β-estradiol,
and the fitness advantage/disadvantage of switched cells can be tuned with drugs, hygromycin B
and cycloheximide due to an additional cycloheximide resistance allele cyh2∆::cyh2r [183]. The
genotype of the strain is as follows:
*W303 MATa cyh2∆::cyh2-Q37E-cs hmlα2∆::R ho∆::prSCW11-cre-EBD78-natMX
ura3∆::prGPD-loxP-yEmRFP-tCYC1-CYH2-hygMX-loxP-yEGFP-tADH3*.
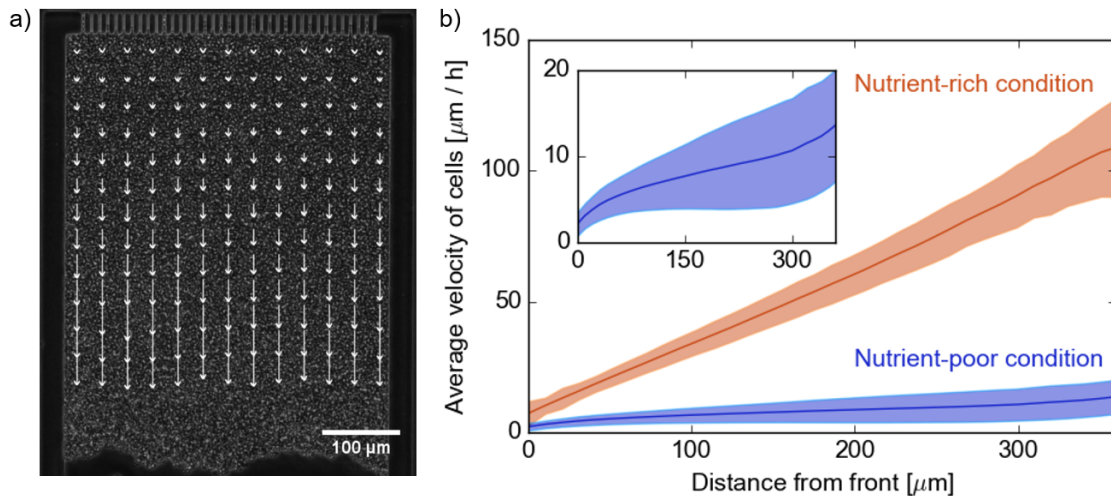
Figure 3.8: (a) A snapshot from the particle image velocimetry analysis [102, 182]. Each arrow shows the parallel component of the displacement of a 20x20 μm² region (32x32-pixel) during one time frame (10 minutes). For the sake of visibility, the length of arrows is rescaled by factor of 2, and the number of arrows is reduced from 37x37 to 13x13. (b) Under our usual experimental conditions (nutrient-rich condition, 2%-glucose YPD media), the velocity field is linear along the growth direction, showing that all cells grow at the same rate. To make sure this method would capture a drop in growth rate, we replicated this experiment under nutrient-poor condition (0.01%-glucose YPD media). As expected, the overall velocity is reduced (slower growth rate) and heterogeneous along the growth direction (see inset), showing a slow down in the middle of the chamber due to nutrient depletion. The error shows the standard deviation of the statistics across horizontal positions and over 100 (nutrient-rich) and 140 (nutrient-poor) time points.
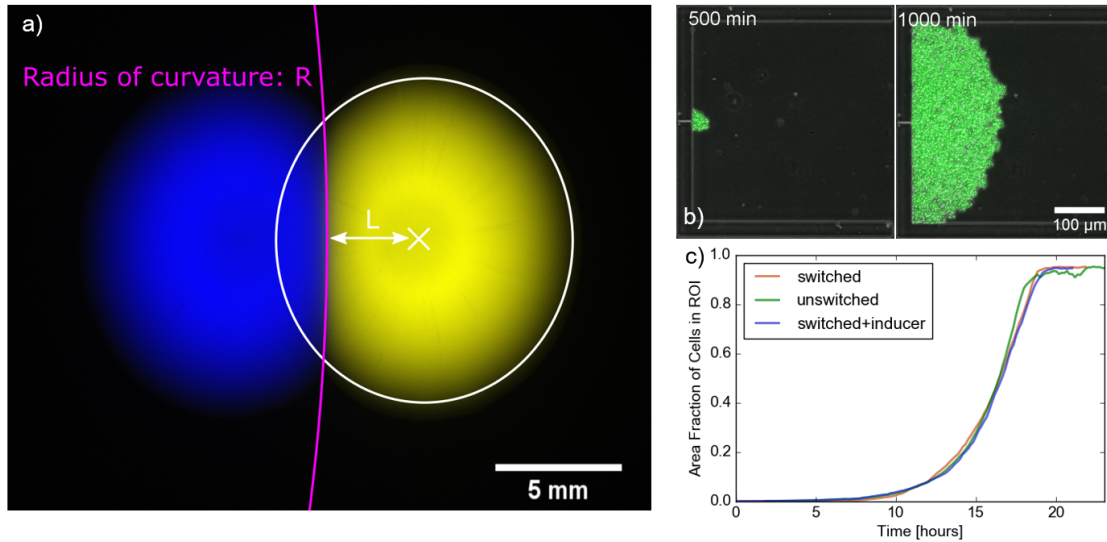
Figure 3.9: Estimation of the relative fitness between the original yJK10 strain and the color-switched yJK10 strain. (a) Colony collision experiments to estimate the fitness effect of color switching. Collisions of 12 pairs of the original yJK10 colony and the color-switched yJK10 colony were observed on YPD plates. The relative fitness between two strains was estimated at $s = 0.022 \pm 0.040$ by the formula $s = L/R$ from the equal time argument [184]. The lines on the figure are illustrations of the concept and not the actual fittings. (b) Population expansion experiments in microfluidics. 1-3 cells were initially trapped in the microfluidic chamber, and the growth of the population was observed for the original yJK10 strain (with YPD) and the color-switched yJK10 strain (with YPD and YPD + β-estradiol). (c) The exponential fitting of the growth curves gives us the estimation of the relative fitness of the color-switched strain to the original strain: $s = 0.019$ (YPD) and $s = -0.020$ (YPD + β-estradiol).
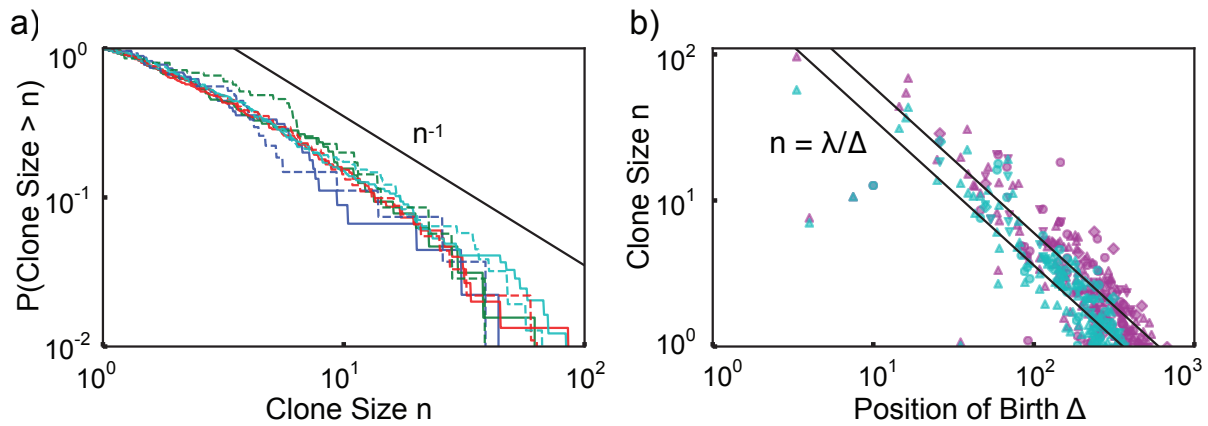
Figure 3.10: Proportion of color-switched cells whose final clone size is greater than n, where area is used as a proxy for clone size. The different lines indicate experimental replicas with respectively 45 (blue), 64 (green), 150 (red), 245 (cyan) mutant clones. The solid lines correspond to the chamber depth of $\lambda = 500$ μm as used in Fig. 2c and the dashed lines correspond to clones imaged at a distance $\lambda = 300$ μm, mimicking the clones we would expect to see in a shorter chamber. (d) Relationship between final clone size and distance from the front at which such clone arose. Purple point correspond to $\lambda = 500$ μm and cyan points correspond to $\lambda = 300$ μm. The different point types indicate experimental replicas with respectively 45 (diamonds), 64 (upside down triangles), 150 (circles), 245 (rightside up triangles) mutant clones. The black line corresponds to λ/Δ, where λ is the size of the chamber and Δ is the distance from the front.
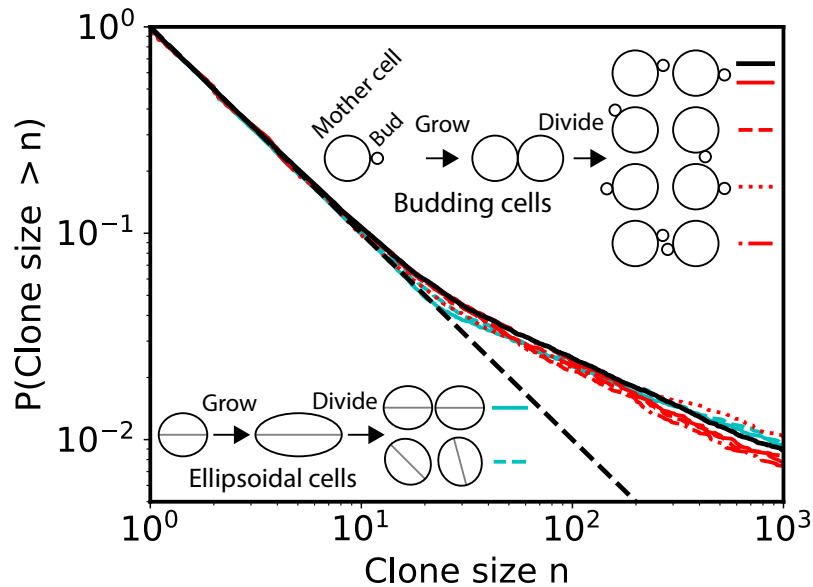
Figure 3.11: Clone size distributions for neutral mutations in mechanical simulations of ellipse-shaped and budding cells with different division rules (growth layer depth $\lambda = 14$ cell widths). The ellipse-shaped cells in these simulations have aspect ratio $= 1$ at birth and grow to aspect ratio $= 2$. These simulations use conjugate gradient energy minimization (see [185]) rather than overdamped molecular dynamics as used in the main text (Fig. 3.3). Ellipse data is shown in cyan, budding data is shown in red, and budding data from the main text (Fig. 3.3b) is shown in solid black for reference. The dashed black line shows the $1/n$ prediction. We compare four different rules for assigning the orientations after division, including the case where cells retain the orientation of their mothers (solid black/cyan/red lines), are assigned random orientations (dashed red/cyan lines), exhibit polar budding with new buds facing outward (dotted red line), and exhibit axial budding with new buds facing inward (dot-dashed red line).
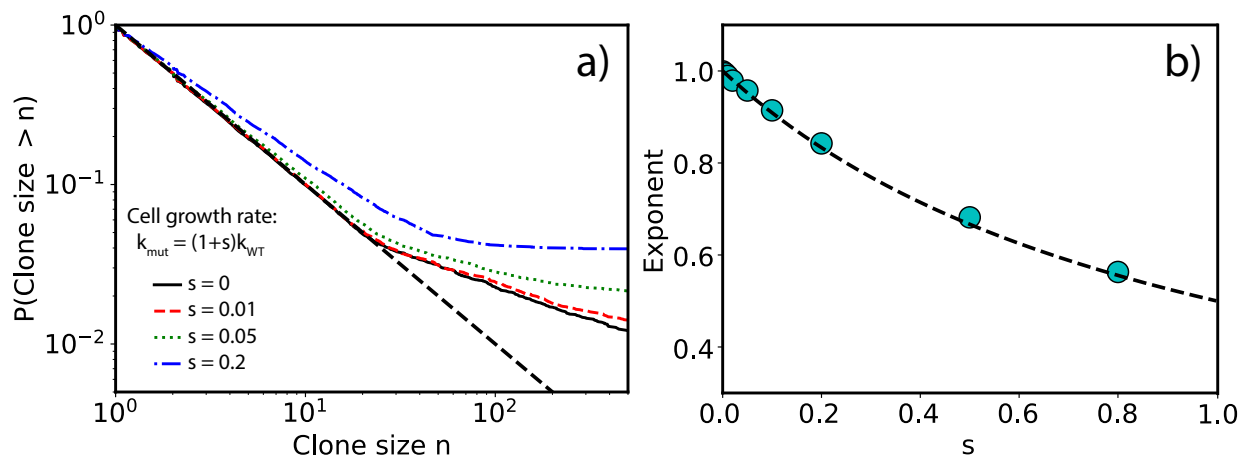
Figure 3.12: Clone size distributions for advantageous mutations in mechanical simulations with a uniform growth layer depth of $\lambda = 14$ cell widths. (a) Distributions for selective advantages ($s = k_{mut}/k_{WT} - 1$) of $s = 0$ (solid black), $s = 0.01$ (dashed red), $s = 0.05$ (dotted green), and $s = 0.2$ (dash-dotted blue). The dashed black line show the $1/n$ prediction. (b) The small-n power-law exponent (cyan points), found in the range $n < 10$, compared to the predicted value P(Clone size $>$ $n) \propto n^{-1/(1+s)}$ (dashed black line). For these simulations, we used ellipse-shaped cell simulations where cells have aspect ratio $= 1$ at birth and grow to aspect ratio $= 2$. These simulations use conjugate gradient energy minimization for population dynamics.
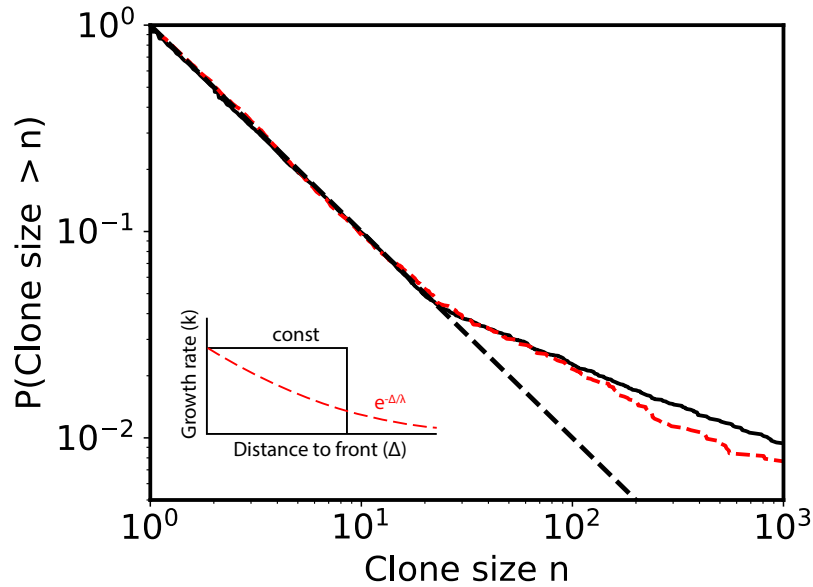
Figure 3.13: Clone size distributions for neutral mutations in mechanical simulations with a uniform growth layer (solid black line) and a growth layer profile where cellular growth rate decreases exponentially with distance to front (dashed red line). The dashed black line show the a/n prediction. Both simulations have a characteristic growth layer depth of $\lambda = 14$ cell widths. For the uniform growth layer, the growth rate $k = k_0$ for $\Delta < \lambda$ and $k = 0$ for $\Delta > \lambda$, where Δ is the distance to the colony front. For the uniform growth layer, the growth rate $k = k_0 \exp -\Delta/\lambda$ for $\Delta < \lambda_{\mathrm{cut}}$ and $k = 0$ for $\Delta > \lambda_{\mathrm{cut}}$, where we used a cut-off distance of $\lambda_{\mathrm{cut}} = 40$ cell widths. For these simulations, we used ellipse-shaped cell simulations where cells have aspect ratio $= 1$ at birth and grow to aspect ratio $= 2$. These simulations use conjugate gradient energy minimization for population dynamics.

Chapter 4

Physical structures of confinement harbor diversity

In chapter 3, we reveal the clone size distribution of jam-packed populations with a 1D continuum model. The model can be widely applied to 2D and 3D systems as long as the geometry is symmetrical, such as the situation in radial expansion. However, the model is no longer valid once the geometry gets asymmetrical or anisotropic. Especially, when the shape of the periphery is highly structured, the analysis requires special treatment. In the context of range expansion, the problem is known as the "wedge problem", where the fluctuation of domain boundaries is suppressed when the periphery has an acute concave shape [186, 187].

In this chapter, the impact of the shape of physical boundaries in a confined habitat is discussed. A hydrodynamic approximation of a cellular population, agent-based simulations, and microfluidic experiments are presented.

4.1   Introduction

Lineage dynamics in spatially structured populations are impacted by the shape of the periphery of the populations. In the case of range expansion, previous studies have shown that the front roughness is critical to the fluctuation of lineage boundaries and the site frequency spectrum [123, 141]. This is due to the mismatch between the direction of local expansion and macroscopic expansion. The local expansion is typically normal to the front shape and not always parallel to the radial direction. Consequently, a zigzag front exhibits characteristic domain fluctuations distinct from a flat front [188].

A similar analogy can be applied to confined populations. Here, the front of the range expan-

sion corresponds to the walls of the confinement. In natural confined habitats, the wall is not often flat, but has some micro-scale structures. For example, *Lactobacillus* and *Acetobacter* colonize a cardia of a fly gut, and the wall of the region has a micro-scale roughness, which may impact the population dynamics [46]. Note that, as a remarkable difference from the front shape in range expansion, the wall shape is always fixed and does not change.

In an extreme scenario, a deep concave structure at a wall can be regarded as a natural mother machine [69], where a cell can be trapped at the structure and hardly invaded by other cells. Thus, the trapped cell can stay in the population for a long time. They enjoy the spatial advantage regardless of the growth rate advantage. This suppresses natural selection and maintains genetic diversity in the cavity.

As discussed in chapter 2, microbial populations in confinement are ubiquitously found, and revealing the feature of the population dynamics is fundamental. Micro-scale structures of physical boundaries can impact the rate of evolution and turnover in confined populations. It is meaningful to investigate the effect of wall structures on population dynamics.

4.2   Continuum model simulations

To systematically study the impact of wall structure, we focus on simple pore geometries with a zigzag wall at the bottom of a pore (fig. 4.1a). We assume dense-packed populations confined in the pore, and aim to characterize the collective movement. One of the simplest models is a continuum model based on Darcy's law (see chapter 1), where r is the growth rate, μ is motility coefficient, and p is internal pressure [61–63].

$$\nabla \cdot \dot{x} = r(x), \tag{4.1}$$

$$\dot{x} = -\mu \nabla p, \tag{4.2}$$

$$\nabla^2 p = -\frac{1}{\mu} r. \tag{4.3}$$

Simulations of the model show the macroscopic behavior of the dense population given the physical boundary conditions (fig 4.1). In the model, the growth rate of cells is assumed to be uniform across the space. At the periphery, we assume a no-penetration boundary condition and slip boundary condition, meaning cells do not feel friction at the wall. At the opening, the internal pressure is assumed to be zero.

Importantly, there is a collective cellular flow at the bottom where micro-scale structures exist. The flow is directed from the convex tips to the concave tips, meaning cells at the convex tips produce offspring and push neighbors to the concave tips. These collective dynamics give a significant spatial advantage to cells at the convex tips. Cells at the convex tips are supposed to stay in the population for a long time. Also, it can be expected that the domain boundaries between lineages are fixed near the concave tips. This expectation is tested by agent-based simulations in the next section.
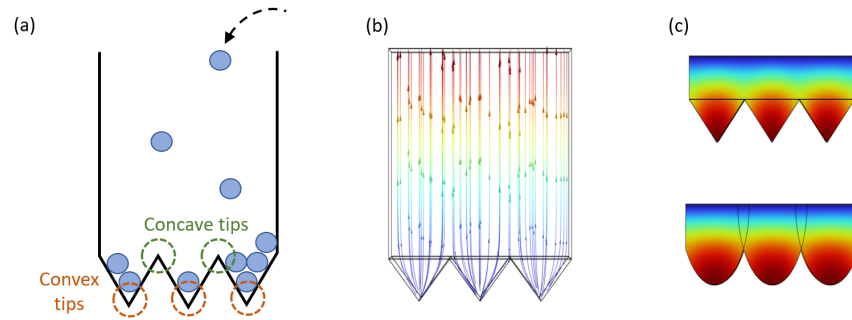
Figure 4.1: Comsol simulations of a continuum cellular growth model. (a) A schematic illustration of microbial colonization in a pore with micro-scale structures at the bottom. (b) Cellular movements in a continuum model simulated with Comsol. The arrows show the direction of movement, and the colors show the magnitude of the velocity (blue: slow and red: fast). (c) Plots of internal pressure p in different bottom geometries simulated with Comsol. The colors show the magnitude of pressure (blue: low and red: high).

Friction at the wall

Slip boundary conditions are fundamental to the collective movements near the wall; however, the condition is unusual in the context of hydrodynamics, where no-slip boundary conditions are commonly used. In the case of cellular populations, no-slip boundary conditions are not realistic because of the finite size effect of cells. On the other hand, no friction is also not very realistic, even though it is a good first-step assumption to simplify the situation. To test the degree of frictions near the wall experimentally, we do a microfluidic culture of bacteria, *Acetobacter indonesiensis*, in a straight rectangular chamber, and conduct PIV (particle image velocimetry) to measure the local velocities (fig 4.3) [182]. The cellular velocities are reduced near the wall, and the reduction is stronger when the velocity is small: it is a $\sim 50\%$ reduction around the deep part of the chamber.

4.3 Agent-based simulations

The above continuum model simulations predict the stabilization of domain boundaries between lineages. To test the prediction, we conduct agent-based simulations (fig 4.4). The simulations are originally presented in [168], and modified for this project to simulate various wall shapes. The model simulates the growth of budding cells under over-damped conditions in a 2D space. The cellular growth mechanically pushes neighbors and produces collective movements by excluding volume effects. All the cells are labeled once the population gets dense-packed, and the lineage dynamics are tracked.

The stability of domain boundaries can be captured by simulations of 2-strain dynamics (fig. 4.5). In the simulations, the chamber has four dimples, and the population dynamics show "quantized"
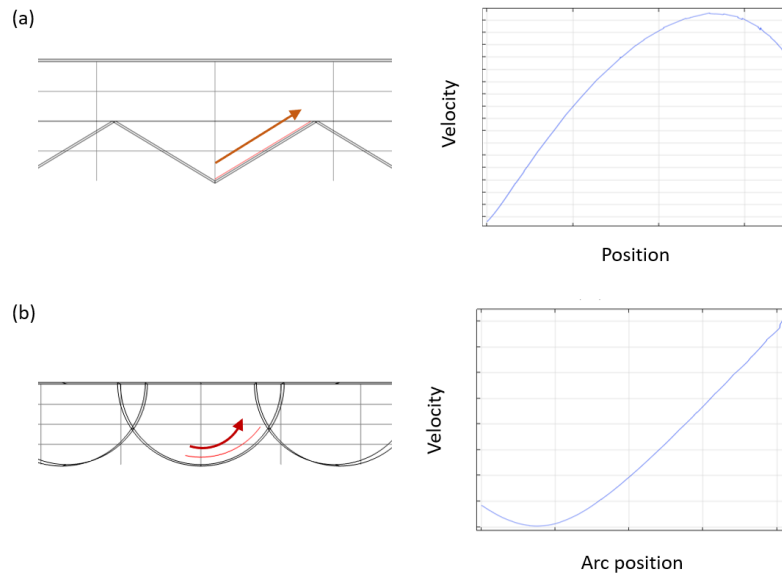
Figure 4.2: Cellular velocity along with the wall of a pore. Comsol simulations show the velocity near the wall for a zigzag geometry (a) and round geometry (b). The red line shows the region plotted in the right panel.

stable frequencies corresponding to the occupation of the dimples. Lineages are trapped within the micro-scale structures of the habitat, and they are resistant to invasion from neighboring lineages (fig. 4.5b). The results imply that spatial structures in a habitat can enhance the genetic diversity of the population.

Next, to investigate the impact of the size of the micro-scale structures, the dimple depth is systematically varied. In the simulations, all the cells in a habitat are individually labeled at a time point, and the decay of the number of existing lineages is tracked over time (fig. 4.6). As expected, the maximum number of lineages in the habitat is equal to the number of dimples when the dimples are deep. As the dimple size decreases, the number of lineages rapidly converges to 1, which is a natural consequence of genetic drift. The changes are continuous, and the decay speed monotonically correlates to the dimple size.

4.4 Microfluidic experiments

To experimentally test the theoretical predictions, microfluidic pores with micro-scale structures are fabricated, and bacteria are cultured in the chambers. The basic experimental protocol follows the method in chapter 2. Two differently-colored neutral *Acetobacter indonesiensis* strains are co-cultured in microfluidic chambers. The chamber depth is 300 μm, which is deep enough for cells to form jam-packed populations, but still sufficiently small to supply nutrients to the bottom by
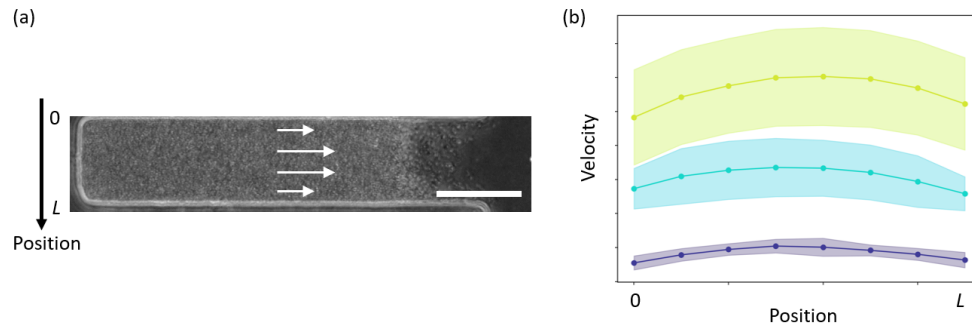
Figure 4.3: PIV analysis to show the velocity reduction near the side walls. (a) A snapshot of a microfluidic culture of bacteria. The white arrows are schematic representations of cellular flows. The white scale bar shows 50 μm. (b) PIV analysis shows the reduction of velocity near the walls due to frictions. The PIV results are averaged over time points, and the errors are shown as shaded regions. Different colors show different positions in the chamber (yellow: near the opening, and dark blue: near the bottom).
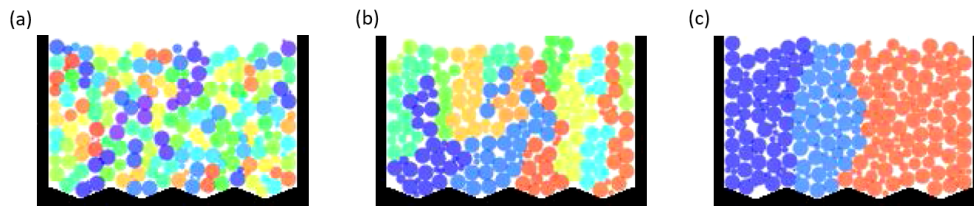
Figure 4.4: Snapshots of agent-based simulations. All the cells in a dense-packed population are labeled (a), and the lineage dynamics are tracked (b and c). Cells around the convex tips enjoy the spatial advantage and dominate the lineage dynamics in the chamber.

diffusion. The chamber has 4 dimples, whose size is about 5 μm, at the bottom wall. As control experiments, chambers with a flat-bottom wall are also tested.

Remarkably, population dynamics in chambers with micro-scale structures exhibit pinning of domain boundaries (fig. 4.7), as expected by theory. The distribution of the number of domain boundaries is measured at $t = 90$ hours after the populations get dense-packed. The flat-bottom populations exhibit the monotonically decaying distribution, consistent with the diversity loss due to genetic drift. On the other hand, the dimpled-bottom populations have the second peak in the middle, showing the tendency of pinning (note that zero domain boundary means that one strain takes over the population).
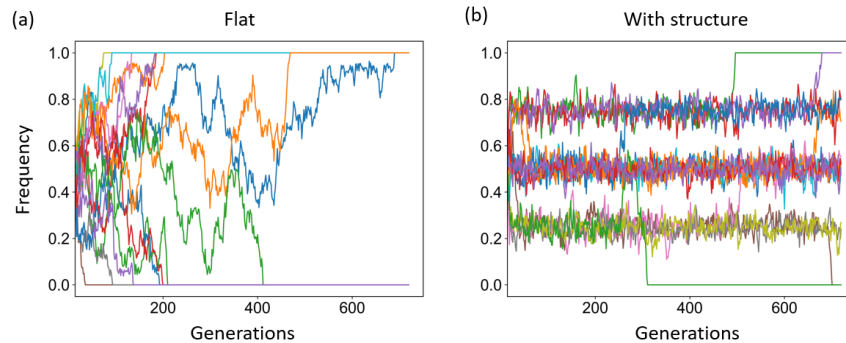
Figure 4.5: Frequency dynamics of 2-strain simulations. (a) Frequency dynamics in a chamber with a flat bottom. Population dynamics exhibit random genetic drift. (b) Frequency dynamics in a chamber with zigzag dimples. The bottom wall has four dimples, whose depth is 1 cell length. Stable frequencies are quantized to 5 states, corresponding to the dimple occupations (0 - 4 dimples are occupied).

4.5   Conclusion

In this chapter, the role of the wall shape on the dynamics of a dense-packed microbial population is investigated by a continuum model, agent-based simulations, and microfluidic experiments. The wall shape impacts the macroscopic flow of biomass by constraining the direction of cellular displacements. This results in the emergence of "spatial hot spots" where cells are spatially fixed and persist in the population.

In light of evolutionary dynamics, it is noteworthy that growth rate advantages may be less relevant when the spatial advantages due to wall shapes exist. Our results imply that structured physical boundaries weaken selective pressure and promote genetic drift. In an extreme case, spatial structures may prefer novel traits of cells such as an ability to invade a dense-packed space and attach to a "spatially-advantageous" position.

In fact, agent-based simulations reveal that even small structures, which are smaller than a single-cell size, can promote the persistence of existing lineages. Thus, micro-scale structures or the roughness of the walls can impact the genetic diversity in a confined population. Our results provide a novel insight into the importance of small physical structures in population dynamics under confinement.
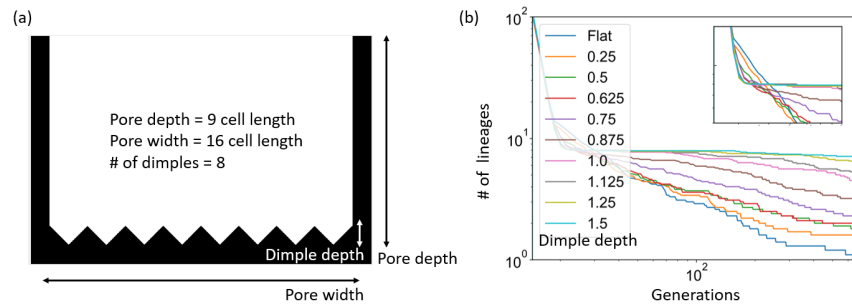
Figure 4.6: Frequency dynamics of multi-strain simulations. (a) The geometry of the chamber. All the geometrical parameters other than the dimple depth are fixed, and only the dimple depth is systematically varied from 0 (flat bottom) to 1.5 cell depth. (b) Decay of the number of lineages in the pore. 10 independent simulations are averaged for each dimple size. For the flat-bottom chamber, the number of lineages decreases to 1 due to genetic drift. On the other hand, the number of lineages stays around 8, which is the number of dimples, for the chambers with deep dimples. As the chamber depth changes, the stability of the genetic diversity is gradually decreasing. The inset shows the magnified view of the early time points of the simulations.
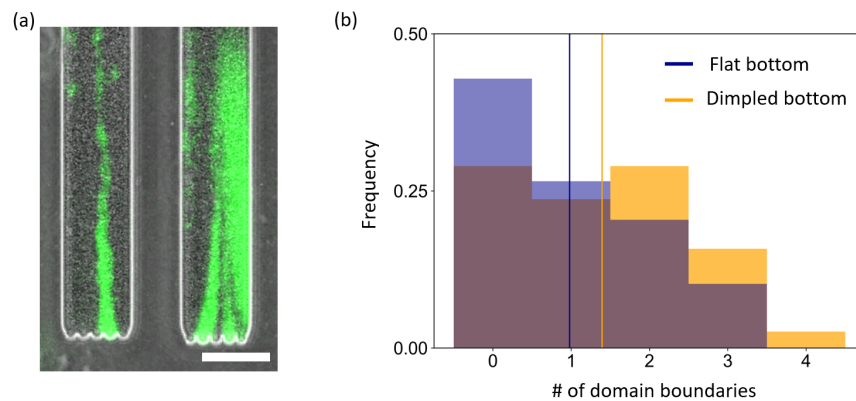
Figure 4.7: Microfluidic experiments reveal the pinning of domain boundaries at micro-scale structures. (a) A snapshot of microfluidic experiments. Differently-colored two neutral strains (green and dark) of *Acetobacter indonesiensis* are co-cultured in microfluidic chambers with 4 dimples, whose depth is about ~5 μm. The snapshot is 90 hours after the populations get dense-packed. Domain boundaries are pinned at the micro structures, and the lineage diversity is maintained. The white scale bar is 50 μm. (b) The number of domain boundaries around the bottom wall is measured in 49 and 38 populations for flat-bottom chambers and dimpled-bottom chambers, respectively. The bar graph shows the distribution of the number of domain boundaries at $t = 90$ hours after the populations get dense-packed. The vertical lines show the average number of domain boundaries for each case.

Chapter 5

Population dynamics in hydrodynamic flow

Microbial populations exhibit various density phases, as shown in chapter 2. In the previous chapters 3 and 4, characteristic dynamics of jam-packed populations are discussed. In this chapter, dilute populations in various types of flow are investigated. Especially, microfluidic methodology to design in-vitro experiments is the main topic.

This chapter consists of three parts. First, the mixing of populations by peristaltic deformation of chamber walls is discussed. Peristaltic mixing is achieved by microfluidics and, its application to small-scale continuous culture is proposed. Second, bacterial aggregation in vortex flow is studied. We show that vortex flow can be easily produced in simple geometry. Microfluidic experiments reveal that a vortex can work as a habitat for microbes. Third, bacterial growth in slow directional flow is investigated. We propose a microfluidic design to systematically control the flow rate in culture chambers of various sizes.

I thank Andre Lai and Aaron Streets for helping me with designing and fabricating double-layer microfluidics. Jonathan White and Aaron Streets kindly let me use their KATARA system for controlling peristaltic mixing. I am also grateful to Siddhansh Agarwal for the helpful discussion about the hydrodynamics of lid-driven cavity flow. The Comsol simulations in this chapter are conducted in the Molecular Graphics and Computation Facility in University of California, Berkeley, and the facility is supported by NIH S10OD023532.

5.1   Mixing by external peristaltic forces

Mixing is critical for spatially-structured populations to diminish spatial heterogeneity. It makes nutrient availability or death rate uniform across populations and promotes the evolution of the populations. Mixing can be passively done by diffusion or motility of microbes. In addition, it is also possible to actively mix populations by external forces, such as shaking or peristaltic pushing.

Peristaltic motions are fundamental in the gut microbiome [106, 189]. They are useful to mix low Reynold number liquid, such as a viscous suspension or a small-volume culture, where shaking does not work well. Experimentally, peristaltic mixing has been applied to microfluidic experiments [190, 191], on behalf of a "shaken test tube". The mechanics are proposed by Quake

group using double-layer microfluidics [192, 193]. The device consists of a bottom thin "culture layer" and a top "control layer." By applying pressure to the control layer, the top layer pushes down the bottom one, and the deformation can completely close the bottom channel, known as Quake valve [192]. By actuating three valves in a certain order, directional flow can be produced, and it can be used for mixing.

We design a microfluidic device, whose design is inspired by the prior work [191]. Microbes can be cultured in a ring-shaped chamber, and peristaltic motions enable the mixing of the population. Importantly, the device allows us to continuously culture the population by serial dilution (fig. 5.1). The actuation of the valves is regulated by a KATARA system (Kit for Arduino-based Transistor Array Actuation) [194].
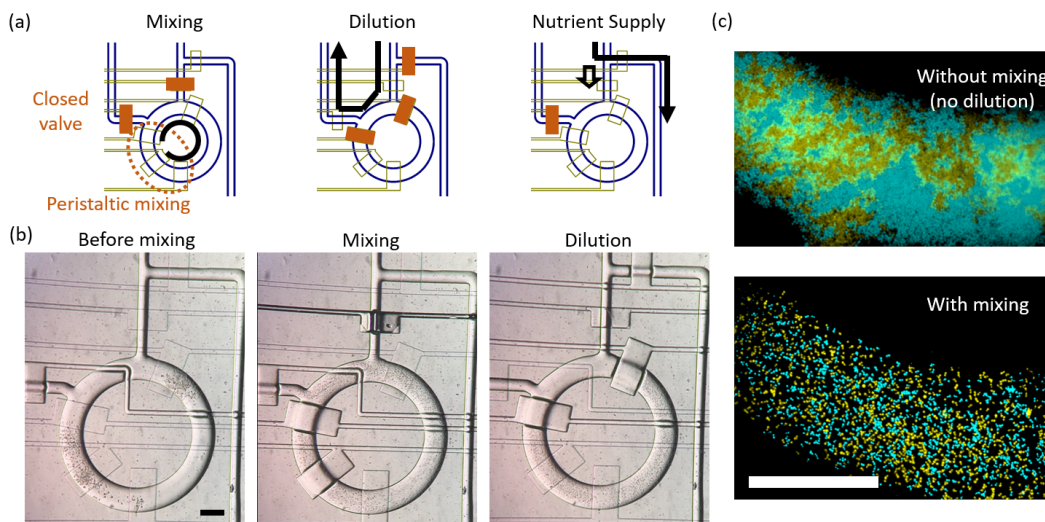
Figure 5.1: Microfluidics for mixing and continuously culturing microbial populations. (a) A schematic diagram of valve actuation for each step. Closed valves are shown in orange color. Black arrows show the movement of flow. In the "nutrient supply" step, a fresh culture medium is continuously flowed in the channel, and nutrients are supplied to the culture chamber by diffusion. (b) Experimental snapshots of mixing and dilution. *Saccharomyces cerevisiae* is cultured in the device. (c) Demonstration of mixing. Differently colored *Saccharomyces cerevisiae* strains, yJHK111 and yJHK112 [184], are cultured overnight without mixing (top) and mixed after the overnight culture (bottom). Scale bars show 300 μm.

Our system is not only useful for investigating the impact of spatial structures by tuning the degree of mixing, but also promising to continuously culture a small population, whose size is $\sim 10^4$ cells. Historically, liquid microbial cultures have been conducted with flasks, test tubes, or 96-well plates, whose volume is lower-bound by ~ 100 μL. This corresponds to $\sim 10^8$ population size, resulting in a characteristic evolutionary dynamics called *clonal interference* [195, 196]. Decreasing the population size is fundamental to studying the *periodic selection* regime instead of the

clonal interference regime (fig. 5.2) [197]. Our system provides a useful avenue to investigate the evolutionary dynamics of a small population [1] .
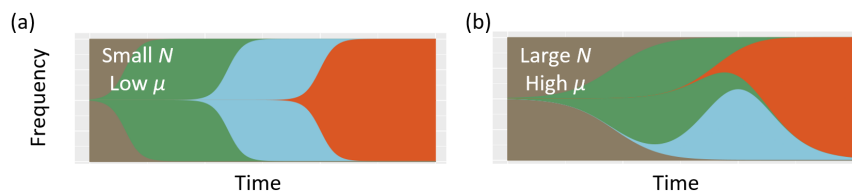
Figure 5.2: Illustrations of periodic selection and clonal interference. (a) With a small population size (N) and low mutation rate (μ), no beneficial mutation arises before one beneficial mutation is fixed. (b) With a large population size and high mutation rate, multiple beneficial mutations compete with each other.

5.2   Microbial aggregation in vortex flow

The migration of microbes is facilitated by fluid flow. Advective flow transports cells and produces characteristic spatial patterns. The impact of complex flow fields on population dynamics has not been well-studied, but recently its significance in the context of evolution has been highlighted by microbial experiments [198]. To study the impact of advective flow patterns, it is critical to experimentally produce flow fields in a controllable and reproducible manner. The study by Atis *et al.* [198] uses convective flow in a viscous liquid, but also, recent studies have shown that vortex patterns are easily produced and regulated with microfluidics [199–201].

There are mainly two different ways to produce vortex flow. One method uses high-speed flow so that a microfluidic system reaches the turbulent flow regime (high Reynolds number regime). High-speed vortices work as a "centrifuge" and selectively trap cells based on their size [200, 201]. On the other hand, the other way using the so-called *lid-driven cavity flow* works in the laminar flow regime (low Reynolds number regime) and does not require high-speed flow. Lid-driven cavity flow is originally found in 2D Stokes flow [202] but is also confirmed in 3D cases when the thickness of the cavity is large enough compared with the width [203, 204]. Experimentally, the swimming dynamics of marine microbes in a vortex have been studied using the second method [199], but the impact of a vortex on long-term dynamics, such as ecological and evolutionary dynamics, is still an open question.

In this section, we propose an experimental platform to trap and culture bacteria in vortices of various sizes. First, we simulate Stokes hydrodynamics in various geometries in Comsol (fig. 5.3). The simulations capture the sensitivity of the vortex formation to the ratio between the thickness

---

[1]Droplet microfluidics can also achieve a continuous culture of a small population. But it has an upper bound of the population size around $\sim 10^3$ cells. To accelerate evolution, $10^4 - 10^5$ is an ideal population size given the mutation rate of *E. coli* as a typical parameter.
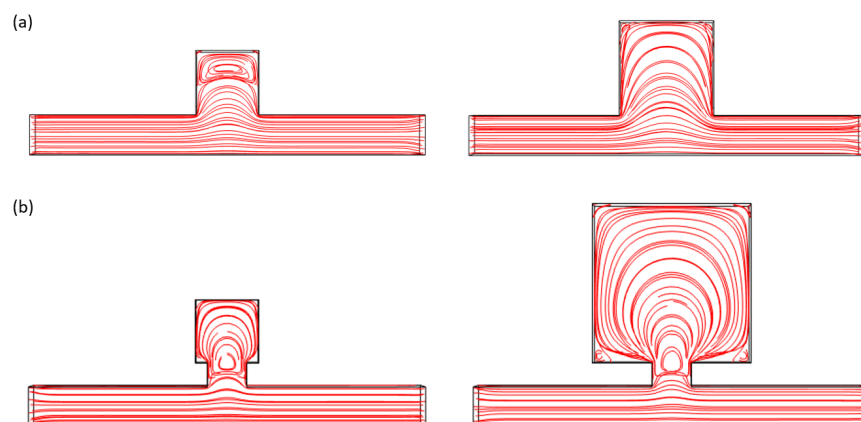
Figure 5.3: Streamlines in 3D Comsol simulations of lid-driven cavity flow. The thickness of the device is fixed as 80 μm. (a) The formation of vortices is sensitive to the size of a cavity. Vortices are formed in an 80 μm × 80 μm chamber (left) but not in a 120 μm × 120 μm chamber (right). (b) With an aperture, vortices are stably formed in an 80 μm × 80 μm chamber (left) and 200 μm × 200 μm chamber (right). The size of the aperture is fixed: the width is 50 μm, and the length is 30 μm.

and the width of the cavity (fig. 5.3a), as documented in the previous study [204]. This is problematic with the scalability of vortices: to increase the vortex size, the thickness of the device should also increase, which is experimentally challenging for microfluidics. To solve the issue, an aperture at the opening of a cavity [199] contributes to forming a "nuclear" of vortices and stabilizes large vortices (fig. 5.3b). Importantly, these cavities with a narrow opening can robustly form vortices independent of the flow rate. Our result suggests that vortex flow may be more ubiquitously observed in nature than previously expected.
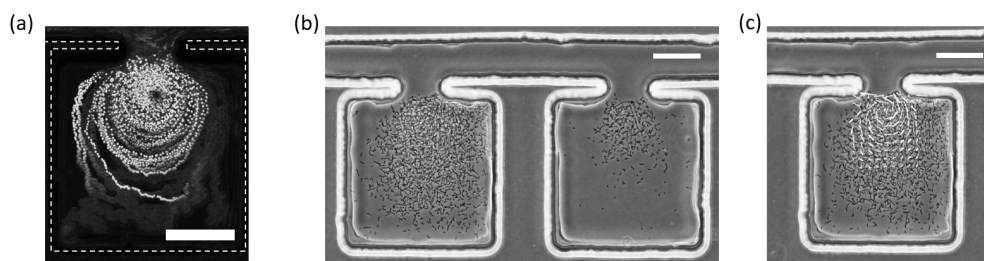
Figure 5.4: Microfluidic experiments show the aggregation of bacteria in vortices. (a) An overlay of trajectories of colloidal particles over 450 frames (15 minutes). (b) *Acetobacter indonesiensis* aggregates in vortices. (c) Movements of cells in vortices are analyzed by PIV and shown as white lines. The scale bars show 50 μm.

Next, we experimentally fabricate vortex-producing microfluidics and culture *Acetobacter indonesiensis* in vortices. Notably, cells aggregate around vortices and form populations (fig. 5.4). The populations are stable for at least two days, meaning that the trap is sufficiently stable for cells to proliferate. The experiments show that a trap by vortex flow can work as a habitat for microbes.

5.3 Population dynamics in slow directional flow

1D directional flow is a simple but important flow field that is biologically relevant, for example, to a human gut [189]. Population dynamics of microbes in the flow are largely affected by the flow rate. The most intriguing parameter regime is where the flow rate is low enough so that cells can have enough time to proliferate before they are washed out from the population. In an animal gut, the effective escape time of cells is extended by active diffusion, such as peristaltic mixing [106, 189]. However, it is also useful to highlight the pure impact of the slow flow rate.

Here, we propose a ladder-shaped microfluidic device with which a very slow flow rate is achieved in the spokes by subtle fluctuations of flow resistance. The device is an extension of our microfluidic panflute presented in chapter 2. The impact of 1D flow can be tested in pipe-like chambers (the "spokes" of the ladder) of various sizes (fig. 5.5).
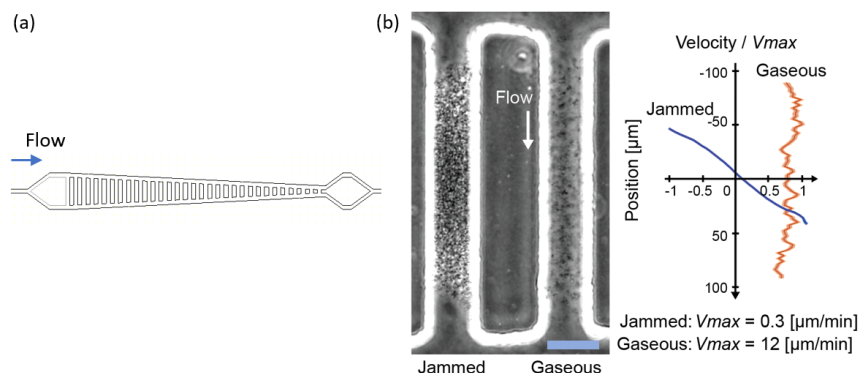
Figure 5.5: A microfluidic ladder device captures the growth of cells in slow flow. (a) The design of the ladder device. The incoming flow equally splits into both sides. There should be no flow in the spokes of the ladder in principle, but small fluctuations of the flow resistance can produce slow flow in the spokes by chance. (b) Colonization of *Acetobacter indonesiensis* in the spokes of a ladder device. The right panel shows the relative velocity across positions. In the jammed spoke, there is no significant flow because the jammed cells increase the flow resistance. On the other hand, the gaseous population directionally moves to the bottom. The scale bar shows 50 μm.

Ladder-shaped microfluidics has been used for tracking cell lineages with continuous nutrient supplies in previous studies [205, 206]. In these cases, The microbial populations in the "spokes" are dense-packed, and so there is no significant directional flow across the spokes because of

the high flow resistance due to dense-packing. In our device, we mainly focus on dilute gaseous populations in the spokes. The sensitivity of the flow direction in the spokes to flow resistance fluctuation has been previously reported and applied to microfluidic logic circuits with bubbles [207]. Using this feature, we successfully achieve slow directional flow in the spokes. We observe higher cellular density in the spokes than in the side channels, suggesting the proliferation of cells in the spokes. We also capture the length scale dependency of the population density, which is consistent with the result in chapter 2 (fig. 5.5).

The directional flow presented in fig. 5.5 is not very reproducible because it is a consequence of random fluctuations of flow resistance, such as fabrication errors or the presence of debris. To more systematically investigate the impact of directional flow, we propose another design of a ladder-shaped device inspired by a previous study [208]. The device aims to vary the length scale of spokes under the same flow rate (fig. 5.6a). The length of spokes can be calculated by the equations of flow pressure.

$$P_{tot} = [R_1 + r + 2r + \cdots + (n-1)r]I,$$

$$P_{tot} = [(n-1) + R_2 + 2r + 3r + \cdots + (n-1)r]I,$$

$$P_{tot} = [(n-1)r + (n-2)r + R_3 + 3r + \cdots + (n-1)r]I,$$

$$\vdots$$

$$P_{tot} = [(n-1)r + (n-2)r + \cdots + 2r + r + R_n]I,$$

where R_i and r are the hydrodynamic resistance, P_{tot} is the total pressure drop, and I is the flow current. In general,

$$P_{tot} = \left[R_k + r \sum_{i=1}^{k-1} (n-i) + r \sum_{i=k}^{n-1} i \right]. \tag{5.1}$$

It can be calculated as

$$P_{tot} = \left[R_k + r \left(n(k-1) - \frac{(k-1)k}{2} + \frac{(n+k-1)(n-k)}{2} \right) \right] I \tag{5.2}$$

$$= \left[R_k + r \left(-k^2 + (n+1)k + \frac{n(n-3)}{2} \right) \right] I. \tag{5.3}$$

Therefore,

$$R_k = \frac{P_{tot}}{I} + r \left(k^2 - (n+1)k - \frac{n(n-3)}{2} \right). \tag{5.4}$$

Note that the result is symmetrical: $R_j = R_{n-j+1}$. As the flow resistance is proportional to the length of the channel given the same cross-sectional area, the length of the spokes can be calculated. The spokes of the new ladder device should vary quadratically (fig. 5.6b). This device helps the investigation of the impact of directional flow on population dynamics, and how it is affected by spatial scale, as discussed in chapter 2.

(a)

(b)
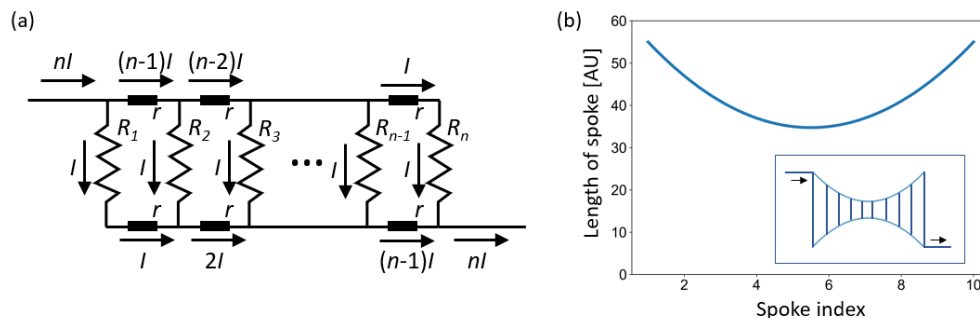
Figure 5.6: Designing a ladder device for investigating the impact of directional flow in pipes of various sizes. (a) The diagram of the flow pressure circuit. (b) The plot shows the length of the spokes of the ladder L_i. We assume $N = 10$, $P_{tot}/I = 100$, $r = 1$, and $L_i \sim R_i$. The inset shows a schematic illustration of a new ladder device.

5.4   Conclusion

In this chapter, microbial population dynamics in various types of hydrodynamic flow are studied, and the experimental technique to produce the flow fields is discussed. In nature, microbial populations are subject to various types of flow. Reproducing these environments in a controlled setup is critical to understand microbial ecology and evolution.

We successfully developed microfluidic experimental systems to study microbial population dynamics under (i) peristaltic mixing, (ii) vortex flow, and (iii) slow directional flow. The experiments in this chapter highlight the characteristic consequence of each flow pattern. (i) Peristaltic mixing breaks the spatial clusters of cells belonging to the same lineage. Disassembling clusters is expected to promote inter-species interactions. (ii) Microbes in vortex flow show aggregation. Given that lid-driven vortices can be easily and stably produced under certain geometries, the result suggests a possibility that hydrodynamic vortices work as microbial habitats. (iii) Bacterial populations in a slow directional flow exhibit two density phases, jammed and gaseous phases, depending on the length of pipes. The result is consistent with the finding in chapter 2. Importantly, jammed populations increase the flow resistance of the pipe and change the flow property. This experiment provides insight into the interplay between the environment and population density.

Bibliography

[1] P. Turchin, "Complex population dynamics", in *Complex population dynamics* (Princeton university press, 2013).

[2] M. Juhas, L. Eberl, and B. Tümmler, "Quorum sensing: the power of cooperation in the world of pseudomonas", Environmental microbiology **7**, 459–471 (2005).

[3] R. G. Abisado, S. Benomar, J. R. Klaus, A. A. Dandekar, and J. R. Chandler, "Bacterial quorum sensing and microbial community interactions", MBio **9**, e02331–17 (2018).

[4] Y.-H. Li and X. Tian, "Quorum sensing and bacterial social interactions in biofilms", Sensors **12**, 2519–2538 (2012).

[5] S. F. Gilbert, *Developmental biology.* (sinauer associates, Inc, 2010).

[6] E. Bianconi, A. Piovesan, F. Facchin, A. Beraudi, R. Casadei, F. Frabetti, L. Vitale, M. C. Pelleri, S. Tassani, F. Piva, S. Perez-Amodio, P. Strippoli, and S. Canaider, "An estimation of the number of cells in the human body", Annals of human biology **40**, 463–471 (2013).

[7] W. B. Cannon, "Organization for physiological homeostasis", Physiological reviews **9**, 399–431 (1929).

[8] M. Kimura, *The neutral theory of molecular evolution* (Cambridge University Press, 1983).

[9] E. Baake and W. Gabriel, "Biological evolution through mutation, selection, and drift: an introductory review", Annual Reviews of Computational Physics **7**, 203–264 (2000).

[10] D. Tilman, P. Kareiva, et al., *Spatial ecology: the role of space in population dynamics and interspecific interactions*, Vol. 30 (Princeton University Press, 1997).

[11] S. Altizer, R. Bartel, and B. A. Han, "Animal migration and infectious disease risk", science **331**, 296–302 (2011).

[12] D. E. Bowler and T. G. Benton, "Causes and consequences of animal dispersal strategies: relating individual behaviour to spatial dynamics", Biological reviews **80**, 205–225 (2005).

[13] D. McDougald, S. A. Rice, N. Barraud, P. D. Steinberg, and S. Kjelleberg, "Should we stay or should we go: mechanisms and ecological consequences for biofilm dispersal", Nature Reviews Microbiology **10**, 39–50 (2012).

[14] L. Solnica-Krezel and D. S. Sepich, "Gastrulation: making and shaping germ layers", Annual review of cell and developmental biology **28**, 687–717 (2012).

[15]M. A. McManus and C. B. Woodson, "Plankton distribution and ocean dispersal", Journal of Experimental Biology **215**, 1008–1016 (2012).

[16]G. C. Hays, A. J. Richardson, and C. Robinson, "Climate change and marine plankton", Trends in ecology & evolution **20**, 337–344 (2005).

[17]J. Adler, "Chemotaxis in bacteria", Annual review of biochemistry **44**, 341–356 (1975).

[18]H. C. Berg, "Chemotaxis in bacteria", Annual review of biophysics and bioengineering **4**, 119–136 (1975).

[19]G. E. Uhlenbeck and L. S. Ornstein, "On the theory of the brownian motion", Physical review **36**, 823 (1930).

[20]N. J. Gotelli et al., *A primer of ecology*, Vol. 494 (Sinauer Associates Sunderland, MA, 2008).

[21]K. M. Ibrahim, R. A. Nichols, and G. M. Hewitt, "Spatial patterns of genetic variation generated by different forms of dispersal during range expansion", Heredity **77**, 282–291 (1996).

[22]S. Klopfstein, M. Currat, and L. Excoffier, "The fate of mutations surfing on the wave of a range expansion", Molecular biology and evolution **23**, 482–490 (2006).

[23]H. Kierstead and L. B. Slobodkin, "The size of water masses containing plankton blooms", J. mar. Res **12**, 141–147 (1953).

[24]A. Okubo and S. A. Levin, *Diffusion and ecological problems: modern perspectives*, Vol. 14 (Springer, 2001).

[25]J. G. Skellam, "Random dispersal in theoretical populations", Biometrika **38**, 196–218 (1951).

[26]A. S. Griffin, S. A. West, and A. Buckling, "Cooperation and competition in pathogenic bacteria", Nature **430**, 1024–1027 (2004).

[27]H. H. Kong and J. A. Segre, "Skin microbiome: looking back to move forward", Journal of Investigative Dermatology **132**, 933–939 (2012).

[28]A. Conwill, A. C. Kuan, R. Damerla, A. J. Poret, J. S. Baker, A. D. Tripp, E. J. Alm, and T. D. Lieberman, "Anatomy promotes neutral coexistence of strains in the human skin microbiome", Cell Host & Microbe **30**, 171–182 (2022).

[29]E. A. Miller, D. E. Beasley, R. R. Dunn, and E. A. Archie, "Lactobacilli dominance and vaginal ph: why is the human vaginal microbiome unique?", Frontiers in microbiology **7**, 1936 (2016).

[30]C. Tropini, K. A. Earle, K. C. Huang, and J. L. Sonnenburg, "The gut microbiome: connecting spatial organization to function", Cell host & microbe **21**, 433–442 (2017).

[31]J. C. Stearns, M. D. Lynch, D. B. Senadheera, H. C. Tenenbaum, M. B. Goldberg, D. G. Cvitkovitch, K. Croitoru, G. Moreno-Hagelsieb, and J. D. Neufeld, "Bacterial biogeography of the human digestive tract", Scientific reports **1**, 1–9 (2011).

[32]G. P. Donaldson, S. M. Lee, and S. K. Mazmanian, "Gut biogeography of the bacterial microbiota", Nature Reviews Microbiology **14**, 20–32 (2016).

[33] D. M. Proctor and D. A. Relman, "The landscape ecology and microbiota of the human nose, mouth, and throat", Cell host & microbe **21**, 421–432 (2017).

[34] J. L. Mark Welch, B. J. Rossetti, C. W. Rieken, F. E. Dewhirst, and G. G. Borisy, "Biogeography of a human oral microbiome at the micron scale", Proceedings of the National Academy of Sciences **113**, E791–E800 (2016).

[35] J. L. Mark Welch, F. E. Dewhirst, and G. G. Borisy, "Biogeography of the oral microbiome: the site-specialist hypothesis", Annual review of microbiology **73**, 335–358 (2019).

[36] V. Torsvik and L. Øvreås, "Microbial diversity and function in soil: from genes to ecosystems", Current opinion in microbiology **5**, 240–245 (2002).

[37] L. Ranjard and A. Richaume, "Quantitative and qualitative microscale distribution of bacteria in soil", Research in microbiology **152**, 707–716 (2001).

[38] R. L. Berendsen, C. M. Pieterse, and P. A. Bakker, "The rhizosphere microbiome and plant health", Trends in plant science **17**, 478–486 (2012).

[39] W. A. Corpe, "Attachment of marine bacteria to solid surfaces", Adhesion in biological systems, 73–87 (1970).

[40] A. Giometto, D. R. Nelson, and A. W. Murray, "Physical interactions reduce the power of natural selection in growing yeast colonies", Proceedings of the National Academy of Sciences **115**, 11448–11453 (2018).

[41] J. Kayser, C. F. Schreck, M. Gralka, D. Fusco, and O. Hallatschek, "Collective motion conceals fitness differences in crowded cellular populations", Nature ecology & evolution **3**, 125–134 (2019).

[42] M. J. Müller, B. I. Neugeboren, D. R. Nelson, and A. W. Murray, "Genetic drift opposes mutualism during spatial population expansion", Proceedings of the National Academy of Sciences **111**, 1037–1042 (2014).

[43] J. L. Connell, A. K. Wessel, M. R. Parsek, A. D. Ellington, M. Whiteley, and J. B. Shear, "Probing prokaryotic social behaviors with bacterial "lobster traps"", MBio **1**, e00202–10 (2010).

[44] S. M. Lee, G. P. Donaldson, Z. Mikulski, S. Boyajian, K. Ley, and S. K. Mazmanian, "Bacterial colonization factors control specificity and stability of the gut microbiota", Nature **501**, 426–429 (2013).

[45] I. Martínez, M. X. Maldonado-Gomez, J. C. Gomes-Neto, H. Kittana, H. Ding, R. Schmaltz, P. Joglekar, R. J. Cardona, N. L. Marsteller, S. W. Kembel, et al., "Experimental evaluation of the importance of colonization history in early-life gut microbiota assembly", Elife **7** (2018).

[46] R. Dodge, E. W. Jones, H. Zhu, B. Obadia, D. J. Martinez, C. Wang, A. Aranda-Díaz, K. Aumiller, Z. Liu, M. Voltolini, et al., "A gut commensal niche regulates stable association of a multispecies microbiota", bioRxiv (2021).

[47] R. S. Cantrell and C. Cosner, *Spatial ecology via reaction-diffusion equations* (John Wiley & Sons, 2004).

[48]R. A. Fisher, "The wave of advance of advantageous genes", Annals of eugenics **7**, 355–369 (1937).

[49]J. D. Murray, "Mathematical biology: i. an introduction. interdisciplinary applied mathematics", Mathematical Biology, Springer **17** (2002).

[50]A. N. Kolmogorov, "A study of the equation of diffusion with increase in the quantity of matter, and its application to a biological problem", Moscow University Bulletin of Mathematics **1**, 1–25 (1937).

[51]W. C. Allee, O. Park, A. E. Emerson, T. Park, K. P. Schmidt, et al., *Principles of animal ecology.* Edn 1 (WB Saundere Co. Ltd., 1949).

[52]J. Monod, "The growth of bacterial cultures", Annual review of microbiology **3**, 371–394 (1949).

[53]T. M. Liggett and T. M. Liggett, *Interacting particle systems*, Vol. 2 (Springer, 1985).

[54]T. Shimaya and K. A. Takeuchi, "Lane formation and critical coarsening in a model of bacterial competition", Physical Review E **99**, 042403 (2019).

[55]F. Michor, Y. Iwasa, H. Rajagopalan, C. Lengauer, and M. A. Nowak, "Linear model of colon cancer initiation", Cell cycle **3**, 356–360 (2004).

[56]A. M. Klein, T. Nakagawa, R. Ichikawa, S. Yoshida, and B. D. Simons, "Mouse germ line stem cells undergo rapid and stochastic turnover", Cell stem cell **7**, 214–224 (2010).

[57]C. Lopez-Garcia, A. M. Klein, B. D. Simons, and D. J. Winton, "Intestinal stem cell replacement follows a pattern of neutral drift", Science **330**, 822–825 (2010).

[58]E. Murray, "A two-dimensional growth process", in Proc. 4th berkeley symp. math. statist. probability, Vol. 4 (Univ. California Press, Berkeley, 1960), p. 223.

[59]E. Domany and W. Kinzel, "Equivalence of cellular automata to ising models and directed percolation", Physical review letters **53**, 311 (1984).

[60]M. O. Lavrentovich, K. S. Korolev, and D. R. Nelson, "Radial domany-kinzel models with mutation and selection", Physical Review E **87**, 012103 (2013).

[61]H. Darcy, *Les fontaines publiques de la ville de dijon: exposition et application des principes à suivre et des formules à employer dans les questions de distribution d'eau: ouvrage terminé par un appendice relatif aux fournitures d'eau de plusieurs villes, au filtrage des eaux et à la fabrication des tuyaux de fonte, de plomb, de tôle et de bitume*, Vol. 2 (V. Dalmont, 1856).

[62]H. Byrne and D. Drasdo, "Individual-based and continuum models of growing cell populations: a comparison", Journal of mathematical biology **58**, 657–687 (2009).

[63]H. Byrne and M. A. Chaplain, "Free boundary value problems associated with the growth and development of multicellular spheroids", European Journal of Applied Mathematics **8**, 639–658 (1997).

[64]M. E. Kempner and R. A. Felder, "A review of cell culture automation", JALA: Journal of the Association for Laboratory Automation **7**, 56–62 (2002).

[65]L. Boitard, D. Cottinet, N. Bremond, J. Baudry, and J. Bibette, "Growing microbes in millifluidic droplets", Engineering in Life Sciences **15**, 318–326 (2015).

[66]T. S. Kaminski, O. Scheler, and P. Garstecki, "Droplet microfluidics for microbiology: techniques, applications and challenges", Lab on a Chip **16**, 2168–2187 (2016).

[67]P. B. Rainey and M. Travisano, "Adaptive radiation in a heterogeneous environment", Nature **394**, 69–72 (1998).

[68]S. R. Poltak and V. S. Cooper, "Ecological succession in long-term experimentally evolved biofilms produces synergistic communities", The ISME journal **5**, 369–378 (2011).

[69]P. Wang, L. Robert, J. Pelletier, W. L. Dang, F. Taddei, A. Wright, and S. Jun, "Robust growth of escherichia coli", Current biology **20**, 1099–1103 (2010).

[70]B. S. Griffiths and L. Philippot, "Insights into the resistance and resilience of the soil microbial community", FEMS microbiology reviews **37**, 112–129 (2013).

[71]C. A. Lozupone, J. I. Stombaugh, J. I. Gordon, J. K. Jansson, and R. Knight, "Diversity, stability and resilience of the human gut microbiota", Nature **489**, 220–230 (2012).

[72]K. Z. Coyte, J. Schluter, and K. R. Foster, "The ecology of the microbiome: networks, competition, and stability", Science **350**, 663–666 (2015).

[73]J. Oh, A. L. Byrd, M. Park, H. H. Kong, J. A. Segre, N. C. S. Program, et al., "Temporal stability of the human skin microbiome", Cell **165**, 854–866 (2016).

[74]T. Pédron, C. Mulet, C. Dauga, L. Frangeul, C. Chervaux, G. Grompone, and P. J. Sansonetti, "A crypt-specific core microbiota resides in the mouse colon", MBio **3**, e00116–12 (2012).

[75]A. Saffarian, C. Mulet, B. Regnault, A. Amiot, J. Tran-Van-Nhieu, J. Ravel, I. Sobhani, P. J. Sansonetti, and T. Pédron, "Crypt-and mucosa-associated core microbiotas in humans and their alteration in colon cancer patients", MBio **10** (2019).

[76]B. Obadia, Z. T. Güvener, V. Zhang, J. A. Ceja-Navarro, E. L. Brodie, W. J. William, and W. B. Ludington, "Probabilistic invasion underlies natural gut microbiome stability", Current Biology **27**, 1999–2006 (2017).

[77]T. D. Lawley and A. W. Walker, "Intestinal colonization resistance", Immunology **138**, 1–11 (2013).

[78]G. L. Grundmann, "Spatial scales of soil bacterial diversity–the size of a clone", FEMS microbiology ecology **48**, 119–127 (2004).

[79]A. M. Mowat and W. W. Agace, "Regional specialization within the intestinal immune system", Nature Reviews Immunology **14**, 667–685 (2014).

[80]D. Or, B. F. Smets, J. Wraith, A. Dechesne, and S. Friedman, "Physical constraints affecting bacterial habitats and activity in unsaturated porous media–a review", Advances in Water Resources **30**, 1505–1527 (2007).

[81] K. Z. Coyte, H. Tabuteau, E. A. Gaffney, K. R. Foster, and W. M. Durham, "Microbial competition in porous environments can select against rapid biofilm growth", Proceedings of the National Academy of Sciences **114**, E161–E170 (2017).

[82] C. Yang and K. M. Ottemann, "Control of bacterial colonization in the glands and crypts", Current opinion in microbiology **47**, 38–44 (2019).

[83] G. Lambert and E. Kussell, "Memory and fitness optimization of bacteria under fluctuating environments", PLoS Genet **10**, e1004556 (2014).

[84] R. Yamada, S. A. Deshpande, K. D. Bruce, E. M. Mak, and W. J. William, "Microbes promote amino acid harvest to rescue undernutrition in drosophila", Cell reports **10**, 865–872 (2015).

[85] E. K. Chu, O. Kilic, H. Cho, A. Groisman, and A. Levchenko, "Self-induced mechanical stress can trigger biofilm formation in uropathogenic escherichia coli", Nature communications **9**, 1–10 (2018).

[86] M. E. Cates and J. Tailleur, "Motility-induced phase separation", Annu. Rev. Condens. Matter Phys. **6**, 219–244 (2015).

[87] C. Wissel, "A universal law of the characteristic return time near thresholds", Oecologia **65**, 101–107 (1984).

[88] E. H. Van Nes and M. Scheffer, "Slow recovery from perturbations as a generic indicator of a nearby catastrophic shift", The American Naturalist **169**, 738–747 (2007).

[89] L. Dai, D. Vorselen, K. S. Korolev, and J. Gore, "Generic indicators for loss of resilience before a tipping point leading to population collapse", Science **336**, 1175–1177 (2012).

[90] S. Ramaswamy, "The mechanics and statistics of active matter", Annu. Rev. Condens. Matter Phys. **1**, 323–345 (2010).

[91] M. C. Marchetti, J.-F. Joanny, S. Ramaswamy, T. B. Liverpool, J. Prost, M. Rao, and R. A. Simha, "Hydrodynamics of soft active matter", Reviews of Modern Physics **85**, 1143 (2013).

[92] M. E. Cates, D. Marenduzzo, I. Pagonabarraga, and J. Tailleur, "Arrested phase separation in reproducing bacteria creates a generic route to pattern formation", Proceedings of the National Academy of Sciences **107**, 11715–11720 (2010).

[93] W. B. Russel, W. Russel, D. A. Saville, and W. R. Schowalter, *Colloidal dispersions* (Cambridge university press, 1991).

[94] J. Ladau and E. A. Eloe-Fadrosh, "Spatial, temporal, and phylogenetic scales of microbial ecology", Trends in microbiology **27**, 662–669 (2019).

[95] J. A. Wiens, "Spatial scaling in ecology", Functional ecology **3**, 385–397 (1989).

[96] S. A. Levin, "The problem of pattern and scale in ecology: the robert h. macarthur award lecture", Ecology **73**, 1943–1967 (1992).

[97] S. R.-J. Ross, Y. Suzuki, M. Kondoh, K. Suzuki, P. Villa Martín, and M. Dornelas, "Illuminating the intrinsic and extrinsic drivers of ecological stability across scales", Ecological Research **36**, 364–378 (2021).

[98]V. Dakos, B. Matthews, A. P. Hendry, J. Levine, N. Loeuille, J. Norberg, P. Nosil, M. Scheffer, and L. De Meester, "Ecosystem tipping points in an evolving world", Nature ecology & evolution **3**, 355–362 (2019).

[99]C. J. Marx and M. E. Lidstrom, "Development of improved versatile broad-host-range vectors for use in methylotrophs and other gram-negative bacteria", Microbiology **147**, 2065–2075 (2001).

[100]Y. Xia and G. M. Whitesides, "Soft lithography", Angewandte Chemie International Edition **37**, 550–575 (1998).

[101]J. C. McDonald, D. C. Duffy, J. R. Anderson, D. T. Chiu, H. Wu, O. J. Schueller, and G. M. Whitesides, "Fabrication of microfluidic systems in poly (dimethylsiloxane)", ELECTROPHORESIS: An International Journal **21**, 27–40 (2000).

[102]W. Thielicke and E. J. Stamhuis, "Pivlab-time-resolved digital particle image velocimetry tool for matlab", Published under the BSD license, programmed with MATLAB **7**, R14 (2014).

[103]J.-Y. Tinevez, N. Perry, J. Schindelin, G. M. Hoopes, G. D. Reynolds, E. Laplantine, S. Y. Bednarek, S. L. Shorte, and K. W. Eliceiri, "Trackmate: an open and extensible platform for single-particle tracking", Methods **115**, 80–90 (2017).

[104]C. Matano, "On the relation between the diffusion-coefficients and concentrations of solid metals", Japanese Journal of Physics **8**, 109–113 (1933).

[105]A. Savitzky and M. J. Golay, "Smoothing and differentiation of data by simplified least squares procedures.", Analytical chemistry **36**, 1627–1639 (1964).

[106]J. Cremer, I. Segota, C.-y. Yang, M. Arnoldini, J. T. Sauls, Z. Zhang, E. Gutierrez, A. Groisman, and T. Hwa, "Effect of flow and peristaltic mixing on bacterial growth in a gut-like channel", Proceedings of the National Academy of Sciences **113**, 11414–11419 (2016).

[107]G. Batchelor, "Brownian diffusion of particles with hydrodynamic interaction", Journal of Fluid Mechanics **74**, 1–29 (1976).

[108]C. S. Holling, "Resilience and stability of ecological systems", Annual review of ecology and systematics **4**, 1–23 (1973).

[109]A. J. Ladd, "Hydrodynamic transport coefficients of random dispersions of hard spheres", The Journal of chemical physics **93**, 3484–3494 (1990).

[110]J. t. Richarson, "Sedimentation and fluidisation: part i", Transactions of the institution of chemical engineers **32**, 35–53 (1954).

[111]N. F. Carnahan and K. E. Starling, "Equation of state for nonattracting rigid spheres", The Journal of chemical physics **51**, 635–636 (1969).

[112]J. D. Weeks, D. Chandler, and H. C. Andersen, "Role of repulsive forces in determining the equilibrium structure of simple liquids", The Journal of chemical physics **54**, 5237–5247 (1971).

[113]R. Zwanzig, *Nonequilibrium statistical mechanics* (Oxford University Press, 2001).

[114] A. P. Willard and D. Chandler, "Instantaneous liquid interfaces", The Journal of Physical Chemistry B **114**, 1954–1958 (2010).

[115] A. Mulero, F. Cuadros, and C. Galán, "Test of equations of state for the weeks–chandler–andersen reference system of two-dimensional lennard-jones fluids", The Journal of chemical physics **107**, 6887–6893 (1997).

[116] A. L. Thorneywork, R. E. Rozas, R. P. Dullens, and J. Horbach, "Effect of hydrodynamic interactions on self-diffusion of quasi-two-dimensional colloidal hard spheres", Physical review letters **115**, 268301 (2015).

[117] S. S. Khali, D. Chakraborty, and D. Chaudhuri, "Two-step melting of the weeks–chandler–anderson system in two dimensions", Soft Matter **17**, 3473–3485 (2021).

[118] O. Hallatschek and D. R. Nelson, "Gene surfing in expanding populations", Theoretical population biology **73**, 158–170 (2008).

[119] M.-C. Duvernoy, "Growth mechanics of a bacterial microcolony", PhD thesis (Université Grenoble Alpes, 2015).

[120] C. Aguilar, H. Vlamakis, A. Guzman, R. Losick, and R. Kolter, "Kind is a checkpoint protein linking spore formation to extracellular-matrix production in bacillus subtilis biofilms", MBio **1** (2010).

[121] J. Yan, C. D. Nadell, H. A. Stone, N. S. Wingreen, and B. L. Bassler, "Extracellular-matrix-mediated osmotic pressure drives vibrio cholerae biofilm expansion and cheater exclusion", Nature communications **8**, 1–11 (2017).

[122] O. P. Kuipers, P. G. de Ruyter, M. Kleerebezem, and W. M. de Vos, "Quorum sensing-controlled gene expression in lactic acid bacteria", Journal of Biotechnology **64**, 15–21 (1998).

[123] D. Fusco, M. Gralka, J. Kayser, A. Anderson, and O. Hallatschek, "Excess of mutational jackpot events in expanding populations revealed by spatial Luria-Delbrück experiments", Nature Communications **7**, 12760 (2016).

[124] C. D. Nadell, K. Drescher, and K. R. Foster, "Spatial structure, cooperation and competition in biofilms", Nature Reviews Microbiology **14**, 589 (2016).

[125] C. J. Chan, C.-P. Heisenberg, and T. Hiiragi, "Coordination of morphogenesis and cell-fate specification in development", Current Biology **27**, R1024–R1035 (2017).

[126] B. Waclaw, I. Bozic, M. E. Pittman, R. H. Hruban, B. Vogelstein, and M. A. Nowak, "A spatial model predicts that dispersal and cell turnover limit intratumour heterogeneity", Nature **525**, 261 (2015).

[127] C. Carmona-Fontaine, M. Deforet, L. Akkari, C. B. Thompson, J. A. Joyce, and J. B. Xavier, "Metabolic origins of spatial organization in the tumor microenvironment", Proceedings of the National Academy of Sciences **114**, 2934–2939 (2017).

[128]K. J. Lenos, D. M. Miedema, S. C. Lodestijn, L. E. Nijman, T. van den Bosch, X. R. Ros, F. C. Lourenço, M. C. Lecca, M. van der Heijden, S. M. van Neerven, et al., "Stem cell functionality is microenvironmentally defined during tumour expansion and therapy response in colon cancer", Nature cell biology **20**, 1193 (2018).

[129]M. van der Heijden, D. M. Miedema, B. Waclaw, V. L. Veenstra, M. C. Lecca, L. E. Nijman, E. van Dijk, S. M. van Neerven, S. C. Lodestijn, K. J. Lenos, et al., "Spatiotemporal regulation of clonogenicity in colorectal cancer xenografts", Proceedings of the National Academy of Sciences **116**, 6140–6145 (2019).

[130]L. Vermeulen, E. Morrissey, M. Van Der Heijden, A. M. Nicholson, A. Sottoriva, S. Buczacki, R. Kemp, S. Tavaré, and D. J. Winton, "Defining stem cell dynamics in models of intestinal tumor initiation", Science **342**, 995–998 (2013).

[131]A. M. Klein and B. D. Simons, "Universal patterns of stem cell fate in cycling adult tissues", Development **138**, 3103–3111 (2011).

[132]S. Rulands and B. D. Simons, "Tracing cellular dynamics in tissue development, maintenance and disease", Current Opinion in Cell Biology **43**, 38–45 (2016).

[133]S. Chabab, F. Lescroart, S. Rulands, N. Mathiah, B. D. Simons, and C. Blanpain, "Uncovering the Number and Clonal Dynamics of Mesp1 Progenitors during Heart Morphogenesis", Cell Reports **14**, 1–10 (2016).

[134]C. Carmona-Fontaine, V. Bucci, L. Akkari, M. Deforet, J. A. Joyce, and J. B. Xavier, "Emergence of spatial structure in the tumor microenvironment due to the Warburg effect", Proceedings of the National Academy of Sciences **110**, 19402–19407 (2013).

[135]S. Lamprecht, E. M. Schmidt, C. Blaj, H. Hermeking, A. Jung, T. Kirchner, and D. Horst, "Multicolor lineage tracing reveals clonal architecture and dynamics in colon cancer", Nature Communications **8**, 1–8 (2017).

[136]V. D. Varner, J. P. Gleghorn, E. Miller, D. C. Radisky, and C. M. Nelson, "Mechanically patterning the embryonic airway epithelium", Proceedings of the National Academy of Sciences **112**, 9230–9235 (2015).

[137]M. D. Ryser, B.-H. Min, K. D. Siegmund, and D. Shibata, "Spatial mutation patterns as markers of early colorectal tumor cell mobility", Proceedings of the National Academy of Sciences **115**, 5774–5779 (2018).

[138]M. Baym, T. D. Lieberman, E. D. Kelsic, R. Chait, R. Gross, I. Yelin, and R. Kishony, "Spatiotemporal microbial evolution on antibiotic landscapes", Science **353**, 1147–1151 (2016).

[139]M. A. Nowak, F. Michor, and Y. Iwasa, "The linear process of somatic evolution", Proceedings of the National Academy of Sciences **100**, 14966–14969 (2003).

[140]M. O. Lavrentovich, M. E. Wahl, D. R. Nelson, and A. W. Murray, "Spatially Constrained Growth Enhances Conversional Meltdown", Biophysical Journal **110**, 2800–2808 (2016).

[141] O. Hallatschek, P. Hersen, S. Ramanathan, and D. R. Nelson, "Genetic drift at expanding frontiers promotes gene segregation", Proceedings of the National Academy of Sciences **104**, 19926–19930 (2007).

[142] Z. Ahmed and S. Gravel, "Intratumor heterogeneity and circulating tumor cell clusters", Molecular biology and evolution **35**, 2135–2144 (2017).

[143] H. Tanaka, Z. Zeravcic, and M. P. Brenner, "Mutation at Expanding Front of Self-Replicating Colloidal Clusters", Physical Review Letters **117**, 1–5 (2016).

[144] S. Peischl, I. Dupanloup, M. Kirkpatrick, and L. Excoffier, "On the accumulation of deleterious mutations during range expansions", Molecular Ecology **22**, 5972–5982 (2013).

[145] S. Peischl, I. Dupanloup, L. Bosshard, and L. Excoffier, "Genetic surfing in human populations: from genes to genomes", Current Opinion in Genetics and Development **41**, 53–61 (2016).

[146] R. Zöllner, E. R. Oldewurtel, N. Kouzel, and B. Maier, "Phase and antigenic variation govern competition dynamics through positioning in bacterial colonies", Scientific Reports **7**, 1–12 (2017).

[147] C. C. Traverse, L. M. Mayo-Smith, S. R. Poltak, and V. S. Cooper, "Tangled bank of experimentally evolved Burkholderia biofilms reflects selection during chronic infections", Proceedings of the National Academy of Sciences **110**, E250–E259 (2013).

[148] F. D. Farrell, M. Gralka, O. Hallatschek, and B. Waclaw, "Mechanical interactions in bacterial colonies and the surfing probability of beneficial mutations", Journal of The Royal Society Interface **14**, 20170073 (2017).

[149] M. O. Lavrentovich, J. H. Koschwanez, and D. R. Nelson, "Nutrient shielding in clusters of cells", Physical Review E **87**, 062703 (2013).

[150] J.-R. Meunier and M. Choder, "Saccharomyces cerevisiae colony growth and ageing: biphasic growth accompanied by changes in gene expression", Yeast **15**, 1159–1169 (1999).

[151] L. Váchová and Z. Palková, "How structured yeast multicellular communities live, age and die?", FEMS yeast research **18**, foy033 (2018).

[152] S. Pirt, "A kinetic study of the mode of growth of surface colonies of bacteria and fungi", Microbiology **47**, 181–197 (1967).

[153] L. Excoffier and N. Ray, "Surfing during population expansions promotes genetic revolutions and structuration", Trends in ecology & evolution **23**, 347–351 (2008).

[154] U. D. Monte, "Does the cell number 109 still really fit one gram of tumor tissue?", Cell Cycle **8**, PMID: 19176997, 505–506 (2009).

[155] A. Sottoriva, H. Kang, Z. Ma, T. A. Graham, M. P. Salomon, J. Zhao, P. Marjoram, K. Siegmund, M. F. Press, D. Shibata, et al., "A big bang model of human colorectal tumor growth", Nature genetics **47**, 209 (2015).

[156] M. J. Williams, B. Werner, C. P. Barnes, T. A. Graham, and A. Sottoriva, "Identification of neutral tumor evolution across cancer types", Nature genetics **48**, 238 (2016).

[157]S. Luria and M. Delbrück, "Mutations of Bacteria from Virus Sensitivity to Virus Resistance.", Genetics **28**, 491–511 (1943).

[158]H. B. Newcombe, "Origin of bacterial variants", Nature **164**, 150 (1949).

[159]K. C. Atwood, L. K. Schneider, and F. J. Ryan, "Periodic selection in escherichia coli", Proceedings of the National Academy of Sciences **37**, 146–155 (1951).

[160]J. Lederberg and E. M. Lederberg, "Replica plating and indirect selection of bacterial mutants", Journal of Bacteriology **63**, 399 (1952).

[161]B. J. Thomas and R. Rothstein, "Elevated recombination rates in transcriptionally active dna", Cell **56**, 619–630 (1989).

[162]C. F. Pope, D. M. O'Sullivan, T. D. McHugh, and S. H. Gillespie, "A practical guide to measuring mutation rates in antibiotic resistance", Antimicrobial agents and chemotherapy **52**, 1209–1214 (2008).

[163]D. E. Lea and C. A. Coulson, "The distribution of the numbers of mutants in bacterial populations", Journal of Genetics **49**, 264–285 (1949).

[164]M. Gralka, F. Stiewe, F. Farrell, W. Möbius, B. Waclaw, and O. Hallatschek, "Allele surfing promotes microbial adaptation from standing variation", Ecology letters **19**, 889–898 (2016).

[165]W. Mather, O. Mondragón-Palomino, T. Danino, J. Hasty, and L. S. Tsimring, "Streaming instability in growing cell populations", Physical review letters **104**, 208101 (2010).

[166]D. Boyer, W. Mather, O. Mondragón-Palomino, S. Orozco-Fuentes, T. Danino, J. Hasty, and L. S. Tsimring, "Buckling instability in ordered bacterial colonies", Physical biology **8**, 026008 (2011).

[167]W.-H. Lin and E. Kussell, "Complex interplay of physiology and selection in the emergence of antibiotic resistance", Current Biology **26**, 1486–1493 (2016).

[168]M. Delarue, J. Hartung, C. Schreck, P. Gniewek, L. Hu, S. Herminghaus, and O. Hallatschek, "Self-driven jamming in growing microbial populations", Nature physics **12**, 762–766 (2016).

[169]M. Gerlinger, A. J. Rowan, S. Horswell, J. Larkin, D. Endesfelder, E. Gronroos, P. Martinez, N. Matthews, A. Stewart, P. Tarpey, et al., "Intratumor heterogeneity and branched evolution revealed by multiregion sequencing", New England journal of medicine **366**, 883–892 (2012).

[170]E. C. de Bruin, N. McGranahan, R. Mitter, M. Salm, D. C. Wedge, L. Yates, M. Jamal-Hanjani, S. Shafi, N. Murugaesu, A. J. Rowan, et al., "Spatial and temporal diversity in genomic instability processes defines lung cancer evolution", Science **346**, 251–256 (2014).

[171]J. Zhang, J. Fujimoto, J. Zhang, D. C. Wedge, X. Song, J. Zhang, S. Seth, C.-W. Chow, Y. Cao, C. Gumbs, et al., "Intratumor heterogeneity in localized lung adenocarcinomas delineated by multiregion sequencing", Science **346**, 256–259 (2014).

[172]S. Ling, Z. Hu, Z. Yang, F. Yang, Y. Li, P. Lin, K. Chen, L. Dong, L. Cao, Y. Tao, et al., "Extremely high genetic diversity in a single tumor points to prevalence of non-darwinian cell evolution", Proceedings of the National Academy of Sciences **112**, E6496–E6505 (2015).

[173]R. Sun, Z. Hu, A. Sottoriva, T. A. Graham, A. Harpak, Z. Ma, J. M. Fischer, D. Shibata, and C. Curtis, "Between-region genetic divergence reflects the mode and tempo of tumor evolution", Nature genetics **49**, 1015 (2017).

[174]J. A. Gallaher, P. M. Enriquez-Navas, K. A. Luddy, R. A. Gatenby, and A. R. Anderson, "Spatial heterogeneity and evolutionary dynamics modulate time to recurrence in continuous and adaptive cancer therapiescontinuous versus adaptive cancer therapies", Cancer research **78**, 2127–2139 (2018).

[175]M. Tarabichi, I. Martincorena, M. Gerstung, A. M. Leroi, F. Markowetz, S. C. Dentro, I. Leshchiner, M. Gerstung, C. Jolly, K. Haase, M. Tarabichi, J. Wintersinger, A. G. Deshwar, K. Yu, S. Gonzalez, Y. Rubanova, G. Macintyre, D. J. Adams, P. Anur, R. Beroukhim, P. C. Boutros, D. D. Bowtell, P. J. Campbell, S. Cao, E. L. Christie, M. Cmero, Y. Cun, K. J. Dawson, J. Demeulemeester, N. Donmez, R. M. Drews, R. Eils, Y. Fan, M. Fittall, D. W. Garsed, G. Getz, G. Ha, M. Imielinski, L. Jerman, Y. Ji, K. Kleinheinz, J. Lee, H. Lee-Six, D. G. Livitz, S. Malikic, F. Markowetz, I. Martincorena, T. J. Mitchell, V. Mustonen, L. Oesper, M. Peifer, M. Peto, B. J. Raphael, D. Rosebrock, S. C. Sahinalp, A. Salcedo, M. Schlesner, S. Schumacher, S. Sengupta, R. Shi, S. J. Shin, L. D. Stein, I. Vázquez-García, S. Vembu, D. A. Wheeler, T.-P. Yang, X. Yao, K. Yuan, H. Zhu, W. Wang, Q. D. Morris, P. T. Spellman, D. C. Wedge, P. Van Loo, P. T. Spellman, Q. D. Morris, O. C. Lingjærde, D. C. Wedge, P. Van Loo, T. P. E. Group, and H. Working, "Neutral tumor evolution?", Nature Genetics **50**, 1630–1633 (2018).

[176]T. Heide, L. Zapata, M. J. Williams, B. Werner, G. Caravagna, C. P. Barnes, T. A. Graham, and A. Sottoriva, "Reply to a 'Neutral tumor evolution?'", Nature Genetics **50**, 1633–1637 (2018).

[177]K. Chkhaidze, T. Heide, B. Werner, M. J. Williams, W. Huang, G. Caravagna, T. A. Graham, and A. Sottoriva, "Spatially constrained tumour growth affects the patterns of clonal selection and neutral drift in cancer genomic data", PLoS computational biology **15**, e1007243 (2019).

[178]L. Chao and E. C. Cox, "Competition between high and low mutating strains of escherichia coli", Evolution **37**, 125–134 (1983).

[179]A. E. Dodson and J. Rine, "Heritable capture of heterochromatin dynamics in saccharomyces cerevisiae", Elife **4**, e05007 (2015).

[180]D. L. Lindstrom and D. E. Gottschling, "The mother enrichment program: a genetic system for facile replicative life span analysis in saccharomyces cerevisiae", Genetics **183**, 413–422 (2009).

[181]N. Otsu, "A Threshold Selection Method from Gray-Level Histograms", IEEE Transactions on Systems, Man, and Cybernetics **9**, 62–66 (1979).

[182]W. Thielicke and E. J. Stamhuis, "Pivlab-towards user-friendly, affordable and accurate digital particle image velocimetry in matlab", Journal of Open Research Software **2**, e30 (2014).

[183]C. Logie and A. F. Stewart, "Ligand-regulated site-specific recombination", Proceedings of the National Academy of Sciences **92**, 5940–5944 (1995).

[184]K. S. Korolev, M. J. Müller, N. Karahan, A. W. Murray, O. Hallatschek, and D. R. Nelson, "Selective sweeps in growing microbial colonies", Physical biology **9**, 026008 (2012).

[185]P. Gniewek, C. F. Schreck, and O. Hallatschek, "Biomechanical feedback strengthens jammed cellular packings", Phys. Rev. Lett. **122**, 208102 (2019).

[186]B. Derrida and R. Dickman, "On the interface between two growing eden clusters", Journal of Physics A: Mathematical and General **24**, L191 (1991).

[187]S. Chu, M. Kardar, D. R. Nelson, and D. A. Beller, "Evolution in range expansions with competition at rough boundaries", Journal of theoretical biology **478**, 153–160 (2019).

[188]O. Hallatschek and D. R. Nelson, "Life at the front of an expanding population", Evolution: International Journal of Organic Evolution **64**, 193–206 (2010).

[189]O. M. Ghosh and B. H. Good, "Emergent evolutionary forces in spatial models of microbial growth in the human gut microbiota", bioRxiv, 2021–07 (2022).

[190]F. K. Balagaddé, L. You, C. L. Hansen, F. H. Arnold, and S. R. Quake, "Long-term monitoring of bacteria undergoing programmed population control in a microchemostat", Science **309**, 137–140 (2005).

[191]B. M. Paegel and G. F. Joyce, "Darwinian evolution on a chip", PLoS biology **6**, e85 (2008).

[192]M. A. Unger, H.-P. Chou, T. Thorsen, A. Scherer, and S. R. Quake, "Monolithic microfabricated valves and pumps by multilayer soft lithography", science **288**, 113–116 (2000).

[193]J. Melin and S. R. Quake, "Microfluidic large-scale integration: the evolution of design rules for biological automation", Annual review of biophysics and biomolecular structure **36**, 213–231 (2007).

[194]J. A. White and A. M. Streets, "Controller for microfluidic large-scale integration", HardwareX **3**, 135–145 (2018).

[195]I. Cvijović, A. N. N. Ba, and M. M. Desai, "Experimental studies of evolutionary dynamics in microbes", Trends in Genetics **34**, 693–703 (2018).

[196]G. I. Lang, D. P. Rice, M. J. Hickman, E. Sodergren, G. M. Weinstock, D. Botstein, and M. M. Desai, "Pervasive genetic hitchhiking and clonal interference in forty evolving yeast populations", Nature **500**, 571–574 (2013).

[197]J. A. G. de Visser and D. E. Rozen, "Clonal interference and the periodic selection of new beneficial mutations in escherichia coli", Genetics **172**, 2093–2100 (2006).

[198]S. Atis, B. T. Weinstein, A. W. Murray, and D. R. Nelson, "Microbial range expansions on liquid substrates", Physical review X **9**, 021058 (2019).

[199]R. Stocker, "Microorganisms in vortices: a microfluidic setup", Limnology and Oceanography: Methods **4**, 392–398 (2006).

[200]S. C. Hur, A. J. Mach, and D. Di Carlo, "High-throughput size-based rare cell enrichment using microscale vortices", Biomicrofluidics **5**, 022206 (2011).

[201]A. J. Mach, J. H. Kim, A. Arshi, S. C. Hur, and D. Di Carlo, "Automated cellular sample preparation using a centrifuge-on-a-chip", Lab on a Chip **11**, 2827–2834 (2011).

[202]J. J. Higdon, "Stokes flow in arbitrary two-dimensional domains: shear flow over ridges and cavities", Journal of Fluid Mechanics **159**, 195–226 (1985).

[203]P. Shankar and M. Deshpande, "Fluid mechanics in the driven cavity", Annual review of fluid mechanics **32**, 93–136 (2000).

[204]N. Osterman, J. Derganc, and D. Svenšek, "Formation of vortices in long microcavities at low reynolds number", Microfluidics and Nanofluidics **20**, 1–10 (2016).

[205]M. Hashimoto, T. Nozoe, H. Nakaoka, R. Okura, S. Akiyoshi, K. Kaneko, E. Kussell, and Y. Wakamoto, "Noise-driven growth rate gain in clonal cellular populations", Proceedings of the National Academy of Sciences **113**, 3251–3256 (2016).

[206]A. M. Proenca, C. U. Rang, C. Buetz, C. Shi, and L. Chao, "Age structure landscapes emerge from the equilibrium between aging and rejuvenation in bacterial populations", Nature communications **9**, 1–11 (2018).

[207]M. Prakash and N. Gershenfeld, "Microfluidic bubble logic", Science **315**, 832–835 (2007).

[208]D. Tondeur, Y. Fan, J.-M. Commenge, and L. Luo, "Uniform flows in rectangular lattice networks", Chemical engineering science **66**, 5301–5312 (2011).